Department of Physics and Astronomy
University Heidelberg

Diploma Thesis
in Physics

submitted by
Martin Hackel
born in Heidelberg

2013

Dielectric Profiling of Alpine Ice Cores as Assistance for Ground Penetrating Radar

This diploma thesis has been carried out
at the Institute of Environmental Physics
by Martin Hackel under the supervision of
Dr. D. Wagenbach, Dr. P. Bohleber

Referees:
Prof. Dr. K. Roth
Prof. Dr. O. Eisen

ABSTRACT

The present thesis aimed to, for the first, deploy dielectric profiling (DEP) to an entire Alpine ice core drilled to bedrock. DEP allows for a non-destructive measurement of an ice core's complex relative dielectric permittivity at kHz frequencies. Based on the thus obtained dielectric profile of the core, it was the task to derive a synthetic radargramm by forward modelling and to compare the later with radar traces from ground penetrating radar (GPR). Forward modelling by convolution of the reflectance profile, derived from DEP data, with a synthetic radar wavelet in the time domain yields a synthetic radargramm, which in principle should reproduce the coherent features of a GPR trace recorded adjacent to the borehole. Thereby a physical connection between ice core properties and radar reflectors is established. The method was applied in full extent to the CDM core from Col du Dôme (CDD), Mont Blanc, and partially to the KCC core from Colle Gnifetti (CG), Monte Rosa, which supplemented the thesis in it's final stage. The DEP data of the CDM core was afflicted with a comparatively large amount of defects and with artefacts due to a dysfunction of the DEP setup. An adequate approach of data treatment was rigorously developed and applied. The corrections could be assessed with the complementary data of the KCC core. Analysis of the DEP profiles e.g probably allowed the identification of a known regime change in Alpine snow chemistry in the 1950s. Forward modelling reproduced in the firn part several reflectors from GPR traces adjacent to the borehole predominately caused by permittivity changes. As by product the analysis of radargramms from CDD revealed below the firn-ice transition a reflector-free zone (RFZ), as it is known from CG, and offered some indications regarding its origin.

ZUSAMMENFASSUNG

Ziel dieser Arbeit war es, erstmalig einen vollständigen bis zum Felsbett gebohrten alpinen Eiskern mittels Dielectric Profiling (DEP) zu vermessen. DEP erlaubt die zerstörungsfreie Messung der komplexen relativen dielektrischen Permittivität eines Eiskerns im kHz-Frequenzbereich. Auf Basis der gemessenen dielektrischen Profile sollte durch Vorwärtsmodellierung eine synthetische Radarspur abgeleitet und mit Bodenradarmessungen (GPR) verglichen werden. Vorwärtsmodellierung mittels Faltung eines aus DEP-Daten gewonnenen Reflektivitätsprofils mit einem synthetischen Radarpuls im Zeitraum liefert eine synthetische Radarspur, welche prinzipiell die wesentlichen Eigenschaften einer Bodenradarmessung am Ort der Bohrung reproduzieren sollte. Eiskerneigenschaften und Radarreflektoren werden dadurch physikalisch verknüpft. Die Methode wurde vollumfänglich auf den CDM-Kern vom Col du Dôme (CDD), Mont Blanc, und in Teilen auf den in der Endphase hinzugekommenen KCC-Kern vom Colle Gnifetti (CG), Monte Rosa, angewandt. Die DEP-Daten des CDM-Kerns waren stark mit Artefakten behaftet, die teilweise von der vergleichsweise großen Defektrate des Kerns und teilweise von einer Fehlfunktion der Messapparatur herrührten. Umfassende Korrekturen wurden entwickelt und angewandt und konnten mit den Vergleichsdaten des KCC-Kerns evaluiert werden. Die Analyse der DEP-Daten erlaubte unter Anderem die wahrscheinliche Identifikation eines bekannten Regimewechsels in der Alpinen Eischemie während der 1950er Jahre. Die Vorwärtsmodellierung führte zu einigen übereinstimmenden Reflektoren im Firnbereich, die überwiegend durch Permittivitätsschwankungen verursacht werden. Als Nebenprodukt der Analyse der Bodenradarstudien, wurde am CDD unterhalb des Firneisüberganges eine reflektorfreie Zone (RFZ), wie sie bereits vom CG bekannt ist, sowie Hinweise auf deren Ursprung gefunden.

CONTENTS

... man who keep company with glaciers come
to feel tolerably insignificant by and by.

Mark Twain,
A Tramp Abroad, Chap. XL

1 INTRODUCTION

The research on the anthropogenic impact on climate requires records of natural climate variability in the preindustrial era. To this end natural climate archives like sea sediments[Cronin *et al.*, 2013], tree rings [Corona *et al.*, 2010, Hafner *et al.*, 2013] or glaciers [Petit *et al.*, 1999] have to be explored, as comprehensive instrumental records only date back to the 18th century [Auer *et al.*, 2007, Böhm *et al.*, 2010]. Amongst these possible sources cold glaciers are unique, as they do not only comprise a stratigraphical record of past temperature variability archived in stable water respectively oxygen isotopes [Dansgaard, 1964, Johnsen *et al.*, 2001], but also of the atmospheric composition [Lüthi *et al.*, 2008] entrapped in innumerous air bubbles in the ice matrix.

Obtaining stratigraphical climate records relies basically on the local drilling of ice cores. Corresponding research on polar ice sheets has successfully established a history of climate and atmosphere in polar regions reaching back as far as 800,000 years before present (BP) [Petit *et al.*, 1999, Lüthi *et al.*, 2008, Lambert *et al.*, 2008, Dahl-Jensen *et al.*, 2013]. However, complementary ice core records for regions of medium latitudes, that are closer to human settlements, can only be gained from a few sufficiently cold remote and high-elevated alpine[1] glaciers [Haeberli, 1976, e.g.], which are not subject to melting and which's stratigraphy is not disturbed by melt water percolation. They bear particular difficulties for ice core studies,caused by complex bedrock topographies, spatio-temporally variable accumulation patterns and complex ice flow [Wagenbach, 1992, Wagenbach *et al.*, 2012]. Their ice core records in general are not yet understood as well as their polar counterparts, they mainly cover the Holocene and are afflicted with hard to quantify dating uncertainties, rapidly growing with depth [e.g. Wagenbach, 1992].

Partial remedy may be gained by spatial radar surveys [Navarro and Eisen, 2009, Bogorodskiĭ *et al.*, 1985], which proved to be a powerful complement to polar ice core studies, and principally allow the spatial extrapolation of dated ice core properties [Millar, 1981, Hempel *et al.*, 2000, Eisen *et al.*, 2003a] along internal reflecting horizons (IRH), i.e. layers of homogeneous density and acidity that are interpreted as isochrones [Robin *et al.*, 1969], and thus the synchronization of various ice cores of one glacier [Jacobel and Hodge, 1995, Siegert *et al.*, 1998].

However, combined investigations by ice core studies and GPR surveys require a solid understanding of the dielectric properties of glacier ice. E.g. ice core properties are measured in the depth domain while radar traces are recorded in the time domain, which both are linked through the electromagnetic wave-velocity profile. The dielectric properties of an ice core can be obtained by dielectric profiling (DEP) [Moore and Paren, 1987, Wilhelms, 1996, 2000], i.e. the measurement of capacitance and conductance with a cylindrical capacitor. Such records in principle allow a conclusion on the main variable contributions to the glacier ice's dielectric properties, its impurity content [Moore *et al.*, 1990, 1992, 1994, Wolff, 1995, Wolff *et al.*, 1997a] and density [Moore, 1988, Wilhelms, 1996, 2000, 2005], and on the other hand the derivation of a theoretical reflectance profile and further by forward modelling of a synthetic radargramm [Moore, 1988, Blindow, 1994a, Hildebrand, 1996, Miners *et al.*, 1997, 2002, Eisen *et al.*, 2003b,c, 2004, 2006]. The comparison of synthetic and recorded GPR radargramms thus in principle allows a direct connection of ice core properties and recorded radar reflectors.

Even though combined investigations based on ice core studies, GPR surveys, DEP and forward modelling have been applied very successfully on polar sites, first promising approaches on alpine sites

[1] In this thesis *alpine* will refer to mountain glaciers in general, while the capital *Alpine* will denote such in the European Alps.

that combined GPR and ice core informations have been conducted just recently [Eisen *et al.*, 2003a, Bohleber, 2011, Konrad, 2011, Konrad *et al.*, 2013]. In this sequence Bohleber [2011], Konrad *et al.* [2013] lately were able to establish a method to assess inter-core dating coherency and uncertainty in a multi-core array on the cold Alpine[1] glacier Colle Gnifetti (CG) in the Monte Rosa region, Swiss Alps, on basis of ice core data, GPR surveys and a 2.5-dimensional flow model. However, the uncertainty of the datings transferred from ice cores on to IRH still was rapidly growing with depth and major limitations arose from the vanishing of the IRH below about half the glaciers depth, a phenomenon referred to as reflector-free zone (RFZ)[2] [Eisen *et al.*, 2003a, Konrad, 2011]. A comprehensive investigation of the connective dielectric profiles of alpine glaciers is ongoing, though a first attempt with focus on the forward modelling was conducted within the limits of a Bachelor thesis for the firn core KCO, drilled in the upper firn layers of CG in 2005 [Jepsen, 2010].

In this context it was primary objective of this thesis

- to for the first time measure the dielectric properties of a deep Alpine ice core from surface till bedrock by dielectric profiling (DEP) [Wilhelms, 1996, 2000], and to thoroughly investigate the record with respect to previous knowledge and existing data sets,
- to derive a synthetic radargramms from DEP data by forward modelling on basis of a simple convolution approach [Eisen *et al.*, 2003b], and to establish in how far the features of recorded GPR radargramms could be reproduced therewith.

The thesis comprises data from the cold Alpine[1] glaciers Col du Dôme (CDD) in the Mont Blanc summit range, French Alps, and Colle Gnifetti (CG) in the Monte Rosa region, Swiss Alps. Both are very comparable in most of their features but differ in their annual net-surface accumulation, CDD is characterized by an exceptionally high one, CG by an exceptionally low one. They thus supply complementary records of different resolution and on different time scales.

The thesis is focused on DEP data of the CDM ice core since the core was readily available and uncut after the drilling in September 2012 on CDD in institutional cooperation of *Laboratoire de Glaciologie et Géophysique de'l Environnement (LGGE)*, *Institut für Umweltphysik of University Heidelberg (IUP)* and *Physical Institute of University Berne (PIUB)*, and on a grid of GPR profiles covering the drilling site, recorded by Bohleber [2012, personal communication] during the same campaign. The DEP data had to be measured using a DEP measuring bench of the *Alfred-Wegener-Institut for Polar and Maritime Research (AWI)* [Wilhelms, 1996, 2000]. As the CDM core comprised a comparatively high amount of defects and as the supplied DEP setup did not work faultless, large effort had to be concentrated on the development of corrections to remove artefacts of the DEP raw data, thus forcing an emphasis of the thesis on to the DEP data processing. The GPR profiles had already been processed by Bohleber [2012, personal communication] and remained to be analysed and discussed. The forward modelling was implemented as convolution of a synthetic radar wavelet with the ice core's reflectance profile in the time domain on basis of code by Eisen *et al.* [2003b], its results had to be analysed and discussed.

In the final stage of the thesis it was possible to supplement the data from CDD by DEP data of the KCC core, a new core drilled to bedrock in August 2013 on CG in institutional cooperation of *Institut für Umweltphysik of University Heidelberg (IUP)*, *Physical Institute of University Berne (PIUB)*, *Alfred-Wegener Institut for Polar and Maritime Research (AWI)*, *Department of Geosciences of Université de Fribourg*, *Climate Change Institute of University of Maine*. DEP could be measured this time with fine core quality and a functioning setup. The DEP data could be processed and contributes to the discussion.

For analysis and discussion the thesis could revert to data on chemical concentrations and dating of the CDK ice core [Preunkert et al., 2012, personal communication], drilled at CDD in 2004 adjacent to the CDM core, glaciological parameters of CDD (ice thickness, surface velocities, etc.) [Vincent *et al.*, 2007a, 1997] and DEP and density data of the KCO firn core [Jepsen, 2010].

[2] Note that the reflector-free zone (RFZ) at Colle Gnifetti (CG) is not identical to the polar echo-free zone [Drews *et al.*, 2009].

2 Study Sites

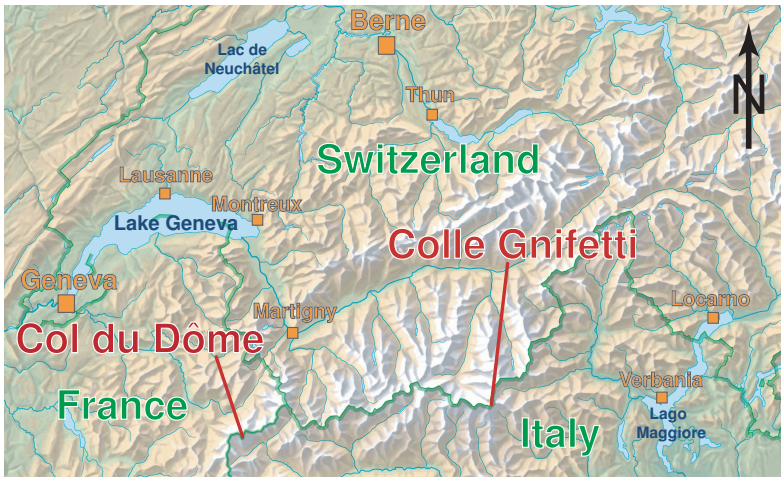

Figure 2.1: Western Alps, geodata © swisstopo.

The present thesis comprises data from the two most investigated high-elevated cold Alpine glaciers, Col du Dôme (CDD) on top of the Mont Blanc massif, French Alps, which is the highest elevation in Europe, and Colle Gnifetti (CG) in the Monte Rosa massif, the highest mountain range in the Swiss Alps. (cf. Figure 2)

2.1 Glaciological Settings

Topography

The two glaciers are both convex saddles located in about the same altitude in the summit regions of two massifs surmounting their far surrounding significantly. They are comparable in dimensions, topographic features and geographic orientation. (cf. Figure 2.2 and Table 2.1)

CDD is ranging from Dôme du Goûter in the west to Mont Blanc summit in the east. In the south it is confined by a steep face. At the faces beyond Dôme du Goûter and Mont Blanc summit crevasses are lying hillsides.

CG is ranging from Signalkuppe in the southeast to Zumsteinspitze in the northwest. On its northeastern flank it is confined by a 100m deep ice cliff. In the western hillside beyond Signalkuppe a bergschrund occurs.

Firn Temperature

Both glaciers are to the present cold glaciers (cf. Figure 2.2 and Table 2.1) and belong to the firn phase *recristallisation-infiltration zone* [Shumskii, 1964] resp. *percolation zone A* [Müller, 1962], meaning that melting events occur only seldom and afflict only the surface layer. They are both frozen to bedrock and are not subject to basal sliding.

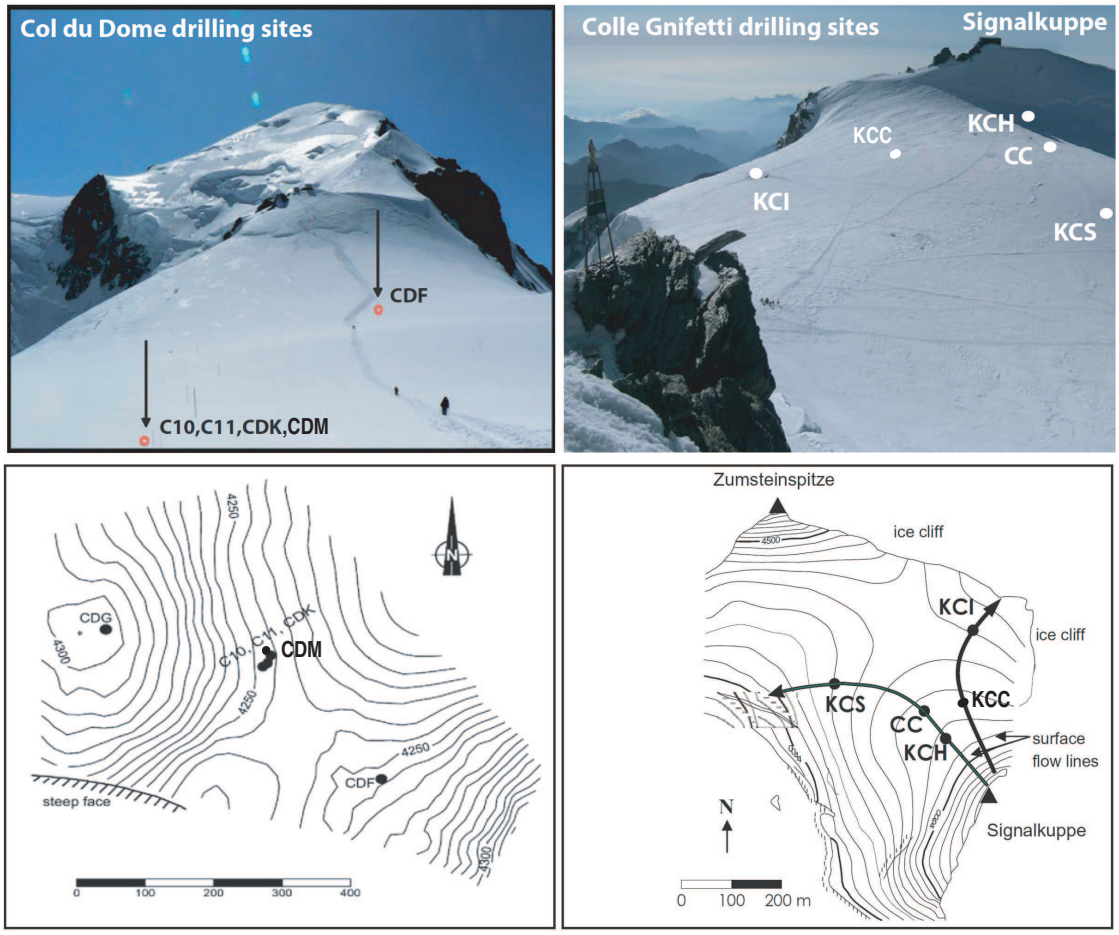

Figure 2.2: Pictures and Maps of Col du Dôme (CDD) and Colle Gnifetti (CG) in the right column. Top left: CDD taken from Dôme du Goûter in the west, looking to Mont Blanc in the east. Drilling sites are marked as red dots. **Top right:** CG taken from Zumsteinspitze, looking to Signalkuppe. Drilling sites are marked as white dots. **Bottom left:** Map of CDD with contour lines in 5m steps. Drilling sites are marked as black dots. **Bottom right:** Map of CG with contour lines in 10m steps. Drilling sites are marked as black dots. Figures modified from Wagenbach *et al.* [2012]

Table 2.1: Properties of the cold Alpine Glaciers Col du Dôme (CDD) and Colle Gnifetti (CG). Sources: [1]≡[Wagenbach *et al.*, 2012], [2]≡[Vincent *et al.*, 2007b], [3]≡[Vincent *et al.*, 2007a], [4]≡[Hoelzle *et al.*, 2011], [5]≡[Wagenbach, 2001], [6]=≡[Luthi and Funk, 2000].

	Col du Dôme (Mont Blanc)		**Colle Gnifetti** (Monte Rosa)	
Altitude / m. a.s.l.	4250	[1]	4450	[1]
Glacier Thickness / m	40-140	[1]	60-120	[1]
Firn temperature (in 20m depth)	-11°C	[2]	-14°C	[4]
Precipitation / m w.e./a	1.7	[1]	1.4	[1]
Net-surface accumulation / m w.e./a	0.2-3.5	[3]	0.1-1	[5]
Surface velocity / m/a	0.5-10	[3]	0.5-2	[6]

ACCUMULATION

Even though both glaciers are comparable in precipitation, temperatures, dimensions, topographic features and geographic orientation, they differ significantly in accumulation (cf. Table 2.1). CDD is characterized by a very high net-surface accumulation and CG by a very little one. Wagenbach *et al.* [2012] explain that this is caused by the different position of the potential snow sinks. I.e. the steep face at CDD is located upwind while the ice cliff at GC is located downwind of the main drilling sites. As consequence of the diametrical accumulation patterns the thickness of annual layers at CDD is high, yielding a good resolution in depth but reaching back only a few hundred years [Preunkert *et al.*, 2000], while the annual layers at CG are thin comprising over the total glacier depth several thousand years [Bohleber, 2008]. The two glaciers thus supply complementary records on different time scales.nnual layers at CG are thin comprising over the total glacier depth several thousand years. The two glaciers thus supply complementary records on different time scales.

MASS BALANCE

Both glaciers have remained in steady state for at least the last century and were not yet afflicted in their morphology by climate changes.

CDD The glacier has been subject to topographic measurements since the late 19th century [Vallot, 1913b,a, Vincent *et al.*, 1997, 2007a], thus it was established that it remained in steady state since at least 100 years before present (BP) and has not yet been affected by climate change [Vincent *et al.*, 2007a].

CG Geodetic measurements since the 1980s and comparisons of photographs from 1893 to 1994 established the glacier to be close to steady state [Luthi and Funk, 2000] for at least the last century [Wagner, 1996]. The saddle of CG has not yet been afflicted by climate warming [Hoelzle *et al.*, 2011].

SUMMARIZED CHARACTERISTICS

COMMON FEATURES	DISSIMILAR FEATURES
• altitude, dimension, topographic features and geographic orientation, • temperature and precipitation, • both glaciers are assumed to be in steady state, • glacier type *recristallisation-infiltration zones* [Shumskii, 1964].	• net-surface accumulations, • wind exposure, • age-depth relations, • time scales of contained climate records.

2.2 PAST RESEARCH

2.2.1 ICE CORE STUDIES

Ice cores have been drilled on both sites since the 1970s. Most of them were firn cores, the drilled deep cores are listed in Table 2.2 displayed in Figure 2.2 with a first core. The cores relevant for this thesis are on CDD the cores CDK (2004) and CDM (2012) and on CG the cores KCO (2005) and KCC (2013).

Table 2.2: Deep ice cores drilled at Col du ôme (CDD), Mont Blanc, and Colle Gnifetti (CG), Monte Rosa. The grey shaded cores are not relevant for the purpose of this thesis.

Cores from COL DÛ DOME (CDD)	**C10**	**C11**	**CDG**	**CDF**	**CDK**	**CDM**
Year	1994	1994	1999	1999	2004	2012
Total depth / m	126*	139*	38.6	101.5	123.1	122.5
Net surface accumulation / m w.e./a	2.22	2.44	0.6±0.2	2.0±0.2	2.6±0.2	2.6±0.2

Cores from COLLE GNIFETTI (CG)	**CC**	**KCS**	**KCH**	**KCI**	**KCO**	**KCC**
Year	1982	1995	1995	2005	2005	2013
Total depth / m	64.1	100.0	60.3*	61.8*	25.8**	71.9
Net surface accumulation / m w.e./a	0.22	0.51	0.23	0.14	0.14	***

*Drilling may not have reached bedrock.

**Firn core, bedrock is supposed to lie below 62m.

***Not yet available as just recently drilled.

DEPOSITION OF AEROSOL-RELATED SPECIES

The records of past impurity depositions on CDD and GC are highly correlated. Their joint data sets on short (CDD) and long (CG) time scale supply a *quasi-complete reconstruction of past atmospheric aerosol load and composition over Europe since 1920* [quote from Preunkert and Legrand, 2013]. They reveal a general transition of the Alpine snow chemistry from a slightly alkaline regime to an acid one over the past 100 years [Wagenbach *et al.*, 1988, Wagenbach and Geis, 1989, Wagenbach *et al.*, 2012]. (cf. Figure 2.3)

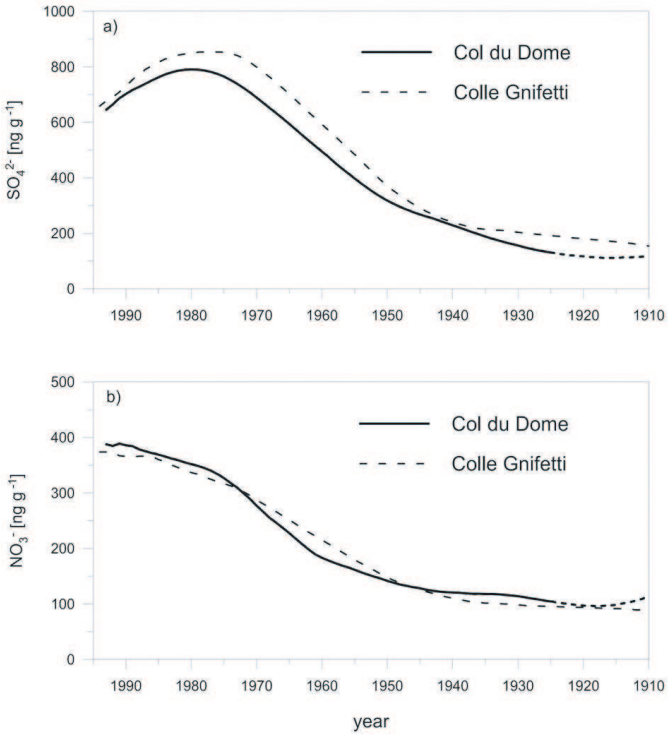

Figure 2.3: Long term trend of deposition of main contributors to acidity, sulphate and nitrate, at Col du Dôme (CDD) and Colle Gnifetti (CG). Distinctly visual is a transition in ice chemistry from a slightly alkaline regime before 1950 to an acid regime afterwards. Figure from Wagenbach *et al.* [2012].

AGE-DEPTH RELATIONS

Alpine ice core dating usually is conducted by counting of annual cycles in aerosol deposition [Preunkert *et al.*, 2000] and the identification of absolute time markers like the 1963 tritium peak, Saharan dust depositions in 1977, 1947 and 1901 and the eruption of the volcano Katmai in 1912. The age-depth relations of drilling sites on both CDD and CG are displayed in Figure 2.4. Apparently they become non-linear after about half the total depth, thus displaying strong layer thinning and illustrating the difficulty of simple dating approaches by layer counting.

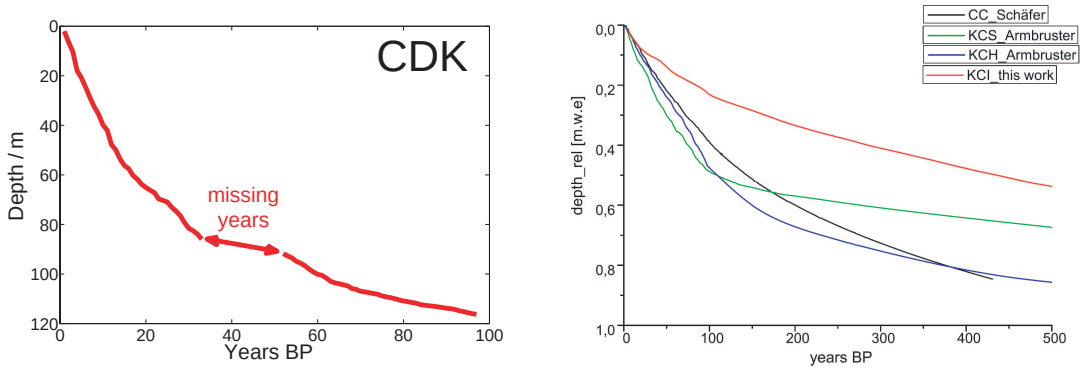

Figure 2.4: Age-depth profiles at Col du Dôme and Colle Gnifetti. On the left: Age-depth profile of the CDK core. Data from Preunkert et al. [personal communication]. **On the right:** Age-depth profiles from the cores CC, KCS, KCH and KCI. Figure from Bohleber [2008].

MISSING YEARS

The layer counting while the dating of the CDK core revealed a gap in the time scale, i.e. 'missing years' between 1955 and 1970 (cf. Figure 2.4), that's origin has not yet been understood but is assumed to stay in connection with the crevasse upstream CDD on the flank of Dôme du Goûter [Waldner, 2011].

ANOMALOUS LEAD CONCENTRATIONS AT CDD

A further peculiarity of CDD was detected in the analysis of the cores C10 and C11 [Vincent *et al.*, 1997], CDK [Waldner, 2011] and CDM [Zipf, 2013] for the lead radio isotope ^{210}Pb . All core's ^{210}Pb-activity-depth profiles display below a depth of ca. 85m a distinguishable peak, the so-called ^{210}Pb anomaly, that can not be accounted for with any deposition event at the surface and is assumed to stay in connection with the crevasse upstream CDD too [Vincent *et al.*, 1997, Waldner, 2011, Zipf, 2013].

2.2.2 GROUND PENETRATING RADAR SURVEYS

Past GPR surveys have been conducted on both glaciers to determine ice thickness and basal properties and to investigate the internal structure.

CDD Investigations have been conducted for:

- ice thickness and bedrock topography [Vincent *et al.*, 1997, Böhlert, 2005],
- internal structure [Bohleber, 2012, personal communication].

The recent survey on CDD by Bohlber [2012, personal communication] will enter into this thesis.

CG Investigations have been conducted for:

- ice thickness and bedrock topography [Wagner, 1996, Luthi and Funk, 2000],
- extrapolation and comparison of ice core properties [Eisen *et al.*, 2003a, Bohleber, 2011, Konrad, 2011, Konrad *et al.*, 2013],
- suitable drilling sites [Böhlert, 2005].

REFLECTOR-FREE ZONE AT COLLE GNIFETTI

At CG Eisen *et al.* [2003a] observe that internal reflecting horizons (IRH) in radargramms are no longer distinguishable below the firn-ice transition in a depth of about 30 to 50 meters, a phenomenon they describe as reflector-free zone (RFZ). This is probably not caused by mere attenuation as polar experiences with GPR at 250MHz show, that the tracing of IRH in several 100m depth is possible and that reflectors generally do not vanish until a few hundred meters above the bedrock, a phenomenon at polar sites referred to as echo-free zone [Drews *et al.*, 2009]. The authors argue that the RFZ at CG might possibly originate from the combined vanishing of larger gradients both in density or acidity below this depth. They point out that this naturally is expected for density, as below the firn-ice transition only ice exists and density variabilities thus are limited, but that one could still expect strong variabilities in acidity, e.g. from volcano peaks. They however find that the firn-ice transition for CG lies in a depth corresponding ca. to the year 1950 when the ice chemistry changed from a slightly alkaline regime before to a acidic regime after (cf. Figure 2.3). The authors indicate that a combination of these two effects might be responsible for the occurrence of the RFZ. After proving the existence of reflections from changes in crystal-orientation fabric (COF) [Eisen *et al.*, 2007] Eisen [2012, personal communication] further indicate a possibility that coherent reflections from below the firn-ice transition are overlain, and thus masked, by strong incoherent backscatter from abrupt changes in crystal orientation changes.

2.2.3 FLOW MODELLING

At CDD a 2D flow simulation approach with the finite-element method has been conducted by Vincent *et al.* [1997], Gagliardini and Meyssonnier [1997]. On CG flow modelling approaches have been conducted in 2D by Haeberli *et al.* [1988], applying a flow law for firn using the finite-element method in 3D by Wagner [1996], Luthi and Funk [2000] and recently based on the approach of Vincent *et al.* [1997] in 2.5D by Konrad [2011] (cf. Appendix C).

3 PHYSICAL BASICS AND GLACIOLOGICAL METHODS

3.1 ELECTRODYNAMICS OF ICE

Ice responds to external electric fields frequency-dependent by polarisation and conduction but does not display magnetic response.

POLARISATION Two mechanisms contribute to polarisation, atomic polarisation (i.e. the induction of dipole moments in the atoms through the electric field, often depicted as the relative shifting of the molecular electron cloud against the lattice of atomic cores) and dipolar polarisation (i.e. the orientation of the permanent dipole moments of the water molecules in the electric field).

The relaxation time for atomic polarisation lies in the infrared way above radar or dielectric profiling (DEP) frequencies. Hence atomic polarisation can be neglected in regard to radar measurements or dielectric profiling (DEP). The relaxation time for dipolar polarisation, however, lies in the μs-range yielding a relaxation frequency in the kHz-range at the lower boundary of the radar and DEP spectrum. Dipolar polarisation consequently afflicts radar or DEP application in ice.

CONDUCTION The conduction depends on the diffusion of ionic defects (i.e. OH^- or H_3O^+ ions embedded into the crystal lattice instead of a H_2O molecule) and Bjerrum defects (i.e. bonds with two electrons instead of one, so-called D-defects, or without any electron, so-called L-defects) [e.g. Bogorodskiĭ *et al.*, 1985, Petrenko and Whitworth, 1999].

A theoretical derivation of the frequency-dependent dielectric properties of mono-crystalline ice has been established in formal correspondence to the model of Debye [1929] by Jaccard's theory of conduction [Gränicher *et al.*, 1957, Jaccard, 1959, 1965, 1967] outlined e.g. in Bogorodskiĭ *et al.* [1985], Petrenko and Whitworth [1999].

3.1.1 FIELD EQUATIONS

Electrodynamics in homogeneous snow, firn or ice are determined by the Maxwell Equations [Maxwell, 1881] in matter with simple linear constitutive relations. Conduction can be assumed to be ohmic [Petrenko and Whitworth, 1999]. The corresponding equations can be found in any textbook on classical electrodynamics, e.g. in Jackson [1999].

MAXWELL EQUATIONS		CONSTITUTIVE RELATIONS		OHM'S LAW
$\nabla \times \mathbf{E} = -\frac{\partial}{\partial t}\mathbf{B}$	$\nabla \mathbf{D} = \rho$			
		$\mathbf{D}=\varepsilon_0 \boldsymbol{\varepsilon}' \mathbf{E}$	$\mathbf{B} = \mu_0 \boldsymbol{\mu}' \mathbf{H}$	$\mathbf{j} = \boldsymbol{\sigma} \mathbf{E}$
$\nabla \times \mathbf{H} = \mathbf{j} + \frac{\partial}{\partial t}\mathbf{D}$	$\nabla \mathbf{B} = 0$			

$\boldsymbol{\varepsilon}'$ is the real relative permittivity, $\varepsilon_0 = 8.854187817 \cdot 10^{-12}\mathrm{AsV^{-1}m^{-1}}$ [Gerthsen and Meschede, 2010] the vacuum permittivity, $\boldsymbol{\mu}'$ the real relative permeability, $\mu_0 = 1.2566370614 \cdot 10^{-6}\mathrm{VsA^{-1}m^{-1}}$ the vacuum permeability [Gerthsen and Meschede, 2010], ρ the density of free electric charges, $\mathbf{j}$ the density of free electrical currents and $\boldsymbol{\sigma}$ the electrical conductivity. Dashes $'$ emphasize dimensions to be real.

ANISOTROPY Glacier ice hitherto has been found in only one of fourteen possible solid phases of water, i.e. as hexagonal crystal with uniaxial symmetry frequently referred to as I_h. The properties of mono-crystalline ice are anisotropic and depend on the orientation against its c-axis. Snow and firn however are poly-crystalline with randomly orientated grains and are macroscopic isotropic. Hence, for mono-crystalline ice the real relative permittivity $\boldsymbol{\varepsilon}'$, the real relative permeability $\boldsymbol{\mu}'$ and the electrical conductivity $\boldsymbol{\sigma}$ are tensors of 2nd order. For poly-crystalline snow and firn, however, they are reduced to scalars ε, ε' and σ.

COMPLEX RELATIVE PERMITTIVITY It is usual to define a complex relative permittivity $\boldsymbol{\varepsilon}$ for time-harmonic alternating electrical fields $\mathbf{E}(\omega,t) = \mathbf{E}_0(\omega)e^{i\omega t}$. This allows a formal simplification of Ampère's law.

$$\boldsymbol{\varepsilon} = \boldsymbol{\varepsilon}' - i\boldsymbol{\varepsilon}'' = \boldsymbol{\varepsilon}' - i\frac{\boldsymbol{\sigma}}{\omega\varepsilon_0} \qquad \text{with} \qquad \boldsymbol{\varepsilon}'' = \frac{\boldsymbol{\sigma}}{\omega\varepsilon_0} \tag{3.1}$$

$$\Longrightarrow \nabla \times \mathbf{H} = \mathbf{j} + \frac{\partial}{\partial t}\mathbf{D} = \boldsymbol{\sigma}\mathbf{E}(\omega,t) + \varepsilon_0\boldsymbol{\varepsilon}'(\omega)\frac{\partial}{\partial t}\mathbf{E}(\omega,t) = i\omega\varepsilon_0\left(\boldsymbol{\varepsilon}'(\omega) - i\frac{\boldsymbol{\sigma}}{\omega\varepsilon_0}\right)\mathbf{E}(\omega,t)$$

The real part $\boldsymbol{\varepsilon}'$ corresponds to the real relative permittivity while the imaginary part $\boldsymbol{\varepsilon}''$ represents losses from ohmic conduction and dielectric polarisation, which can be quantified by a loss tangent $\tan\delta = |\boldsymbol{\varepsilon}''|/|\boldsymbol{\varepsilon}'| = \varepsilon''/\varepsilon'$. Note that in general further attenuation losses have to be considered by a further imaginary contribution $\boldsymbol{\varepsilon}''_{loss}$, yielding $\boldsymbol{\varepsilon} = \boldsymbol{\varepsilon}' - i(\boldsymbol{\varepsilon}'' + \boldsymbol{\varepsilon}''_{loss}) = \boldsymbol{\varepsilon}' - i(\frac{\boldsymbol{\sigma}}{\omega\varepsilon_0} + \boldsymbol{\varepsilon}''_{loss})$.

3.1.2 WAVE PROPAGATION

PHASE VELOCITY Regarding the wave speed of electromagnetic radiation, ice is commonly assumed to be a low-loss material, in which wave propagation takes place loss-less in charge- and current-free space $\rho \approx 0$, $\mathbf{j} \approx 0$, thus yielding harmonic wave equations with wave speed c. The assumption is justified since $\varepsilon'' << \varepsilon'$ (cf. Section 3.1.3) in the MHz to GHz range holds.

$$c = \frac{c_0}{\sqrt{\varepsilon'}} \tag{3.2}$$

For the vacuum light velocity holds $c_0 = 2.99792458 \cdot 10^8 \mathrm{ms}^{-1}$ [Gerthsen and Meschede, 2010].

REFLECTION COEFFICIENT In case of the reflection coefficient R at boundaries between adjacent layers, reflections may also stem from changes in the imaginary part. Thus, the full complex permittivity is considered. R depends via the complex refraction indices $n_{1,2} = \sqrt{\varepsilon_{1,2}}$ on the complex relative permittivities $\varepsilon_{1,2}$ of the two layers.

$$R = \frac{n_1 - n_2}{n_1 + n_2} = \frac{\sqrt{\varepsilon_1} - \sqrt{\varepsilon_2}}{\sqrt{\varepsilon_1} + \sqrt{\varepsilon_2}} \tag{3.3}$$

3.1.3 DIELECTRIC PROPERTIES

The dielectric properties of pure ice depend on the

- frequency of the applied electric field,
- dielectric anisotropy,
- temperature.

As natural cold snow, firn and glacier ice are two-component mixtures of ice and air, their complex relative permittivity ε_F depends in mixed contributions on those of their constituents as on their volume

fractions. Furthermore real samples can contain varying concentrations of impurities. Their dielectric properties depend additionally on

- density,
- contained impurities.

An overview over empirical values for the real relative permittivity and electrical conductivity of polar snow, firn and ice is given in Table 3.1.

Table 3.1: Empirical values for the high-frequent real relative dielectric permittivity ε'_∞ and the high-frequent electric conductivity σ_∞.

Material	ε'_∞	σ_∞ / μS/cm	**Conditions**	**Source**
Polar Ice	3.15	0.090	f>10kHz, T=-15C, $\rho = 917$kg/m^3	[Wolff, 1995]
	3.12	0.002	f>10kHz, T=-50C, $\rho = 917$kg/m^3	[Wolff, 1995]
	$3.12 - 3.19$	—	f>1MHz, T=-20C, $\rho = 917$kg/m^3	[Fujita *et al.*, 2000]
	3.18	—	f>10MHz, T=-20C, $\rho = 917$kg/m^3	[Bohleber *et al.*, 2012]
Polar Firn	1.67	0.022	f>10kHz, T=-15C, $\rho = 350$kg/m^3	[Wolff, 1995]
Alpine Firn	1.8	0.002	f=250kHz, T=-19C, $\rho = 450$kg/m^3	[Jepsen, 2010]
	2.8	0.005	f=250kHz, T=-19C, $\rho = 800$kg/m^3	[Jepsen, 2010]

FREQUENCY DEPENDENCE For the frequency-dependent dielectric properties of ice holds corresponding to theory [Gränicher *et al.*, 1957, Jaccard, 1959, 1965, 1967] and empirical results (cf. Figures 3.1 and 3.2) at the

LOW-FREQUENT LIMIT Dipolar polarisation dominates, the permanent dipole moments of the water molecules are all orientated, and the static real relative permittivity amounts at its maximum to $\varepsilon'_s \approx 100$ [Fujita *et al.*, 2000]. DC conduction prevails.

RELAXATION FREQUENCY The permanent dipole moments can no longer follow the oscillation of the field, ε' drops rapidly in the kHz range around the relaxation frequency f_r [Bohleber *et al.*, 2012, Fujita *et al.*, 2000]. The imaginary part ε'' displays a minimum and the loss tangent $\tan\delta$ reaches a maximum [Fujita *et al.*, 2000].

HIGH-FREQUENT LIMIT The real part converges against $\varepsilon'_\infty = 3.18 \pm 0.01$ in the MHz- to GHz-range [Bohleber *et al.*, 2012]. Loss rapidly decreases hence in the MHz- to GHz-range, the range of DEP and radar frequencies, ice is a low-loss medium with $\varepsilon'' << \varepsilon'$. AC conduction prevails.

DEPENDENCE ON DENSITY – MIXING FORMULAE Neglecting complex mixing, i.e. the weak contribution of the constituents imaginary parts to the real relative permittivity of the composite, one can use a relation supplied by Roth *et al.* [1990], which describes the real relative permittivity ε' of a more-component mixture in dependence of the relative permittivities of its constituents ε'_i and their volume fractions $v_i = V_i/V$ with $V = \sum_i V_i$.

$$\varepsilon' = \sum_i v_i \varepsilon_i'^{\alpha}, \qquad \alpha \in [-1, 1] \tag{3.4}$$

In glaciology widely used is a two-component version of this formula with $\alpha = 1/3$, the so-called mixing formula of Looyenga [1965], which Glen and Paren [1975] applied for cold snow, firn and glacier ice as composites of ice and air,

$$\varepsilon'_F = \left(v_I \left(\sqrt[3]{\varepsilon'_I} - \sqrt[3]{\varepsilon'_A} \right) + \sqrt[3]{\varepsilon'_A} \right)^3 \tag{3.5}$$

with the indices F for the composite snow, firn or glacier ice, I for pure ice and A for air. A handy semi-empirical fit for the real relative permittivity ε'_F of firn in dependence of its density ρ_F has been derived from (3.4) with $\alpha = 1/2$ by Kovacs *et al.* [1995].

$$\varepsilon'_F = \left(1 + 0.000845\rho_F \cdot \frac{\mathrm{m}^3}{\mathrm{kg}}\right)^2 \tag{3.6}$$

Considering complex mixing Wilhelms [2005] derived a theory of density-conductivity mixed permittivity (DECOMP) by complex continuation of the mixing formula of Looyenga [1965], the assumptions $\varepsilon_A = 1$ and negligence of the air content's contribution to the volume fraction $v_A\rho_A \approx 0$.

$$\varepsilon_F = \left(\frac{\rho_F}{\rho_I}\left(\sqrt[3]{\varepsilon_I} - 1\right) + 1\right)^3 \tag{3.7}$$

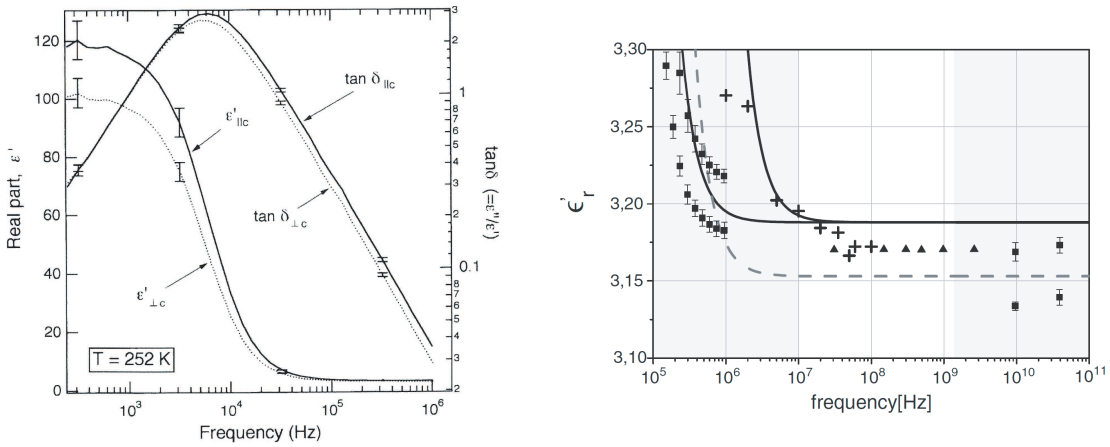

Figure 3.1: Frequency dependency of the real relative permittivity ε' On the left: Depicted are the perpendicular and parallel part in regard to the ice's c-axis of the real relative permittivity ε' and the corresponding loss tangents $\tan\delta$. **On the right:** Depicted are measured values and curves (Debye model) of the real relative permittivity ε'. Note the range of values at radio frequencies. The left Figure is taken from Fujita *et al.* [2000], the right from Bohleber *et al.* [2012].

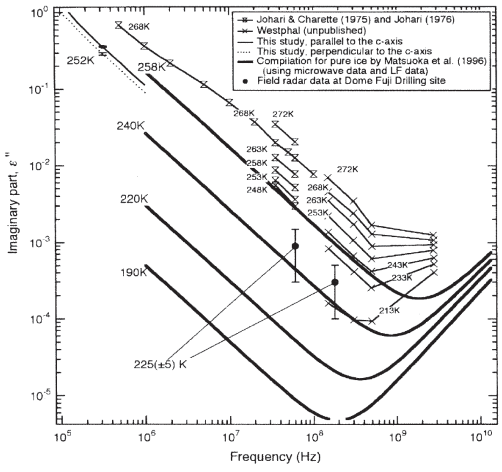

Figure 3.2: Frequency dependency of the imaginary ε'' part of the complex relative permittivity. The Figure is taken from Fujita *et al.* [2000].

3.2 INTRODUCTION OF THE APPLIED METHODS

3.2.1 GROUND PENETRATING RADAR

The use of radar systems in glaciology dates back to first attempts of Waite to measure the ice thickness with radar bursts in 1957 [Waite and Schmidt, 1962]. It was inspired by the virtual realisation of ice as an low loss medium for radar waves (cf. Section 3.1.3) by pilots crossing it with aeroplanes using early radar altimeters in the 1930s. Since radar has become a standard tool and is operated spaceborn, airborn or on the ground on polar as on alpine sites to measure e.g. the ice thickness [e.g. Böhlert, 2005], investigate the internal stratigraphy of glaciers [e.g. Bohleber, 2011], determine surface accumulations [e.g. Steinhage *et al.*, 2013], etc. Within the subject it is referred to as ground-penetrating radar (GPR), ice (penetrating) radar, or particularly for airborne systems as radio-echo sounding (RES).

RADAR SYSTEMS

Radar systems generally comprise transmitter (TX), receiver (RX), control unit and recording system. Electromagnetic waves or wave pulses are generated and emitted by TX and after travelling along various paths to and fro reflectors recorded by RX as functions of their so-called two-way traveltime (TWT).[3] (cf. Figure 3.3).

The data of this thesis was collected using a common bistatic impulse radar systems operated in common offset (CO) mode, for which with TX and RX are mounted with fixed distance on a mobile platform that is moved along a profile while recording.

RESOLUTION Navarro and Eisen [2009] report for the vertical resolution Δz_{GPR} a theoretically value of about one quarter $\lambda/4$ wavelength and unto one half wavelength $\lambda/2$ in praxis. For the horizontal resolution Δx_{GPR} they report a generally depth dependence but for properly migrated areas of a radargramm constant values of $\lambda/2$ for distances of less than $\lambda/4$ between adjacent radar traces. Yet in case of an impulse radar not the wavelength of the carrier wave but the length of the pulse is decisive.

RADAR REFLECTORS AND INTERNAL REFLECTING HORIZONS

Radar reflectors arise from gradients of the dielectric properties along the wave path. In glacier ice such are caused according to the strength of their contribution by

- changes in density [Paren, 1975, Clough, 1977],
- changes in acidity [Hammer, 1980, Moore, 1988],
- changes in crystal-orientation fabrics (COF) [Eisen *et al.*, 2007, Matsuoka *et al.*, 2003, Fujita *et al.*, 1993]

Furthermore reflectors occur at transitions between air, ice, water and bedrock.

Spatially extensive internal reflectors, i.e. coherent layers of dielectric contrast, are referred to as internal reflecting horizons (IRH), and are interpreted as isochrones [Robin *et al.*, 1969].

ALLOCATION Simple mono- or bistatic GPR systems are not able to separate the contributions to a recorded trace spatially. Each radar trace contains a one-dimensional data record that is usually interpreted as back scatter from vertically aligned reflectors below the GPR's coordinate at the glacier surface, even

[3] i.e. the traveltime between emission of the wave by TX and its recording by RX, where "two-way" figuratively describes the situation of closely arranged RX and TX were the wave travels twice on the same path (once to and once fro) between RX/TX and reflector.

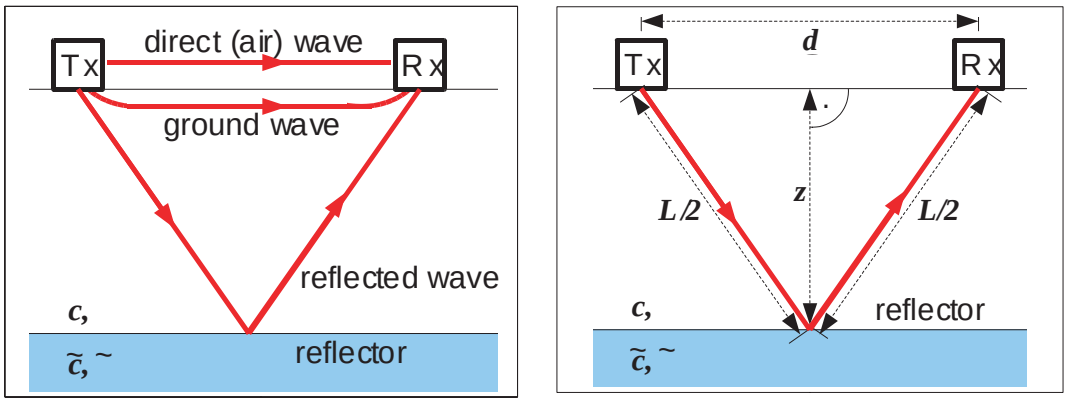

Figure 3.3: On the left: Principle bistatic ground penetrating radar (GPR) setup comprising a transmitter (TX) and a receiver (RX). Electromagnetic waves or wave pulses are generated and emitted by TX and after travelling along various paths to and fro reflectors recorded by RX as functions of their so-called two-way traveltime (TWT). As prominent peaks appear for small TWT the direct air wave and the horizontal ground wave, who are usually eliminated from the data by static correction at the beginning of the GPR processing. **On the right: Conversion of TWT to depth** exemplified for a coplanar composition of surface and internal reflecting horizon (IRH) with homogeneous layer with phase velocity $c = const.$ in between. For the path length holds $L = t_{TWT} \cdot c$ and in case of $d << L$ for the depth $z = t_{TWT} \cdot c/2$. Both Figures are from Konrad [2011].

though it inevitably contains back scatter from reflectors from all directions in space. Thus a radar trace might display for a certain TWT a so-called allocated reflector, that was not located vertically beneath the GPR but might lie anywhere else on a sphere with the same TWT. In Figure 3.4 one might study this phenomenon for an allocated point reflector and for an allocated bedrock reflector.[4]

MIGRATION For simple plain geometries with coplanar surface, internal layering and bedrock the problem of allocation is reduced to two dimensions and thus solvable. Considering a singular strong reflector of an planar IRH, it would appear in the radargramm as distinguishable downward-open hyperbolae (cf. Figure 3.4) as it would not only appear in the trace vertically tangenting it but also allocated in the neighbour traces. After two-way-traveltime-depth conversion the allocated reflectors can be shifted back into the plane of the IRH by simple trigonometric relations. This is called two-dimensional migration and regularly applied in GPR processing.

In complex geometries however the three-dimensional migration of allocated reflectors back to their actual position is with two-dimensional radar data impossible. Thus leaving large unquantifiable uncertainties.

A more comprehensive introduction on radar techniques and applications in glaciology can be found in Navarro and Eisen [2009], Bogorodskiĭ *et al.* [1985].

3.2.2 Conversion of Two-Way Traveltime to Depth

As GPR records reflectors against two-way traveltimes (TWT) the resulting radargramms do not immediately reveal information like the ice thickness, wherefore a conversion of TWT to depth is necessary. This however requires the knowledge of the wave speed c along the wave path (cf. Equation (3.2)).

[4] But it holds in general for all kinds of reflectors, as any kind of reflector can be separated into point reflectors.

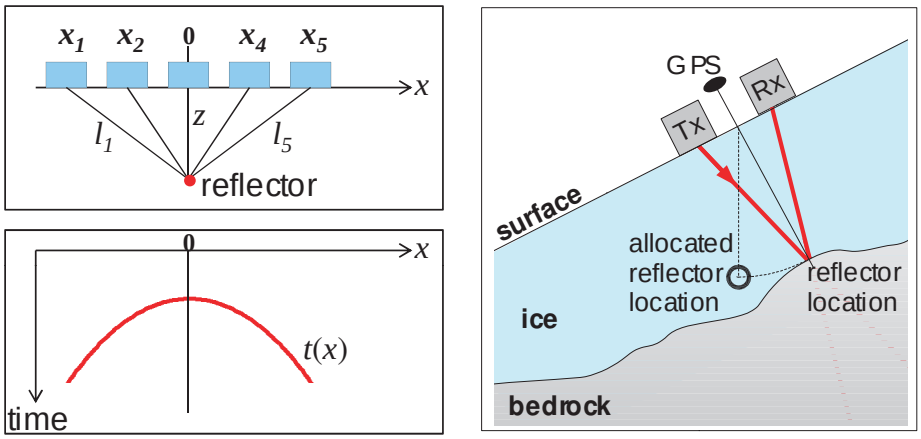

Figure 3.4: On the left: Allocation of a point reflector. A point reflector in depth z that is vertically below position x_0 is located correctly in a radar trace recorded from the GPR at position x_0, yet the GPR at position x_5 records it too and allocates it to a point vertically below x_5 in the depth of $l = \sqrt{z^2 + (x_5 - x_0)^2} > z$. Due to the phenomenon of allocation the point reflector is recorded in the radargramm as hyperbolae. For distinguished point reflectors distinguished hyperbolae are visible.
On the right: Allocation of a bedrock reflectors. Allocation naturally applies for bedrock reflectors too. As they usually are distinguished in comparison to their surrounding, bedrock becomes blurred.
The Figures are from Konrad [2011].

A local velocity profile can be derived e.g. from GPR studies in common midpoint (CMP)[5] mode as TWT-dependent $c(t_{TWT})$ or from dielectric profiling (DEP) of an ice core adjacent to a radar profile as depth-dependent $c(z)$.

If the velocity profile is not known, the assumption of a simple coplanar composition of surface and IRH with an homogeneous layer with $c = const.$ in between (like depicted in Figure 3.3) yields a simple analytic relation between TWT t_{TWT}, wave-path length L antennae distance d and depth z which can be further simplified for large path lengths and small antennae distances $d << L$

$$L = t_{TWT} \cdot c \quad \text{and} \quad z = \frac{1}{2}\sqrt{L^2 - d^2} \overset{d<<L}{\approx} \frac{L}{2} = \frac{t_{TWT} \cdot c}{2}$$

However as the velocity depends via permittivity on density, which increases with depth, the above assumption bears a large error and can only give an estimate.

If $c(z)$ respectively $c(t_{TWT})$ along the wave path is known one can derive more precise implicit continuous or discrete conversion formulae, e.g.

$$t_{TWT}(z) = 2\int_0^z \frac{dz'}{c(z')} = 2 \cdot \sum_i \frac{z_{i+1} - z_i}{c(z_i)} \tag{3.8}$$

Note that the above conversion holds only for radar traces close to the position of the local velocity profile. Yet, if bedrock is recorded continuously, it can be extrapolated along the radargramms by scaling it to the ice thickness. This involves the assumption that the density-depth profile for relative depths to ice thickness was preserved along the radargramm.

[5] Common Midpoint (CMP): Radar traces are recorded for step-wise enlarged distances between TX and RX maintaining a common midpoint.

3.2.3 DIELECTRIC PROFILING

Dielectric profiling (DEP) is a non-invasive method for the measurement of the dielectric properties of ice cores. It measures capacitance and conductance between curved electrodes shifted along the core with alternating currents in the kHz-range. The method was first developed by Moore and Paren [1987], who searched for a more reliable way to measure acidity and detect volcanic peaks in polar ice core records then provided by the previous electrical conductivity method (ECM) [Hammer, 1980].[6] Moore [1993] enhanced the method in its resolution, Wilhelms [1996], Wilhelms *et al.* [1998] introduced a new guarded-electrode geometry enhancing the precision of the measurements and Wilhelms [2000] conducted the last instrumental refinements further improving the method's precision.

APPLICATIONS

DEP is widely used in glaciology both in the field and in the laboratory, e.g. for the

- dating of ice cores by volcanic records [e.g. Cole-Dai *et al.*, 2013, Moore and Paren, 1987]
- determination of past accumulation rates [e.g. Hofstede *et al.*, 2004, Oerter *et al.*, 2000]
- investigating the conduction mechanisms in ice [e.g. Stillman *et al.*, 2013]
- improvement of the understanding of ground penetrating radar (GPR) reflectors [e.g. Drews *et al.*, 2012, Eisen *et al.*, 2003b,c]

DEP BENCH OF THE AWI

The DEP bench of the Alfred-Wegener Institute for Polar and Maritime Research (AWI) [Wilhelms, 2000, Wilhelms *et al.*, 1998, Wilhelms, 1996] (cf. Figure 3.5) used in this study comprises a static long lower frame holding the ice cores and acting in measurements as high electrode and a movable short upper frame carrying the measuring low electrode, which is embedded into a guard electrode on the same potential. The guard electrode's task consists in shielding the low electrode from boundary effects of the electromagnetic field. While measurements the upper frame is shifted stepwise by a step motor along the lower frame. The bench is controlled by a LCR-Meter measuring via the electrodes capacitance and conductance while supplying the alternating current for the electrodes and triggering the motor controller thus controlling the motor. The measured data is exported in real time to a common PC.

UNCERTAINTIES

Principle uncertainties of the measurements derive from the system's precision, i.e. mainly the LCR-meter's specification and calibration, and from air gaps between the electrodes and the ice core or air gaps to to ice core defects. For the derived dielectric properties Wilhelms [2000] reports maximum relative errors of 3.5% for permittivity and 7.5% for conductivity. The depth resolution of the AWI-DEP bench lies without precise specification in the mm-scale and is determined by the length of the low electrode, which is 10mm [Wilhelms, 2000].

DIELECTRIC ICE CORE PROPERTIES FROM DEP MEASUREMENTS

DEP measurements of polar firn established the measured dimensions capacitance and conductance to depend in mixed contributions, besides on the dielectric properties of its constituents pure ice and air, on the firn's content of impurities, i.e. concentrations of acid, salt and ammonia [Moore *et al.*, 1990, 1992, 1994,

[6] ECM measured DC conductivity between two scratching electrodes moved along the polished surface of an ice core yielding results highly sensitive to the contact pressure of the electrodes.

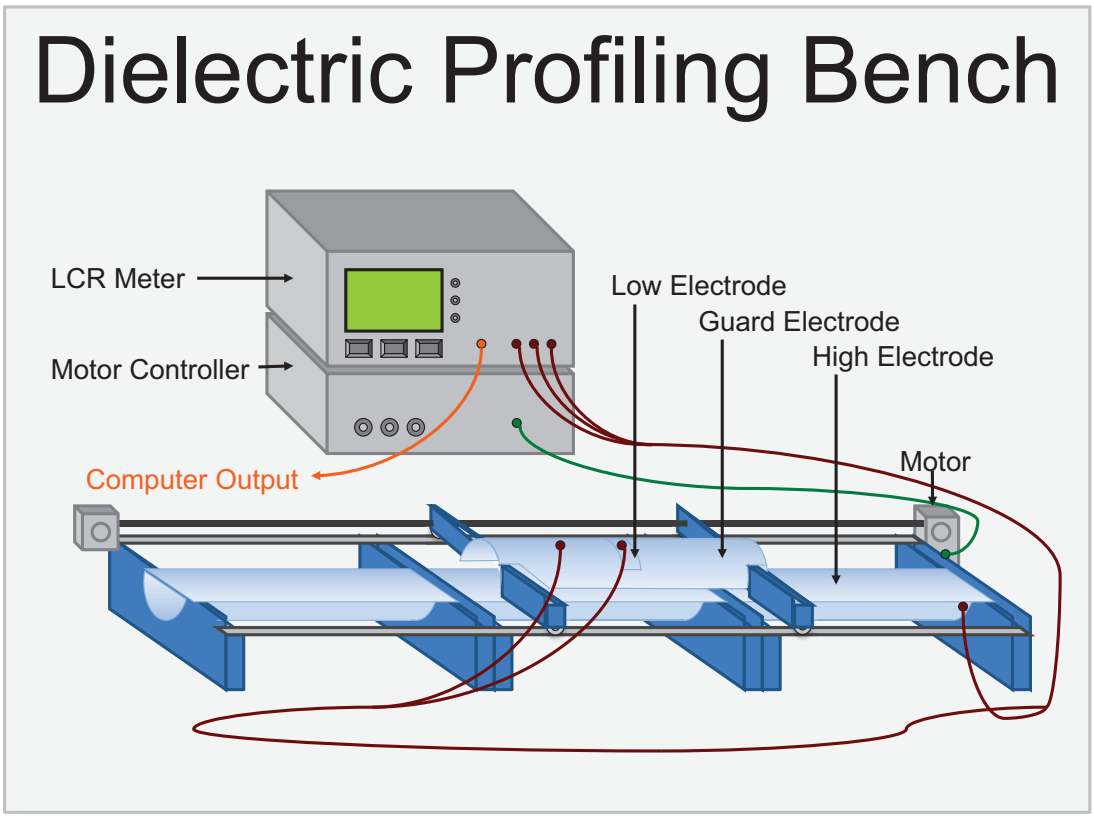

Figure 3.5: Dielectric profiling (DEP) bench of the Alfred-Wegener Institute (AWI), designed by Wilhelms Wilhelms [2000], Wilhelms *et al.* [1998], Wilhelms [1996]. The DEP bench essentially is a cylindrical capacitor measuring capacitance C and conductance G for alternating currents in the kHz-range. It comprises a static long lower frame holding the ice cores and acting in measurements as high electrode and a movable short upper frame carrying the measuring low electrode, which is embedded into a guard electrode on the same potential. The guard electrode's task consists in shielding the low electrode from boundary effects of the electromagnetic field. While measurements the upper frame is shifted stepwise by a step motor along the lower frame. The bench is controlled by a LCR-Meter measuring via the electrodes C and G while supplying the alternating current for the electrodes and triggering the motor controller thus controlling the motor. The measured data is exported in real time to a common PC.

Wolff, 1995, Wolff *et al.*, 1997a][7] and its density [Moore, 1988, Wilhelms, 1996, Wilhelms *et al.*, 1998, Wilhelms, 2000]. Thereby the density enters mainly into the real part and the impurities' concentrations mainly into the imaginary part.

DEP measurements of capacitance C and conductance G of a core allow in principle to derive

- the real relative permittivity ε' and electric conductivity σ,
- the content of acid, ammonia and salt,
- the density ρ.

Derivation of real relative Permittivity and electrical Conductivity The dielectric properties of a core are derived from the measurements with the equations (3.9) and (3.10) [cf.

[7] ECM on the other hand responds only to acidity [Moore *et al.*, 1992, 1994, Wolff, 1995].

Wilhelms, 1996].

$$\varepsilon' = \frac{C}{C_0}, \tag{3.9}$$

$$\sigma = \frac{\varepsilon_0 \cdot G}{C_0} \tag{3.10}$$

$C \equiv$ capacitance of the core $\quad C_0 \equiv$ empty capacitance

$G \equiv$ conductance of the core $\quad \varepsilon_0 \equiv$ vacuum permittivity

DEPENDENCE OF CONDUCTIVITY ON CHEMICAL CONCENTRATIONS Wolff [1995], Wolff *et al.* [1997a] derived from the GRIP ice core at -15C an empirical calibration of the conductivity measured with DEP, depending on the intrinsic conductivity of pure ice and concentrations of acid, ammonia and salt,

$$\sigma = 9 + 4[\mathrm{H^+}] + 1[\mathrm{NH_4^+}] + 0.55[\mathrm{Cl^-}] \tag{3.11}$$

where σ is in μS/m and the chemical concentrations are in μmol/l. Used on polar ice cores [e.g. cf. Stillman *et al.*, 2013] the calibration has not been confirmed for Alpine core's.

DERIVATION OF DENSITY (cf. Section 3.1.3) For known properties of pure ice and air DEP allows with high precision the determination of the measured core's density. Neglecting complex mixing the dependence of the real relative permittivity of the firn on its density can be described by the Looyenga mixing model [Looyenga, 1965] (cf. Equation (3.5)) with a relative error of 10% [Wilhelms, 2005] or semi-empirically with an larger error by the formula from Kovacs *et al.* [1995] (cf. Equation (3.6)).A precise dependence within a relative error of 1% [Wilhelms, 2005] can be described by the theory of density-conductivity mixed permittivity (DECOMP) of Wilhelms [2005] (cf. Equation (3.7)).

3.2.4 FORWARD MODELLING

The principal aim of forward modelling is to establish a physical connection between dielectric ice core profiles, e.g. from dielectric profiling, and radar reflectors in local traces, thus enabling the transfer of ice core properties and datings onto internal reflecting horizons (IRH) and the spatially extrapolation of ice core properties along radar profiles. Past approaches by simple comparisons and investigations for correlations of ice core records with radar traces [e.g. Gudmandsen, 1975, Hammer, 1980, Blindow, 1994b, Hempel *et al.*, 2000] or first attempts of numerical forward modelling [e.g. Moore, 1988, Blindow, 1994a, Hildebrand, 1996, Miners *et al.*, 1997], were restrained by the limited resolution and precision of the dielectric profiling data. In recent years, however, the improvement of dielectric profiling (DEP) [Wilhelms, 1996, 2000] enhanced the derivation of synthetic radargramms by numerical forward modelling approaches [Miners *et al.*, 2002, Eisen *et al.*, 2003b,c, 2004, 2006] and helped the method to become established at polar sites.

APPLICATIONS

Forward modelling has recently been applied on polar sites

- to investigate the causes of radar reflectors [Eisen *et al.*, 2003c,b, Miners *et al.*, 2002],
- to reduce dating uncertainties, when transferring ice core properties and datings onto internal reflecting horizons of adjacent radar profiles [Eisen *et al.*, 2006, 2004].

FORWARD MODELLING BY CONVOLUTION

Forward modelling is based on an ice core's reflectance profile R in the time domain, which can be calculated from DEP data in the depth domain by Equation (3.3) and has to be converted subsequently into two-way-traveltime by Equation (3.8). The convolution approach [Eisen *et al.*, 2003b] gains synthetic radargramms by simple one-sided convolution [cf. Bronstein, 2000, p. 750] of a synthetic wavelet w with the ice core's reflectance profile in the time domain.

$$(w * R)(t) = \int_0^t w(t-t')R(t')dt' \tag{3.12}$$

The approach requires a manageable amount of computing time but neglects wave phenomena like multiple reflections, interferences, etc. The more sophisticated numerical finite-difference time-domain (FDTD) model [Eisen *et al.*, 2003c] accounts for the later physical effects, too, but requires a substantial amount of computing time.

4 GROUND PENETRATING RADAR

The ground penetrating radar (GPR) surveys at Col du Dôme (CDD) and the subsequent processing of the radargramms have been conducted by Bohleber [2012, personal communication]. However, as the radargramms from GPR form the touchstone of this thesis's forward modelling approach, the outstanding analysis and discussion of the radargramms had to be conducted and are presented in the following.

4.1 DATA ACQUISITION

SETUP (cf. Section 3.2.1) GPR on CDD was conducted in common offset (CO) mode with separate shielded transmitter (TX) and receiver (RX) antennae mounted in static distance of 36cm on a sleigh using a RAMAC GPR of Malå Geoscience, Sweden, triggered by an odometer at 0.5m intervals and supplemented by separately collected GPS data [Preunkert et al., 2012, personal communication].

MEASUREMENTS Radargramms were recorded with frequency 250MHz along several flagged paths (cf. Figure 4.1). Every stored trace was stacked from 8 radar shots. For each shot reflections were recorded over time windows of 0.7μs to 0.9μs with about 2500 to 2800 samples per shot. However, the time windows for recording, needed to reach bedrock, were under-estimated.[8]

4.2 DATA PROCESSING

STANDARD PROCESSING Radargramms were processed [Bohleber, 2012, personal communication] with the software FOCUS by Paradigm Ltd. corresponding to a description in Bohleber [2011], following a standard procedure for seismic data processing in Yilmaz [2001], Navarro and Eisen [2009].

STATIC CORRECTION The time axes of the radar traces were shifted as to align the strong surface reflectors to zero time $t_{TWT} = 0$ns. The data from the surface wave above was cut.

FILTER A frequency-bandpass filter was used to cut high and particularly low frequent noise besides the GPR's operating frequency from the recorded traces.

GAIN To compensate the attenuation of amplitudes A due to spherical divergence a geometrical gain correction yielding $A_{corr}(t_{TWT}) \propto A(t_{TWT}) \cdot t_{TWT}^{n}$ was applied with best results for $n = 1.2$.

MIGRATION For identified allocation hyperbolae (cf. Section 3.2.1) a automated migration, i.e. a vertical shifting back into the plane of the IRH, was conducted.

CONVERSION OF TWO-WAY-TRAVELTIME TO DEPTH The conversion of depth to two-way traveltime (TWT) was conducted for the radar traces adjacent to the CDM core's borehole, i.e. the first shots of 121601, 121604 and 121609, as discrete implementation of Equation (3.8) (cf. Section 3.2.2). It was based on a wave-speed profile $c(z)$ derived from the core's dielectric profiling (DEP) data. An extrapolation along the radargramms was not tried as they mostly do not reach bedrock.

[8] Exact values for each radargramm can be found in Table A.1 in Appendix A.1.

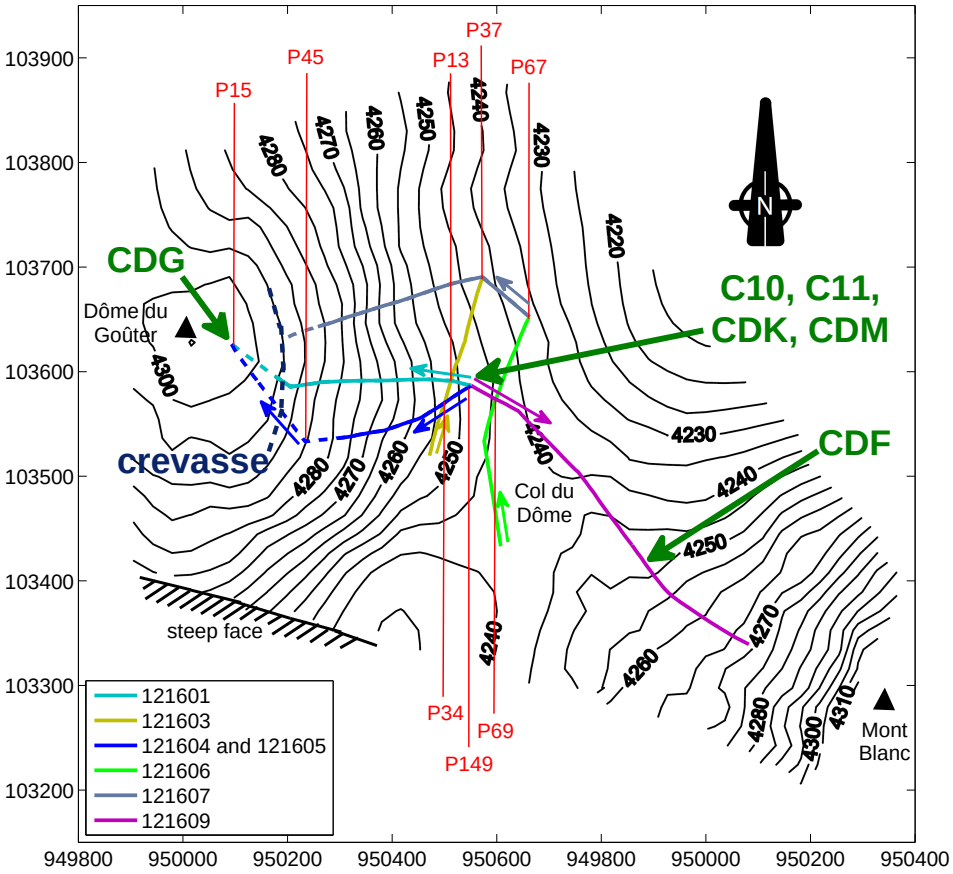

Figure 4.1: Map of the cold Alpine glacier Col dû Dome (CDD). Depicted are seven radar profiles 121601 to 121609 recorded with frequency 250MHz [Bohleber, 2012, unpublished], the locations of the ice cores CDM, CDK, CDG and CDF (dark green) and a crevasse westwards uphill the glacier (dark blue, dashed). Furthermore points of intersection are marked (red). Each profile is plotted in a different colour (cf. legend), its recording direction is marked by an arrow of the same colour. If in a section of a profile the internal reflecting horizons (IRH) H_2 (cf. Section 4.3.1) is traceable, the profile in this section is drawn continuously, else its drawn as a dotted line. Points of intersection are denoted by an 'P' plus the end-numbers of the crossing profiles in rising order, e.g. 'P69' for the intersection of profile 121606 and 121609. Intervals of 100 on the coordinate axes correspond to 100m in reality. The map in the background stems modified from Vincent *et al.* [2007a]

.

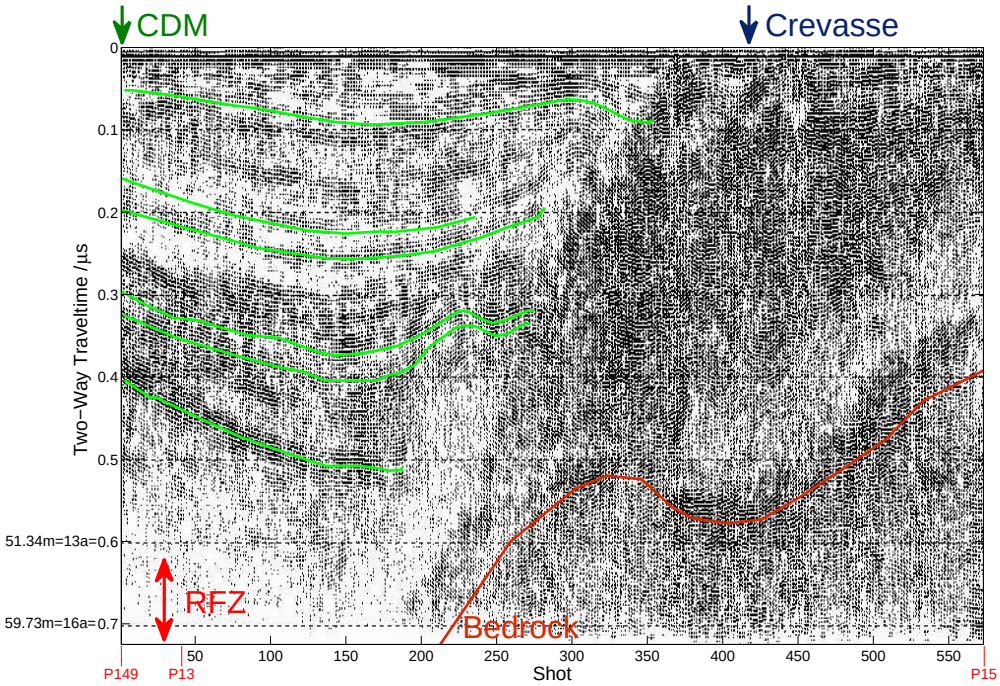

Figure 4.2: Radargramm 121601. The radargramm was recorded in direction of the x axis. Its course is mapped in Figure 4.1. Highlighted in the radargramm are in downwards order the picked internal reflecting horizons (IRH) H_1 to H_6 (light green), the reflector-free zone (RFZ)(red)and the assumed course of bedrock (brown). Marked at the top are the positions of the CDM core's borehole (dark green) and the crevasse (dark blue) and at the bottom the points of intersections with other radargramms (red). For selected two-way traveltimes (TWT) the corresponding local depths and ages before September 2012 at the position of the CDM core are added at the left.

4.3 Results and Discussion of the Ground Penetrating Radar Surveys

All the radargramms resulting from the above processing are displayed in Appendix A.3 (for a map cf. Figure 4.1). There further analysis has been conducted using the software ECHOS by Paradigm Ltd.

4.3.1 Analysis of the Radargramms

The radargramms bear several noteworthy features all exemplarily present in 121601 (cf. Figure 4.2). An overview is listed subsequently.

- Bedrock is visible as strong and broad reflector in parts of radargramm 121601, 121604, 121605 and 121609. It is not visible adjacent to the borehole CDM.
- The crevasse westwards uphill the CDM borehole is noticeable in radargramms 121601 and 121607.
- Below depths corresponding to TWT of 0.5μs to 0.7μs IRH are no longer distinguishable in the radargramms and reflections hardly occur anymore, a so-called reflector-free zone (RFZ) exists. This holds for all radargramms but 121605 were bedrock lies in relative small depths.

- IRH can are well traceable over the hole length of 121603, 121606 and 121609 but for the other profiles only in an area of 100 to 150 meters around the borehole (cf. Figures 4.2 and 4.1).

BEDROCK

Bedrock in radargramms is usually blurred over an uncertainty area of up to 60ns due to the allocation (cf. Section 3.2.1) of the strong bedrock reflectors[9]. In the present radargramms bedrock (where it was recorded) was picked from the broad band of its blurred reflector by increasing the threshold for the depicted amplitudes until only the maximum amplitudes remained. These were interpreted as bedrock.

INFLUENCE OF THE CREVASSE

When approaching the crevasse the IRH in the radargramm abruptly decline and get completely deranged and indefinable in the close vicinity of the crevasse. With greater depths they are disturbed in greater distances to the crevasse (e.g. cf. radargramm 121601 in Figure 4.2). This is caused by the allocation (cf. Section 3.2.1) of the strong reflectors from the ice-air transition at the walls of the crevasse. Assuming a vertical air gap running from surface to bedrock of the glacier, one would expect to see in the radargramm a hyperbolic diffraction area distributed symmetrical around the crevasse.

The observed effect corresponds to descriptions of the influence of crevasses in GPR radargramms from polar sites [e.g. given by Williams *et al.*, 2012, Lever *et al.*, 2013, Arcone and Delaney, 2000, Bogorodskiĭ *et al.*, 1985]. However, the declining of the IRH when approaching the crevasse deviates from the general descriptions of diffraction patterns in radargramms around crevasses. It suggests that the local net-accumulation at the position of the crevasse reaches a local maximum, i.e. that the crevasse is a local source for snow accumulation. This, too, is suggested, when comparing traced IRH from GPR radargramms to modelled isochrones from the application of the flow model SYNDICATE [Konrad, 2011, Konrad *et al.*, 2013] to profile 121601 (cf. Figure C.2, Appendix C). A plausible explanation therefor was, that the open crevasse acts as a sink for wind driven snow from wind erosion at the surface.[10]

REFLECTOR-FREE ZONE

The vanishing of distinguishable IRH in the radargramms from Col dû Dome (CDD) below depths corresponding to TWT of 0.5μs to 0.7μs (e.g. cf. radargramm 121601 in Figure 4.2) corresponds to the so-called reflector-free zone (RFZ) observed for Colle Gnifetti (CG) below the firn-ice transition [Eisen *et al.*, 2003a, Konrad *et al.*, 2013, Konrad, 2011, Bohleber, 2011](cf. Section 2.2.2). Yet the description reflector-free does not really fit for CDD as singular reflectors still occur but are not assignable to distinguished layers, i.e. IRH. The RFZ at CDD begins below the depth of the firn-ice transition as a comparison of radargramm 121601 (cf. Figure 4.2) to the density-depth profile of the CDM core (cf. Figure 6.2, Section 6.2) after conversion of two-way traveltime to depth establishes. After assigning ages to depths by using the age-depth profile of the CDK core[11] (cf. Figure 2.4, Section 2.2.1) the depth of the firn-ice transition was found to lie only in the later half of the 1990s.

This result suggests that one of the three currently discussed hypothetical contributions to the origin of the RFZ (cf. Section 2.2.2) can probably be ruled out, i.e. the supposed buffering impact of the regime tran-

[9] Bedrock reflectors are usually strong due to high dielectric contrast. [Bogorodskiĭ *et al.*, 1985, p. 217] gives for frozen bedrock dependent on its nature (soil, granite, etc.) values in the MHz-range for real relative dielectric permittivity between 1 and 10 and for dielectric conductivity of $10^{-1}\mu$S/cm to $10^{2}\mu$S/cm, while for glacier ice in the MHz-range values of permittivity typically lie around 3.18 and for conductivity in the order of $10^{-1}\mu$S/cm to 10μS/cm (cf. Table 3.1, Section 3.1.3).

[10] Personal experiences with the digging of snow pits on high elevated glaciers and their rapid subsequent burying by wind drift, may anybody make this explanation comprehensible.

[11] Till the going to press of this thesis no dating of the CDM core was available. So the age-depth profile of the CDK core drilled earlier at the same location had to be used.

sition of Alpine snow chemistry from slightly alkaline to acidic in the 1950s [Wagenbach *et al.*, 2012](cf. Figure 2.3, Section 2.2.1) on reflectors from conductivity variability below depths corresponding to the 1950s [Eisen *et al.*, 2003a].

TRACEABILITY OF THE INTERNAL REFLECTING HORIZONS

The picking and tracing of IRH throughout a study site allows the lateral extrapolation of ice core properties and can enable the direct comparison of data from different ice cores. For the radargramms from CDD picking and tracing of IRH is only possible in the firn region down to the depth of the RFZ. There an exemplarily bundle of horizons H_1 to H_6 has been picked and could be traced continuously throughout a large area (cf. Figure 4.2 and the Figures in Appendix A.2). The traceable area is represented in Figure 4.1. There the paths of the radargramms are plotted within the continuously traceable area as continuous lines and beyond the traceable area as dashed lines.

To evaluate the coherence of the IRH two closed circles were examined[12] (cf. Figure 4.1) following a procedure established by Bohleber [2011], Konrad [2011].

SMALL CIRCLE P13 → P34 → P149 → P13
(points of intersection: n_P =3, path length: ≈80m)

LARGE CIRCLE P37 → P34 → P149 → P69 → P67 → P37
(points of intersection: n_P =5, path length: ≈360m)

In both circles the TWT was entrained for each horizons H_1 to H_6 from point of intersection to point of intersection till the starting point was reached again, there resulting in offsets of several nanoseconds respectively horizons rising with depth and number of intersections (cf. Tables A.2 and A.3 in Appendix A.2). E.g. for the second horizon H_2 with TWT in the order of (160±20)ns the offsets amount to 15ns on the small course and 3ns on the large one. The resulting offsets correspond well with comparable ones found by Bohleber [2011, p. 155] on closed courses between boreholes on Colle Gnifetti (CG). Bohleber [2011] as well found IRH only in the firn region and traced them on closed circles down to TWT of 130ns to 440ns for the deepest horizon. He found after passing three points of intersection and after ≈750m offsets of 12ns and 37ns for the deepest horizons. Taking this as measure one can conclude that the traceability at CDD corresponds approximately with the one at CG.

4.3.2 UNCERTAINTIES

UNCERTAINTIES OF IRH

Systematic uncertainties and errors of the reflectors and IRH in radargramms arise from

LIMITED RESOLUTION The limits of resolution corresponding to the summarized specifications by Navarro and Eisen [2009] (cf. Section 3.2.1) cause uncertainties in depth respectively in TWT for every feature depicted in the radargramms. Assuming a real radar wavelet of 5 half cycles of frequency $f = 250$MHz, than follows for the present radargramms a vertical uncertainty of $\Delta t_{TWT}^{vert.} \approx 4$ns and a horizontal uncertainty of $\Delta t_{TWT}^{hor.} \approx 4$ns.

ALLOCATION The uncertainty from allocation (cf. Section 3.2.1) is growing with depth but cannot be quantified further.

[12] Each of them starts at a point of intersection between two or more radargramms, denoted e.g. as P13 for the intersection of 121601 and 121603, runs along parts of several radargramms and switches at several point of intersection until it ends in the starting point.

UNCERTAINTIES IN PICKING IRH

When picking and tracing IRH uncertainties arise from the

- resolution of the GPR,
- risk of picking the false phase thus changing to a higher or lower horizon.

The uncertainty from limited resolution has been discussed in the preceding subsection and is taken over as $\Delta t_{TWT}^{(1)} = 4\text{ns}$. The uncertainty from the risk of picking the false phase within a radargramm $\Delta t_{TWT}^{(2)}$ can only be estimated, the uncertainty from the risk of picking the false phase at a point of intersection when switching from one radargramm to the other $\Delta t_{TWT}^{(3)}$ however can be quantified. It corresponds to the average distance between two horizons in a certain depth at the point of intersection and can for the present case be estimated as ca. $\Delta t_{TWT}^{(3)} = 4\text{ns}$. For the total uncertainty of an IRH in TWT $\Delta t_{TWT}(n_P)$ after n_P profile switches at points of intersection follows with Gaussian error propagation:

$$\Delta t_{TWT}(n_P) = \sqrt{\left(\Delta t_{TWT}^{(1)}\right)^2 + \left(\Delta t_{TWT}^{(2)}\right)^2 + n_P \cdot \left(\Delta t_{TWT}^{(3)}\right)^2} \overset{\text{here}}{=} \sqrt{(n_P+1)\cdot(0.4\text{ns})^2 + \left(\Delta t_{TWT}^{(2)}\right)^2}$$

Comparing expected uncertainties calculated with the above Equation for $\Delta t_{TWT}^{(2)} = 0$ with the unto 5 times larger real offsets appearing in the closed circles (cf. Tables A.2 and A.3) it becomes obvious that the contribution from the risk of picking the false phase within a radargramm $\Delta t_{TWT}^{(2)}$ must be large.

5 DIELECTRIC PROFILING

5.1 DATA ACQUISITION

Dielectric Profiling (DEP) on the CDM ice core from Col du Dôme was conducted in November 2012 by Bohleber and Hackel.

5.1.1 SETUP

The dielectric profiling (DEP) of the CDM ice core was conducted using

- four of five frames of a 3-inch DEP measuring bench of *Alfred-Wegener Institute for Polar and Maritime Research (AWI)*, Bremerhaven, designed by Wilhelms [1996, 2000],
- controlled by a HP 4285A Precision LCR Meter with measurement range from 75 kHz to 30 MHz,
- a PI Physik Instrumente C-500 Stepping Motor Controller and
- a new LabView controlling software α-release of Frenzel [unpublished] on a common PC.

The setup is displayed in Figure 3.5, Section 3.2.3.

5.1.2 MEASUREMENTS

Measurements of the 159 core pieces were carried out in 109 runs at frequencies of 250 kHz, 500 kHz and 1 MHz at constantly -11°C. Furthermore 7 runs of empty measurements were conducted, one at every beginning, half and end of each measurement day. The data was supplemented with visually cognoscible defects and stratigraphic properties (cf. Table 5.4) registered against depth and digitalized in a separate logging file. Overall 17% of the ice core were logged as defective.

Empty measurements with the ice-core-free bench were done to record possible shifts of the measured values due to changes of the experimental setup. They determined the so-called empty capacitance C_0 and empty conductance G_0 for each step along the bench, for which in theory unanimously should hold $C_0 = 0.0622$pF and $G_0 = 0$S [Wilhelms, 1996]. In practice however measured empty values depend sensitively on the real setup and its environment, for example on the self-capacitances of cable guiding or on temperature dependencies of the capacitances and conductances of the setup's components, to name the two major variables whilst the measuring.

The logging file was established, first to be used for the necessary correction of defective ice core parts whilst the further processing of the DEP data and secondly to possibly support the interpretation of results.

5.1.3 PROBLEMS DURING MEASUREMENTS

FAILED OPEN CALIBRATION Prior to the measurements a so-called open calibration of the LCR-Meter, i.e. a field-free measurement with a plane metal sheet between high and low electrode on the potential of low, should have taken place to eliminate offsets on the measured data resulting from other

capacitors joined up in the circuit than the bench's cylindrical one. The calibration was aborted by the LCR Meter for each attempt and indeed could not have been accomplished with the given LCR meter as confirmed by Wilhelms in a later telephone communication. Consequently the raw data for capacitance and conductance was afflicted with an offset and was located in the negative range with capacitances $C < -0.01$ pF and conductances $G < -0.01$ μS. This had to be corrected subsequently whilst data processing. (cf. Section 5.2.3)

DEFECTIVE SOFTWARE The LabView software, which controlled the setup, read the measured data and wrote it into files, seemed to perform without serious shortcomings until a data review at the end of the first measuring day revealed a major error. Even though the software displayed the measured data internally correctly, it did not write it correspondingly into files, but inscribed only three decimal places per value, i.e. for values in the pF and μS range '0.000'. However it was possible to work around the software's saving routine by extracting the data out of the software's block diagram in the LabView development environment. Thus the re-measurement of the first day's core pieces 1 till 63 was possible.

Yet another problem had arisen as those pieces had already been cut into archive pieces and 2.6 cm high lamellae[13] (cf. Figure 5.1), so re-measurements could only be conducted with the archive pieces instead. Thus capacitances C_A^* and conductances G_A^* of effectively a series connection of the archive pieces and an 2.6 cm wide air gap from the missing lamellae had to be measured. As the real relative dielectric permittivity respectively the electric conductivity of air ($\varepsilon_A \approx 1, \sigma_A \approx 0$) lie below the corresponding values of ice (cf. Table 3.1), the measurements of C_A^* and G_A^* are lying lower than the corresponding C and G of intact cores. This is plainly observable in the raw data of the collectively measured core pieces 134 and 135 displayed in Figure 5.5, of which 134 due to its large diameter had to be measured as archive piece whilst 135 could be measured as intact core. For the subsequently necessary correction of the so gathered data (cf. Section 5.2.1) comparative measurements of complete and intact core pieces and there corresponding archive pieces after cutting were conducted , i.e. for 64/65, 72, 80/81 and 88/89.

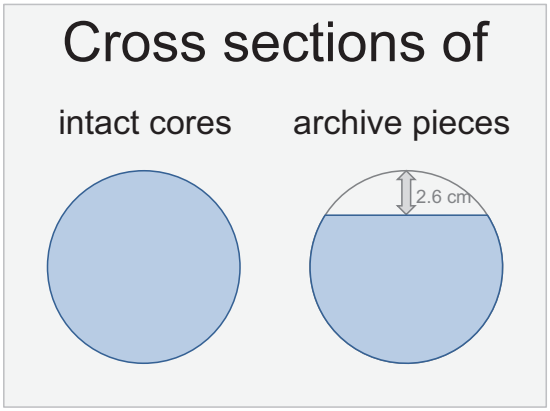

Figure 5.1: Cross sections of intact cores and archive pieces

5.2 DATA PROCESSING

The processing of the DEP data comprised several stages involving corrections and calculations until it resulted in depth profiles of permittivity and conductivity. The separate stages are outlined in Figure 5.2 and discussed at length subsequently. Most of them were standard procedures generally applied in DEP data processing [Wilhelms, 2013, personal communication] whilst others had to be developed specially for the correction of the systematic errors that occurred whilst data acquisition. They all had to be implemented individually for this processing job using MATLAB by MathWorks Inc., as no documentation on the processing and no automated solutions were available.

[13] The lamellae were cut for ion-chromatographic studies

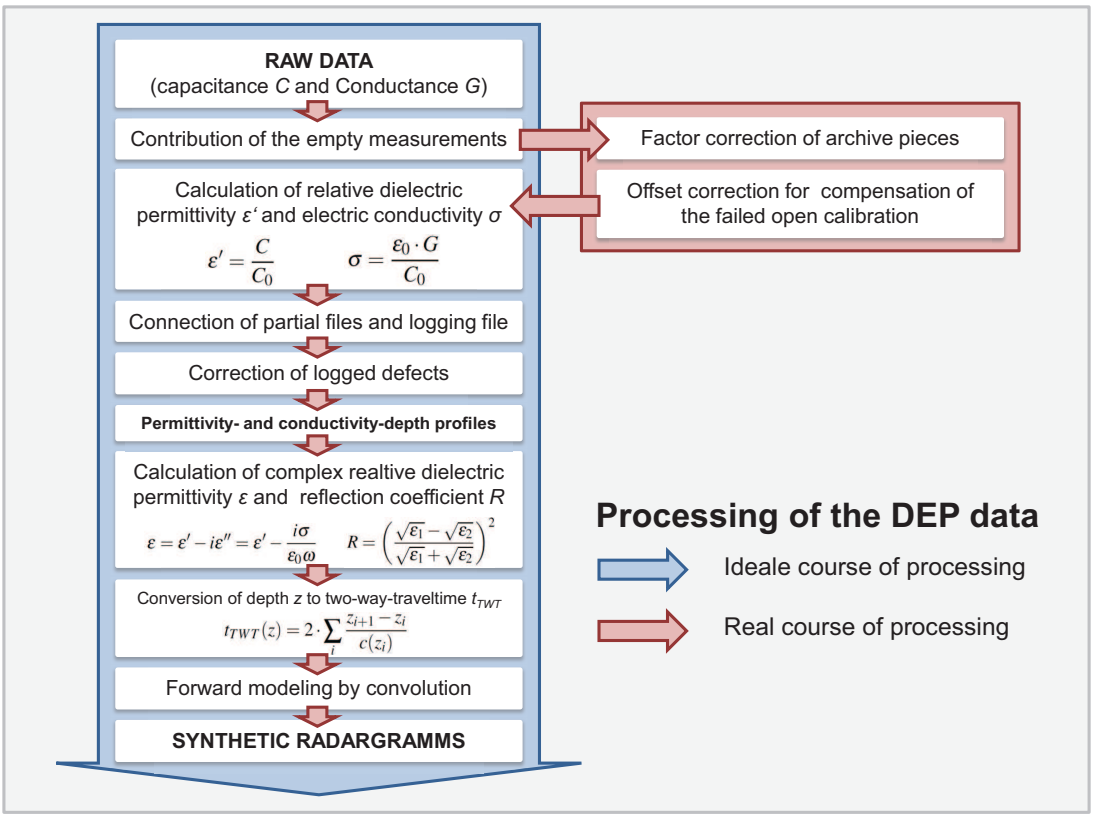

Figure 5.2: Processing of the DEP data and forward modelling by convolution displaying the several stages between the input, the DEP raw data consisting of capacitance and conductance data, the output of the DEP processing, the permittivity- and conductivity-depth profiles, and finally the output of the forward modelling, the synthetic radargramms. Inevitable in processing and more or less standard are the blue shaded stages in the left column. The red shaded processing steps in the right column, had to be developed to deal specially with the problems that occurred whilst the data acquisition.

5.2.1 Correction of Archive Pieces

As already discussed in Section 5.1.3, the values of capacitance C_A^* and conductance G_A^* of the core pieces, that were effectively measured as archive pieces in series connections with 2.6 cm wide air gaps from the missing lamellae, lay to low and had to be corrected. A formal approach for the necessary correction was derived from the theory of the series connection of capacitors and can be found at length in Section B.1 of the appendix. It yields the non-linear relations (B.9) and (B.10) between the effectively measured values C_A^* and G_A^* and the wanted values for intact core pieces C and G:

$$C = \frac{k}{\frac{1}{C_A^*} - l}, \tag{5.1}$$

$$G = \frac{m}{\frac{1}{G_A^*} - n}, \tag{5.2}$$

with $k, l, m, n = const$.

The non-linearity of the relations is a consequence of the depth dependency of the ice cores dielectric properties and the consequential depth dependency of the archive pieces' capacitances C_A and conductances G_A whilst the properties of the air gap remain unchanged throughout depth.

To determine the set of constants k, l, m and n several approaches were possible and tried:

1ST APPROACH: An empirical approach on basis of the comparative measurements of the intact core pieces and archive pieces 64/65, 72, 80/81 and 88/89,

2ND APPROACH: A simplified reduction of this approach only gaining k and m by neglecting the contributions of the air gaps and

3RD APPROACH: An inverse normative determination of the the set of constants using literature values of the real relative dielectric permittivities and electric conductivities of snow and ice plus the demand for steady curves of the measured parameters' trends at the transition between the core pieces measured as archive pieces and measured as intact core pieces.

1ST APPROACH This approach was based on the re-formulation of (5.1) and (5.2) into the line equations $\frac{C}{C_{A*}} = k + l \cdot C$ and $\frac{G}{G_{A*}} = m + n \cdot G$, these recommending, that l respectively n could be gained as slopes and k respectively m as intercepts with the ordinate, if the data of the comparative measurements for the capacitance was plotted $\frac{C}{C_{A*}}$ versus C and respectively corresponding for the conductance. This was conducted on the the trends of the respective data sets, won by eigenvalue decomposition, to avoid that high frequent noise interferes with the expected linear relation. The resulting graphs are displayed exemplarily in Figure 5.3 and completely in Figure B.1 in Appendix B.2, the extracted values of k, l, m and n in Table 5.1. Apparently the expected linear relations can not be established on the current data, there are neither unambiguous slopes nor unambiguous ordinate intercepts. This presumably is caused by the factor that the data basis of the four comparative measurements has been collected bellow the firn-ice transition where the trends of the dielectric properties of the core are no longer subject to major changes and the non-linear relations are replaced by linear once. Lacking comparative data from the firn region of the core thus this approach was dismissed.

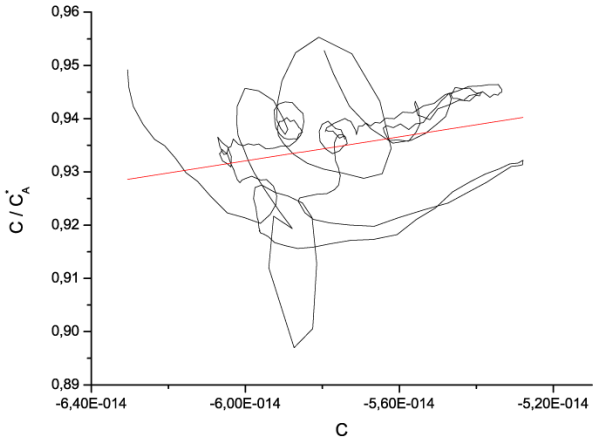

Figure 5.3: 1st Approach of archive piece correction Depicted is exemplarily for core piece 64/65 the resulting graph (black) from plotting $\frac{C}{C_{A*}}$ versus C and a linear fit (red) to it. The expected linear relation can not be established, there is neither an unambiguous slope l nor an unambiguous ordinate intercept k.

2ND APPROACH Still trying to gather a correction out of the comparative measurements the second approach neglected the non-linearity caused by the air gap and assumed that $C_A^* \approx C_A$ respectively $G_A^* \approx G_A$ holds. Than follows corresponding to the formulas (B.13) and (B.14) from Appendix B.1:

$$\frac{C}{C_A^*} \approx \frac{C}{C_A} = k = const.$$

$$\frac{G}{G_A^*} \approx \frac{G}{G_A} = m = const.$$

This reduced the problem to the determination of constant correction factors *k* and *m*, which can inartificially be solved by division of the comparative measurements' data of the intact cores through the appendant one of the archive pieces. Therefor the data was averaged for each of the four segments 64/65, 72, 80/81 and 88/89 after cutting the defective data at the ends and beginnings of single core pieces. Finally the correction factors were gained as the average of the particular four. The results are displayed in Table 5.1. The quality of this approach was tested primarily on basis of the four comparative measurements by comparison of the data of the intact core pieces with the factor corrected data of the archive pieces (cf. Figure 5.4 and Figure B.2 in Appendix B.2). The corrected archive pieces' data corresponds well within one standard derivation with the data of the intact cores. A more qualitative secondary validation was given by the observation, that the uncontinuous steps between the core intervals measured as archive pieces and those measured as intact core pieces were reduced to insignificance by the applied correction (cf. Figure 5.5 and Figure B.3 in Appendix B.2). This was important as artificial discontinuities in the signal subsequently would have led to strong reflectors and artefacts in the synthetic radargramm. The major shortcoming of this approach is, that the negligence of the non-linearity led to a too high trend of the corrected data in lower depths and a too gentle incline of the depth profiles (cf. Section 5.3.3 and Figure 5.8). However, as the macroscopic trend of the data is not essential for the structure of the synthetic radargramms and only inflicts an error in the conversion between depth and traveltime, the results of the factor correction gained by this approach could be used for the further processing.

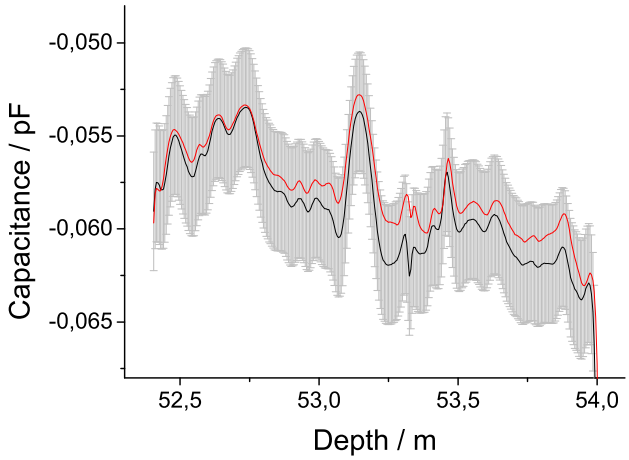

Figure 5.4: 2nd Approach of archive piece correction. Depicted is exemplarily for core piece 64/65 the comparison of the capacitance of the factor-corrected archive piece (black) with the capacitance of the appendant intact core piece (red). Both correspond well within one standard deviation (grey shaded uncertainty range).

3RD APPROACH The final third approach was implemented retroactively after assessing the permittivity-depth profiles in Section 5.3.3, when it became plain that the thitherto applied corrections led to curves too high and to gentle in slope (cf. Figure 5.8). Then the idea evolved to scale the data in order that it fitted with literature values for the boundaries of snow at the top and glacier ice at the bottom. This was conducted by a backwards calculation (cf. Appendix B.1) of the parameters *k*, *l*, *m* and *n* and subsequently the application of the formulae (5.1) and (5.2). Therefor literature values from Bohleber *et al.* [2012] and Jepsen [2010] were used (cf. Table 5.2). The results are listed in Table 5.1. The resulting depth profiles of conductance and capacitance are displayed in Figure 5.8 and met with some fine tuning on the set of parameters the requirement that no large discontinuities should remain at the transitions between core intervals measured as archive pieces and such measured as intact cores. The approach led to the demanded trends of the dielectric properties, but caused a large surge of the relative amplitude of the signals variability in the core's interval measured as archive pieces. The amplitudes abruptly diminish at the transition between the two measurement regimes – obviously an artefact of the approach. In the later

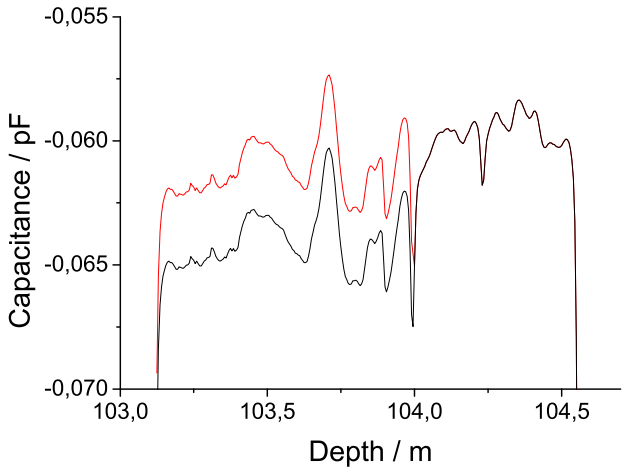

Figure 5.5: 2nd Approach of archive piece correction. Depicted is the capacitance of the core pieces 134/135 before (black) and after factor-correction (red) Both pieces were measured in one run with 134 due to a too large diameter measured as archive piece and 135 as intact core piece. The discontinuity at the transition between the core pieces after correction is reduced to insignificance compared to the natural variability of the data.

forward modelling (cf. Chapter 6) this behaviour led to relative large reflection coefficients in the upper part of the core measured as archive pieces in contrast to relative weak ones in the lower part. In combination with the attenuation of the reflected radar amplitudes with depth this led to an artefact reduction of the reflectors relative amplitudes below core piece 63. The approach therefore was not used for further processing.

Table 5.1: Resulting set of parameters k, l, m and n for the archive piece correction retrieved from three different approaches.

	k	**l** $(\cdot 10^{12})$	**m**	**n** $(\cdot 10^{6})$
1st approach				
Core Pieces 64/65	1.000 ± 0.011	1.132 ± 0.203	0.780 ± 0.014	5.482 ± 1.130
Core Piece 72	1.330 ± 0.044	6.358 ± 0.745	0.809 ± 0.025	6.811 ± 2.017
Core Pieces 80/81	1.114 ± 0.011	2.599 ± 0.192	1.023 ± 0.003	-4.820 ± 0.275
Core Pieces 88/89	0.241 ± 0.035	-1.239 ± 0.607	0.773 ± 0.005	17.0560 ± 4.682
2nd approach	0.954 ± 0.016	—	0.859 ± 0.028	—
3rd approach	0.236	-0.134	0.397	45.791

RÉSUMÉ ON THE THREE APPROACHES Weighing the pros and cons the actual archive piece correction was implemented as factor correction corresponding to the second approach. Thereby a linear operation was applied, which did not cause unaccounted artefacts. However the shortcoming of the resulting data that it overrated the data in the upper core segment had to be kept in mind for the conversion of depth to two-way traveltime in Section 6.1.

5.2.2 TREATMENT OF EMPTY MEASUREMENTS: CALCULATION OF A MEAN EMPTY SIGNAL

The empty measurements were needed for the calculation of the dielectric values of the real relative permittivity ε' and the electric conductivity σ corresponding to Equations (3.9) and (3.10), furthermore they could be used for the correction of the failed open calibration.

As can be seen in Figure 5.6 the seven empty measurements corresponded very well with each other and could be represented by their average, thereby avoiding that minor deviations between the different empty

signals lead to artefact discontinuities at the transitions between core intervals with different assigned empty signals.

Furthermore the separate empty measurements possessed a characteristic course and did not display a constant capacitance for the different positions of the measuring low electrode along the empty capacitor's axis. Reason therefor was the inevitable movement of the cable guidance whilst measuring and consequent modulation of the cables self-capacitance. It was not ex ante obvious how they had to be considered for the forthcoming calculations.Anticipating later results (cf. Section) it became evident that they had to be considered by their mean values as otherwise artefact periodicities would have emerged as one can see in Figure 5.7.

5.2.3 Offset Correction for the Replacement of the failed Open Calibration

As outlined before in Section 5.1.3 the failure of the open calibration of the setup caused an offset on the data. This had to be determined from literature data and subtracted from the measured capacitance and conductance before the calculations of the real relative permittivity and the electric conductivity could be implemented. Two approaches using different literature data were possible.

1st Approach using theoretical values for the empty capacitor of the DEP bench

2nd Approach using literature values of the dielectric properties of glacier ice

1st Approach Initially the offset was determined as difference between the mean values of the average empty signals measured from theoretical values for the setup's empty capacitance C_0^{lit} and empty conductance G_0^{lit} by Wilhelms [1996] (cf. Table 5.2). The corresponding calculations can be found in Appendix B.2, the resulting offsets are listed in Table 5.3. If one assumed that the offset corrected relative dielectric permittivity and electric conductivity of the CDM ice core in the ice region should correspond well with known literature values (cf. Tables 5.2 or the more comprehensive Table 3.1) of these dimensions, the results of this approach deviated significantly from the expectation, e.g. for the permittivity in the basal region the expected value of ca. 3.19 is surpassed by 0.7-0.8 (cf. Figure 5.8).

2nd Approach Due to the deviation of the first approach's results from the expectation, a second approach on basis of literature values of the relative dielectric permittivity and electric conductivity of glacier ice was strained. Now the offsets were determined by backwards calculation, so that the subsequent calculation of the dielectric properties lead to their asymptotic convergence with depth against the initial literature values. Literature values for the dielectric properties of glacier ice have been supplied over the last decades by several studies [e.g. by Bohleber *et al.*, 2012, Fujita *et al.*, 2000, Wolff, 1995, Matsuoka *et al.*, 1996, Johari and Charette, 1975, Johari, 1976] (cf. Table 3.1). The here used values are listed in Table 5.2, the calculations may be found in Appendix B.2 and the resulting offsets are listed in Table 5.3. This approach seemed to lead to the best results and furthermore corresponded to the well established method usually applied by Wilhelms [2013,personal communication].

Résumé on the two Approaches The offset correction was conducted on basis of the second approach, thereby again implementing a linear operation, which did not cause unaccounted artefacts. The resulting data thus converged asymptotically with depth against the expectated values of glacier ice.

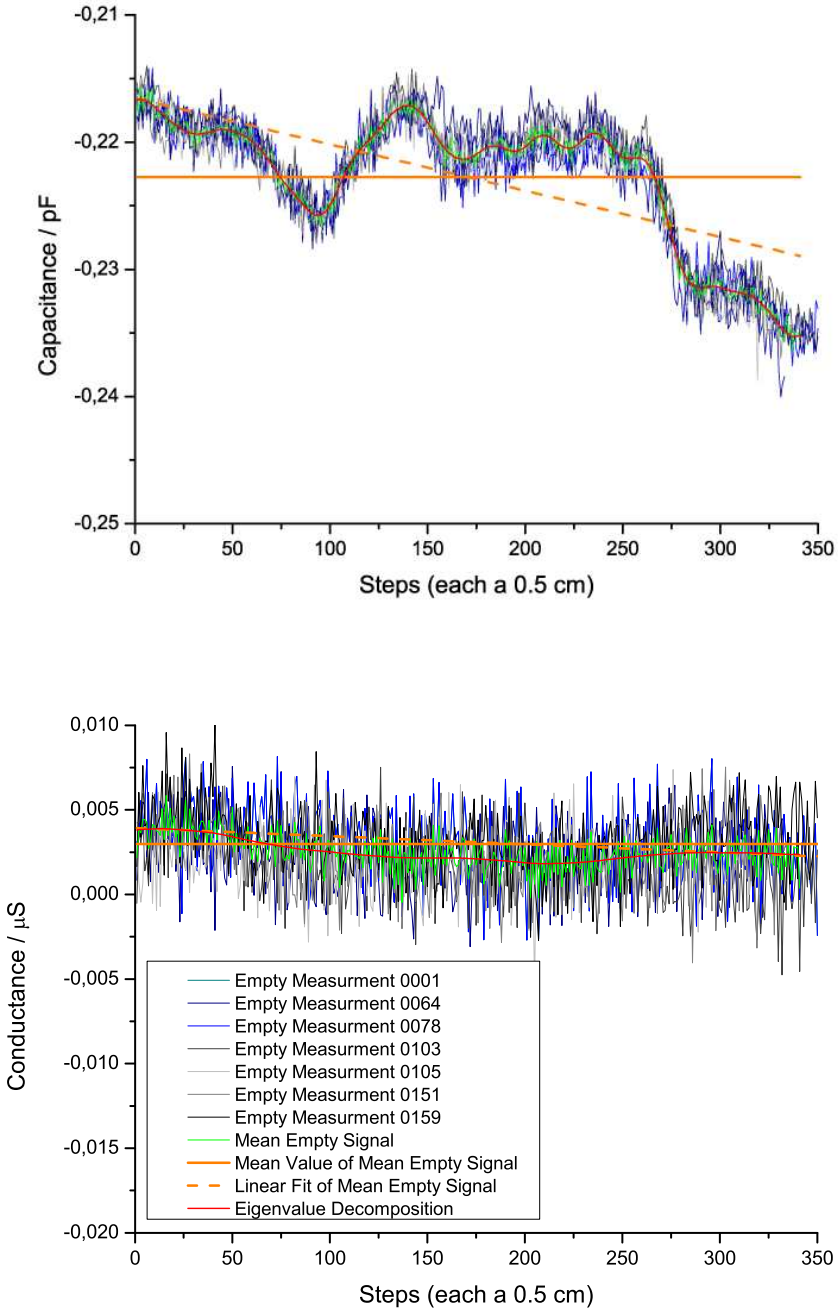

Figure 5.6: Empty measurements: The figures display the seven separate empty measurements of capacitance and conductance collected at the beginning, half and end of each measuring day (shades of blue and grey), their average (green) and thereof an eigenvalue decomposition (coloured in red), a linear fit (orange dotted) and the mean value (orange). Apparently the empty signal does not shift and the separate empty measurements correspond all very well with each other and can be represented by their average. Furthermore it is plain that the seven empty measurements posses characteristic courses and do not display constant values along the length of the empty capacitor. Reason therefor is the inevitable movement of the cable guidance whilst measuring and the consequent modulation of the cables self-capacitance.

Table 5.2: Theoretical values for the empty capacitor of the DEP bench and the dielectric properties of glacier ice applied in the two approaches for the offset correction for the replacement of the failed open calibration. The applied values for dielectric properties ofglacier ice were selected from the various literature values in Table 3.1.

1ST APPROACH:		
Theoretical values for the empty capacitor of the DEP bench:		
Empty capacitance:	$C_0^{lit} = 0.0622$pF	[Wilhelms, 1996]
Empty conductance:	$G_0^{lit} = 0$nS	[Wilhelms, 1996]

2ND APPROACH:		
Literature values for the dielectric properties of glacier ice: (Selection from Table 3.1)		
High-frequent real relative dielectric permittivity:	$\varepsilon_\infty'^{\text{ice}} = 3.18$	[Bohleber *et al.*, 2012]
High-frequent electric conductivity:	$\sigma_\infty^{\text{ice}} = 0.05\mu$S/cm	[Jepsen, 2010]

Table 5.3: Derived offsets from the two different approaches for the offset correction for the replacement of the failed calibration

	ΔC	ΔG
1ST APPROACH	$0.2849pF$	$-2.7873\mu S$
2ND APPROACH	$0.2983pF$	$-2.0368\mu S$

5.2.4 CALCULATION OF RELATIVE DIELECTRIC PERMITTIVITY AND ELECTRIC CONDUCTIVITY

The calculation of the depth profiles of the real relative dielectric permittivity $\varepsilon'(z)$ and the electric conductivity $\sigma(z)$ out of the measured data was based on the relations 3.9 and 3.10 (cf. Section 3.2.3):

$$\varepsilon' = \frac{C}{C_0},$$
$$\sigma = \frac{\varepsilon_0 \cdot G}{C_0},$$

with vacuum permittivity $\varepsilon_0 = 8.854187817 \cdot 10^{-12}\text{AsV}^{-1}\text{m}^{-1}$ [Gerthsen and Meschede, 2010]

Obviously for each depth z the appendant capacitance $C = C(z)$ and conductance $G = G(z)$ had to be applied in this computations. Correspondingly one had to expect that the same held for the empty measurements capacitance C_0 since the modulation of the cable's self-capacitance whilst the measuring had to be expected to have a similar effect in the actual measurements of the core pieces as it had had in the empty measurements. This and several other approaches for the empty signals possible contribution to the calculations were tested and are listed below.

1ST APPROACH: $C_0 = C_0(z) \equiv$ exact course of the average empty signal

2ND APPROACH: $C_0 = C_0^{\text{trend}}(z) \equiv$ eigenvalue decomposition of the average empty signal

3RD APPROACH: $C_0 = C_0^{\text{linear trend}}(z) \equiv$ linear trend of the average empty signal

4TH APPROACH: $C_0 = \int dz' C_0(z') / \int dz' \equiv$ mean value of the average empty signal

The results of the four approaches are plotted in Figure 5.7. The first three apparently led to periodic artefacts. The first one furthermore induced strong noise on the resulting data of ε' and σ as here the high-frequent noise of the empty signal entered into the calculations. Evidently the only approach, which supplied steady and artefact-free results acceptable for further use, was the fourth one.

Input data for the calculations (3.9) and (3.10): capacitance $C(z)$ and conductance $G(z)$

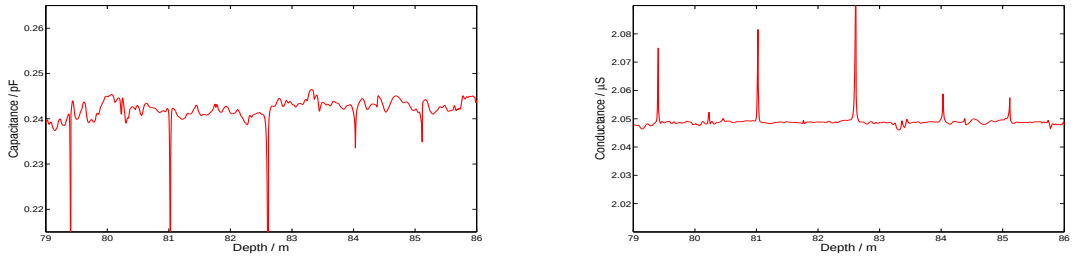

1ST APPROACH: Results from calculations with $C_0 = C_0(z) \equiv$ exact course

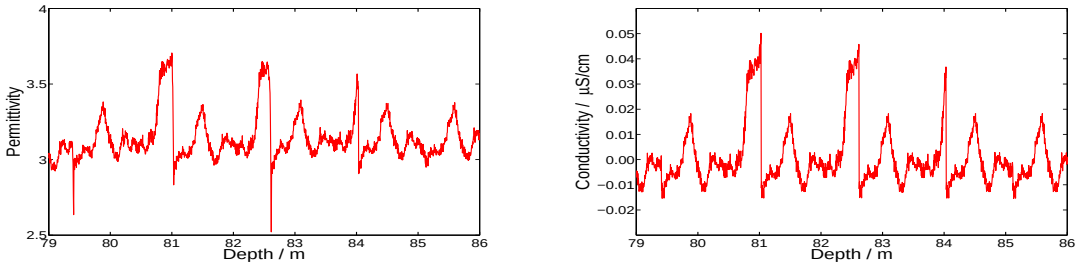

2ND APPROACH: Results from calculations with $C_0 = C_0^{\text{trend}}(z) \equiv$ eigenvalue decomposition

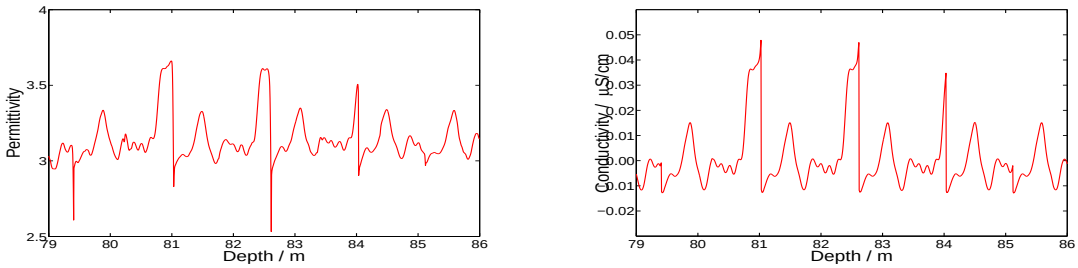

3RD APPROACH: Results from calculations with $C_0 = C_0^{\text{linear trend}}(z) \equiv$ linear trend

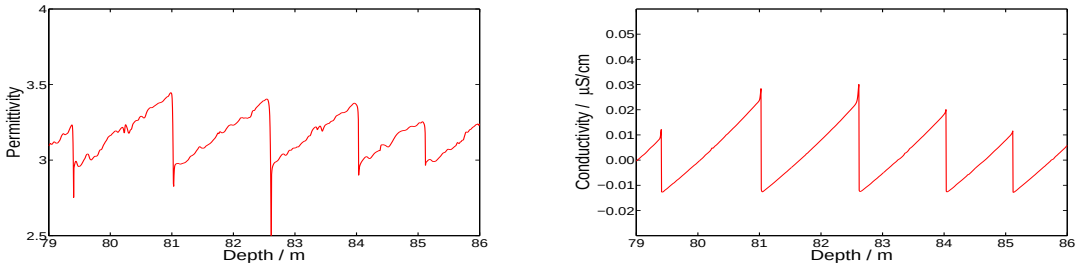

4TH APPROACH: Results from calculations with $C_0 = \int dz' C_0(z') / \int dz' \equiv$ mean value

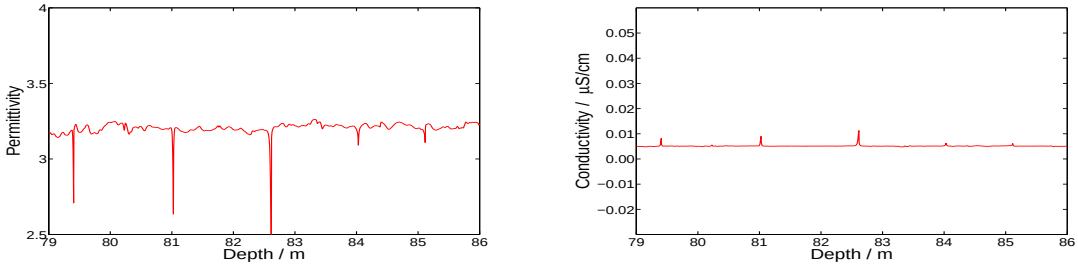

Figure 5.7: Results of four different approaches to include the empty measurements of C_0 into the calculation of the real relative permittivity ε' and the electric conductivity σ: The first three approaches apparently lead to periodic artefacts. The first one furthermore induces strong noise on the resulting data of ε' and σ as here the high-frequent noise of the empty signal enters into the calculations. The only approach, which supplies steady and artefact-free results acceptable for further use, is the fourth one.

Table 5.4: Logged defects and stratigraphic properties of the CDM ice core with appendant acronyms

Defects			Stratigraphy		
BR	≡	Breaks	IL	≡	Separate ice layers
DF	≡	Breaks with missing volume	ILS	≡	Series of ice layers
FR	≡	Fractured ice core volume	ILense	≡	Ice lenses
SL	≡	Slices	CL	≡	Large clear ice layers
DF(SL)	≡	Missing slices	DL	≡	Brownish dust layers
DF(CC)	≡	Defects from core catchers	DarkL	≡	Otherwise dark ice layers
DF(miss)	≡	Missing ice core intervals	Silt	≡	Silt

5.2.5 Connection of Partial Files and Logging File

The single data files of the separate measurements and the logging file were know concatenated to one data file containing both data and logging information of the complete ice core. Overlaps of the logged depth of the adjacent measurements' data files were cut always from the end of the files.

5.2.6 Correction of logged Defects

A specially critical stage of the data processing consisted in the correction of the data of defective or missing ice core volume, because for such the permittivity and conductivity may collapse abruptly creating artefact gradients (cf. Figure 5.9) and thus in the later forward modelling artefact reflectors. A variety of such defects was observed and logged whilst DEP (cf. Table 5.4).

Due to the individuality of the different defects and the high inaccuracy of about 1-2 cm of their logged depths a semi-automatic correction routine was implemented that allowed to decide for every logged defect to correct or not to correct and accordingly the manual definition of borders for cutting and correction. The corrections between these borders were conducted by linear interpolation and logged in separate columns of the data file. Other more sophisticated interpolation modi were dismissed as they led to momentous minima or maxima and unjustifiable oscillating curves. Input and results of these corrections are illustrated in Figure 5.9. The high and sharp peaks of the input data originate from the breaks between the separate ice core pieces.

In summa 17% of the ice core volume was defective, corrections had to be conducted on 24%!

5.2.7 Summarized Effects of the Corrections and Calculations of the Processing

Both the factor correction of the archive pieces and the globally applied offset correction were finally implemented as linear operations on the raw data, i.e. as the 2nd approach for the archive piece correction (AC2) and the 2nd approach for the offset correction (OC2). The factor correction (AC2) particularly ascertaining, that no discontinuities between the core segments measured as archive pieces and those measured as intact core pieces should remain. Furthermore the calculations of permittivity and conductivity were implemented as linear operations as the empty measurements only entered as scalar values into them. In so far artefacts on small scales, such as possible periodical artefacts from the contribution of the empty measurements, can be excluded. However on the global scale the implemented archive piece correction (AC2) neglects the non-linearity caused by the air gap and probably leads to artificially high permittivities respectively low conductivities in lower depths. As can be seen in Figure 5.8 this is also suggested by the course of another profile calculated from density data [Preunkert et al., 2012,

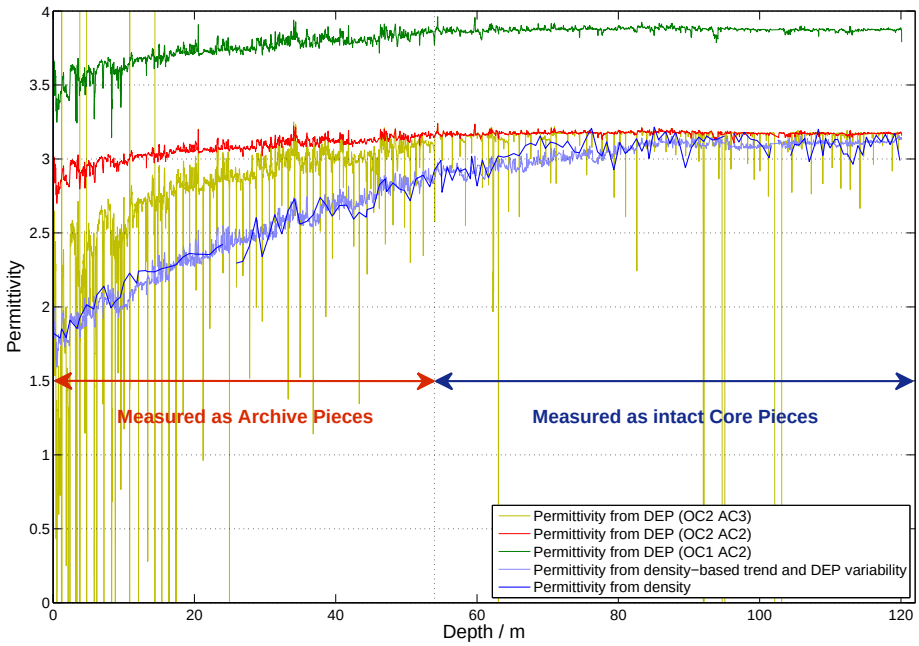

Figure 5.8: Comparison of permittivity-depth profiles from DEP corresponding to different approaches for correction and a density-based profile calculated by Kovacs's formula: The profiles from DEP result from the linear 2nd (AC2) and non-linear 3rd approach (AC3) for the archive piece correction and the 1st (OC1) and 2nd approach (OC2) for the offset correction. Note that on (AC3) no defect corrections have been conducted as the approach was dismissed, hence the data still displays the large sharp peaks from the interceptions of the different measurement runs. The density-based profile (blue) is calculated with Looyenga's Formula (Equation (3.5), Section 3.1.3), the further profile (light-blue) is a hybrid with density trend and DEP variability. For the further analysis and forward modelling profile (OC2 AC2) is used as it contains the exact variability of the DEP data. For the conversion of depth to two-way traveltime the hybrid profile from densitybased trend and DEP variability (light blue) is used as it contains the correct trend. Bedrock lies at 121m.

personal communication] using Looyenga's Model (cf. Equation (3.5), Section 3.1.3). The also depicted but dismissed profile resulting from the 3rd approach for the archive piece correction (OC2 AC3), which considered the non-linearity but induced artificial noise, suggests a true course somewhere between the DEP based profile (OC2 AC2) and the density based profile. The true course of the trend in fact should lie within an relative uncertainty range of 3.5% around the density-based profile [Wilhelms, 2000]. Additionally the implemented offset correction could only shift the data sets into the right region of some expectancy values of the ice's dielectric properties at the frequency 250 kHz determined rather arbitrarily by frequency scaling.[14]

Thus the two data sets certainly are not able to give an exact measure of the ice core's true dielectric properties at the frequency 250 kHz. But for the interest of this thesis the results should be sufficient, as the further forward modelling predominantly depends on the variability of the permittivity and conductivity profiles whilst possible deviations of the trend only cause minor errors in the conversion of depth to two-way traveltime. The further analysis of the permittivity and conductivity profiles as outlined above also depends mainly on the variability of the signal. Yet the poor quality of the ice core, comprising 17%

[14]The problem of the frequency scaling will be discussed later on in Chapter 6.

of defective ice core volume that had to be corrected in the final processing stage again involving 24% of the core, presented a significant challenge for the interest of this thesis, as every missing interval of information about the variability of the data hampered the further forward modelling.

For the conversion of depth to two-way traveltime a further profile is created by adding the detrended (cf. Appendix D.1) permittivity variability to the trend of the density-based profile (cf. Figure 5.8). The resulting profile should reduce errors in depth-to-two-way-traveltime conversion but does not qualify for further analysis or forward modelling, as detrending always causes artefacts on the signal variability.

FURTHER USED PROFILES

- For the further analysis and forward modelling the profile from the 2nd approach of archive piece correction (AC2) and 2nd approach of offset correction (OC2) is used, as it contains the exact and artefact-free variability of the DEP data.
- For the conversion of depth to two-way traveltime the hybrid profile from densitybased trend and DEP variability is used as it contains the correct trend.

5.3 RESULTS AND DISCUSSION OF THE DIELECTRIC PROFILING: PERMITTIVITY- AND CONDUCTIVITY-DEPTH PROFILES

The above DEP processing resulted in depth profiles of the real relative dielectric permittivity and the electric conductivity depicted in Figure 5.9.

5.3.1 ANALYSIS OF THE PERMITTIVITY AND CONDUCTIVITY PROFILES

Visual examining of the permittivity- and conductivity-depth profiles (cf. Figure 5.9) yields that

- the trends are strictly monotonic and converge with depth asymptotic against constant thresholds,
- the variabilities are strong in lower depths and diminish continuously with depth,
- large sharp peaks are not cogniscible,
- the trends of permittivity and conductivity seem to be anti-correlated on global scale,
- in lower depths exist on smaller scale singular correlated peaks,
- below 90m decrease permittivity and conductivity correlated,
- a seasonal signal becomes not obvious.

CORRELATIONS OF DEP DATA WITH DENSITY AND CHEMICAL CONCENTRATIONS

Past studies on polar sites established for DEP data

- an empirical relation (cf. Equation (3.11), Section 3.2.3) between conductivity and impurity depositions [Wolff *et al.*, 1997a,b, 1995, Moore *et al.*, 1994, 1992, 1990],
- a dependence (cf. Equations (3.5) to (3.7), Section 3.1.3) of particularly real relative permittivity and in minor degree conductivity on density [Wilhelms, 2005, 2000, 1996] (cf. Section 3.2.3),

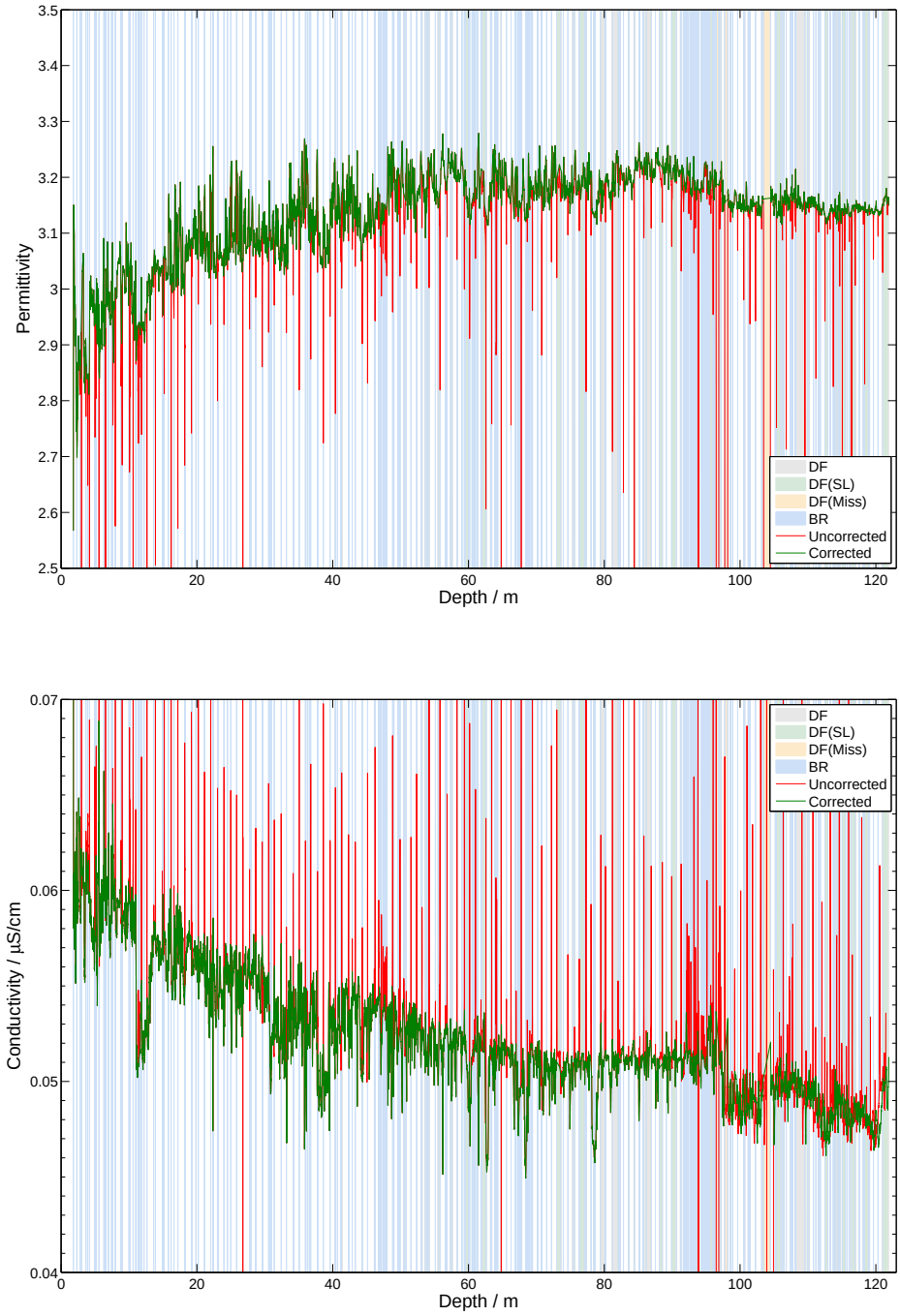

Figure 5.9: Permittivity- and conductivity-depth profiles of the CDM ice core before (red) and after (green) the correction of defects by linear interpolation. The high and sharp peaks of the uncorrected data originate from the breaks between the separate ice core pieces.The shading in the background displays the local kind of defect, that had to be corrected: DF = defective and partially missing ice core volume (grey); DF(SL) = defects from slices (green); DF(miss) = missing ice core parts (yellow); BR = breaks (blue). Bedrock lies at 121m.

- a density-conductivity mixed permittivity (DECOMP)[15] [Wilhelms, 2005] (cf. Equation (3.7), Section 3.2.3).

However, due to the problems that occurred whilst measurements (cf. Section 5.1.3) and the consequent deviation of the measured data from the true course, the measured values were not expected to agree with complementary data calculated from density or chemical concentration on basis of Equations (3.11) or (3.5) to (3.7). E.g. examine the deviation between density- and DEP-based permittivity of the CDM core in Figure 5.8. Non the less it was of interest, whether correlations between the permittivity and conductivity-depth profiles of the CDM core and with data of density and chemical concentrations existed, that could qualitatively confirm the relations listed above.

Density data from the CDM core in half-meter resolution was supplied by Preunkert et. al [2012, personal communication] and, as till the moment of going to press with this thesis chemical concentrations of the CDM core were not available, ion-chromatographic derived impurity concentrations of the CDK core by Preunkert and Legrand [2013].

The subsequent correlations are calculated using a discrete implementation of the classical Pearson Correlation Coefficient [cf. Mudelsee, 2010]. They are partially calculated as (here) so-called absolute correlations on the complete data sets from surface to bedrock and partially as so-called depth-dependent correlations in windows shifted along the depth axis in equidistant steps (cf. Appendix D.2).

CORRELATIONS WITH CHEMICAL CONCENTRATIONS The calculation of correlations of the CDM core's DEP data with impurity concentrations of the CDK core involved the rescaling of the CDK's depth axis using its age-depth profile (cf. Section 2.2.1) by about 33.5m, the depth equivalent of eight years. Thus the common data only covered the depth interval between 33.5m and 119m with a large uncertainty about its certain offset. The probability of finding any correlations consequently was a remote one and no correlations could be found, neither on the complete common length of the data sets, nor depth-dependent (e.g. cf. the depth-dependent correlations with ammonium and calcium in Appendix B.3). All calculated correlation coefficients were scattered around zero. However, a change of variability of the ion-chromatographic data below the rescaled depth of 90m was observable and is further investigated subsequently in this section.

CORRELATION WITH DENSITY The expected dependency of the real relative dielectric permittivity on density is confirmed by a relative high Pearson's correlation coefficient of 0.81.

CORRELATION OF PERMITTIVITY AND CONDUCTIVITY Calculations over the complete core length yield a visible anti-correlation of -0.61. The depth dependent correlations on scales from 30m to 90m in Figure 5.10 however reveal a shifting from an anti-correlation in lower depths to a strong correlation of 0.6 to 0.8 in higher depths below 90m, the later cogniscible on all scales from 1m to 90m. This confirms the visual observation at the beginning of this section. Note that the anti-correlation in lower depths, which is distinctly visible in the trends of the data, might partially be an artefact of the measurement of the core pieces 1 to 63 as archive pieces (cf. Section 5.1.3), for which's non-linearity the applied correction did not account (cf. Section 5.2.1). Compare therefor in Figure 5.13 the DEP profiles of the cores KCO and KCC from Colle Gnifetti (CG), which's trends do not display a visible anti-correlation.

The above investigation in correlations could only confirm the expected density dependency of permittivity unambiguously. It was hampered in the other two cases by shortcomings of the data. However, the shift in the depth-dependent correlation of permittivity and conductivity on intermediate scales from

[15] Density-conductivity mixed permittivity (DECOMP) describes a formal relation of the firn's permittivity and conductivity due to the complex mixing of its constituents' (ice and air) dielectric properties depending on their volume fractions and thus the firn's density.

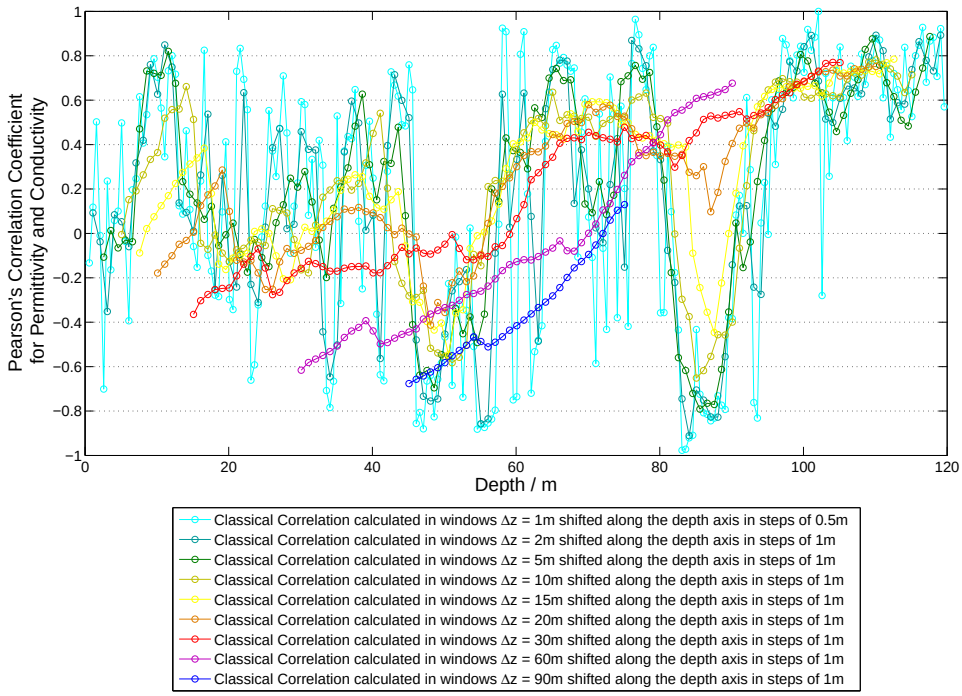

Figure 5.10: Depth-dependent correlations between real relative permittivity and conductivity of the CDM core, calculated in windows of various size shifted along the depth axis in equidistant steps. A point in the correlation-depth diagram in a distinct depth z represents the absolute correlation calculated on data in the depth interval $[z-\Delta z_{window}/2,\, z+\Delta z_{window}/2]$ (cf. Appendix D.2). Apparently their prevails a general anti-correlation on large scale, on intermediate scales a shift from strongly anti-correlated in smaller depths to strongly correlated in larger depths, i.e. below 90m, while on small scales no unambiguous correlation is observable. Bedrock lies at 121m.

strongly anti-correlated to strongly correlated indicates a distinctive change of ice core properties below a depth of ca. 90m and suggests further investigation therein.

SEASONALITY

Both for polar and Alpine sites there have been seasonalities in density and in particle deposition reported. For Greenland and Antarctica Li *et al.* [2007], Zwally and Jun [2002], Gerland *et al.* [1999] observed seasonalities in firn densification and thus density and Kuramoto *et al.* [2011], Rasmussen *et al.* [2006] for aerosol and particle depositions. For Alpine sites, e.g. for Col dû Dome (CDD), Preunkert and Legrand [2013], Legrand *et al.* [2013] reported an annual signal in deposition of e.g. ammonium. As the real relative permittivity in DEP measurements of glacier ice cores depends mainly on density and the electric conductivity mainly on impurity concentrations (cf. Section 3.2.3), e.g. of ammonium, it could be expected that a seasonal signal might be contained in the permittivity- and conductivity-depth profiles of the CDM core.

Ice core records however are defying time series as time increases not linear with depth, hence the frequencies of possibly existent seasonal signals shift continuously with depth. As an initial visual analysis and a simple Fourier analysis could not uncover any seasonality, a continuous-wavelet transformation[16]

[16] The applied continuous wavelet transformation 'expands time series into time frequency space and can therefore find localized intermittent periodicities.' [Grinsted *et al.*, 2004]

[Grinsted *et al.*, 2004] was applied on the detrended[17] permittivity and conductivity profiles (cf. Figure 5.11). It yielded that

- the contributions of all periods to the signals amplitude generally diminish with depth, which is no surprise, as the compression of firn to ice reduces density variations with depth and nearly annihilates them below the firn-ice transition,
- particularly significant contributions to the signals amplitude of medium period diminish with depth and predominantley vanish below 90 meters confirming the argument of above,
- an unambiguous seasonality could not be disclosed.

Possible explanations for the absence of a seasonal signal on the DEP data are

- the huge ratio of defective data,
- the especially large effect of firn densification on possible seasonal signals due to the small number of annual cycles contained in the firn Section of the core, caused by the very high annual net accumulation at CDD; note that the upper 60 meters of the core only contain the snow deposition of 17 years (cf. Figure 6.2),
- disturbances of the glaciers stratigraphy caused by an crevasse on the flow line above the drilling site of the CDM ice core (cf. Sections 2.2.1 and 4.3.1).

CHANGE IN THE VARIABILITY OF THE DATA

Previous analysis indicated that below a depth of about 90m some change takes place with the variability of the DEP data as well as of the ion-chromatographic data. Therefore some further investigation on the variability was conducted, comparing the variability of permittivity and conductivity, derived by detrending using an eigenvalue decomposition (cf. Figure D.1), and the concentrations of the ion-chromatographic data on the scales of there standard deviations.

Apparently the variability of all profiles diminishes significantly below 90m. This is most distinctly visible in the variance of the permittivity and the concentrations of SO_4 and NO_3. While 1σ-events here are rather the usual in depths above 90m there remain only 3-5 in the 30m-interval below (cf. Figures 5.12 and B.6).

TRANSITION OF ALPINE ICE CHEMISTRY FROM ALKALINE TO ACID REGIME

The change of ice core properties below ca. 90m, indicated by the above investigations, could possibly stay in relation with a regime change in Alpine ice chemistry from slightly alkaline to acid in the 1950s [Wagenbach *et al.*, 1988, Wagenbach and Geis, 1989, Wagenbach *et al.*, 2012] (cf. Figure 2.3, Section 2.2.1), as the time span from 1950 to 1960 corresponds in the CDM ice core to a depth of 101m to 92m.[18] This assumption particularly is confirmed by the fact that a change in variability was not only observable in the DEP signals of the CDM core but in impurity concentrations of the CDK core, too (cf. Figure 5.12).

[17] Detrending was conducted by an eigenvalue decomposition using the software AutoSignal, (cf. Figure D.1).
[18] The age-depth conversion was conducted on basis of the CDK core's age-depth profile (cf. Figure 2.4).

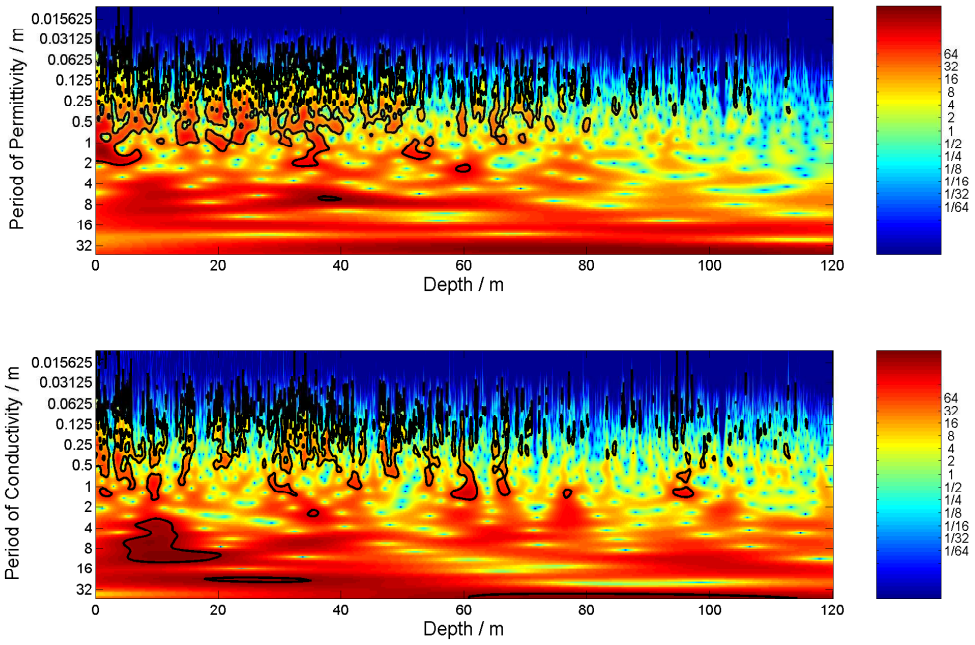

Figure 5.11: Continuous wavelet transformation [Grinsted *et al.*, 2004] of the permittivity- (top) and conductivity-depth profile (bottom). The figures display the contribution of oscillations of a certain period (y axis) to the permittivity- res. conductivity-depth profiles in a certain depth (x axis). The amplitude of the contribution of a certain period in a certain depth is represented by colours corresponding to the colour bar at the right. I.e. high contributions are plotted in dark red while small ones are plotted in dark blue. Significant contributions (delimited from their surrounding by more then one standard deviation) are emphasized by black borders. Bedrock lies at 121m.

SUMMARY OF THE ANALYSIS

- No correlation between the DEP data of the CDM core and chemical concentrations of the CDK core could be established, thus not excluding possible correlations to chemical concentration data of the CDM core, which is at present not available.

- Permittivity and conductivity are anti-correlated on global scale, but show on intermediate scale below a depth of ca. 90m a strong correlation.

- The expected correlation between permittivity and density can be confirmed.

- No seasonality can be detected on the DEP data.

- A significant diminishing of the variability of the DEP data of the CDM core and chemical concentrations of the CDK core below ca. 90m is observable.

- **A change of the ice properties below ca. 90m is suggested!** It could be caused by the regime change in Alpine ice chemistry from slightly alkaline to acid in the 1950s (which correspond to a depth of 92m to 101m).

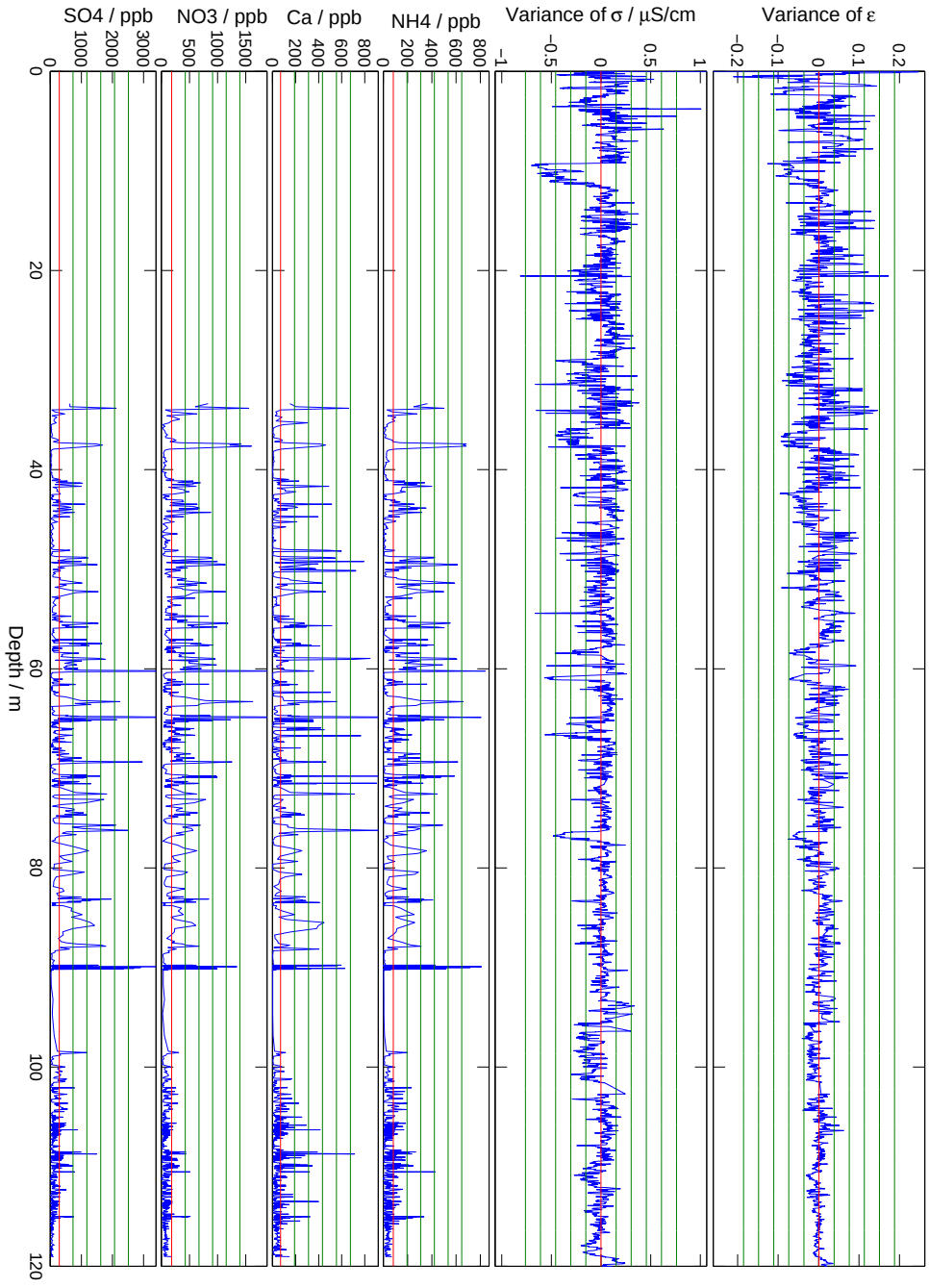

Figure 5.12: Variabilities of the detrended permittivity and conductivity profiles (cf. Figure D.1) and the impurity concentrations of SO_4, NO_3, Ca and NH_4 (blue). Further depicted are the signals mean values (red line) and standard deviations (green lines). Note the reduction of signal variabilities below ca. 90m. Bedrock lies at 121m.

5.3.2 Comparison with further DEP Records

Subsequently the DEP profiles of the CDM ice core from Col du Dôme (CDD) are compared to data sets of the firn core KCO and the deep ice core KCC from Colle Gnifetti (CG). Recall that CDD and CG are characterised by complementary net-surface accumulations and thus time scales of their ice cores (cf. Section 2.1).

The DEP profiles of the KCO core only cover the firn region of CG and were derived within a Bachelor thesis by Jepsen [2010]. The profiles of KCC where derived at the end of this thesis. They were collected with a comparable setup, only deviating from the above (cf. Section 5.1.1) by the use of the originally belonging HP 4284A Precision LCR Meter and the preceding and well established software. Their processing followed the same path as the on of the CDM core (cf. Figure 5.2, Section 5.2). As the core was of very good quality and as the setup worked faultless this time, it did not need any archive piece or offset corrections and defect corrections, too, only afflicted 2% of the core.

The real relative permittivity and conductivity depth profiles of the three cores are compared on relative depth scales (relative to bedrock) in Figure 5.13.

- The profiles from CG are apparently in very good agreement both for permittivity and conductivity, while the profiles of the CDM core from CDD deviate. Also in good agreement to the permittivity profiles of CG, however, is the density-based permittivity profile calculated by Looyenga's Formula (cf. Equation (3.5), Section 3.1.3). This confirms, that the true courses of the CDM core's profiles should have followed the same trend as the ones from the core from CG.
- The variability of the profiles from CG is by more then one order higher as the one of the CDM core's profiles. Particularly the conductivity profiles from CG display large and distinctive peaks as they are known from polar sites [e.g. Eisen *et al.*, 2003b,c] but miss in the CDM core's conductivity profile.
- Both the profiles from CG and CDD display different conductivity regimes. As discussed before (cf. Section 5.3.1) for the CDM core from CDD this is possibly caused by the regime transition in Alpine chemistry in the 1950s [Wagenbach *et al.*, 1988, Wagenbach and Geis, 1989, Wagenbach *et al.*, 2012] (cf. Figure 2.3, Section 2.2.1). Even though no dating for the cores KCC and KCO was available, a rough estimate on basis of a net-surface calculation of 0.2-0.4 m w.e./a for CG (cf. Section 2.1), density profiles of the cores and the assumption of only vertical flow suggests that the observable change might lie in the same time window.

5.3.3 Uncertainties

Uncertainties of the Permittivity- and Conductivity-Depth Profiles

Error of Depth As discussed in Wilhelms [1996, p.114] the error of depth origins mainly from the uncertainty in the reconstruction of the ice core from separately drilled core segments while logging. As in case of the CDM ice core, it consists of the uncertainty in the reconnection of adjacent core segments and of the length of completely destroyed core segments, which amounts to $\Delta z_n = \Delta z \approx 1$cm per core segment n for all n. With Gaussian Error Propagation consequently holds for the error Δz_N in the depth z_N of a core segment N:

$$\Delta z_N = \sqrt{\sum_{n=1}^{N} (\Delta z_n)^2} = \sqrt{N}\Delta z \qquad \text{with} \qquad z_N = \sum_{n=1}^{N} z_n \tag{5.3}$$

Thus for core segments of comparable lengths the relative depth error diminishes with depth, i.e. he amounts for the CDM core near the surface in the depth $z_5 \approx 3.3$m of core segment 5 to $\frac{\Delta z_5}{z_5} \approx 0.68\%$

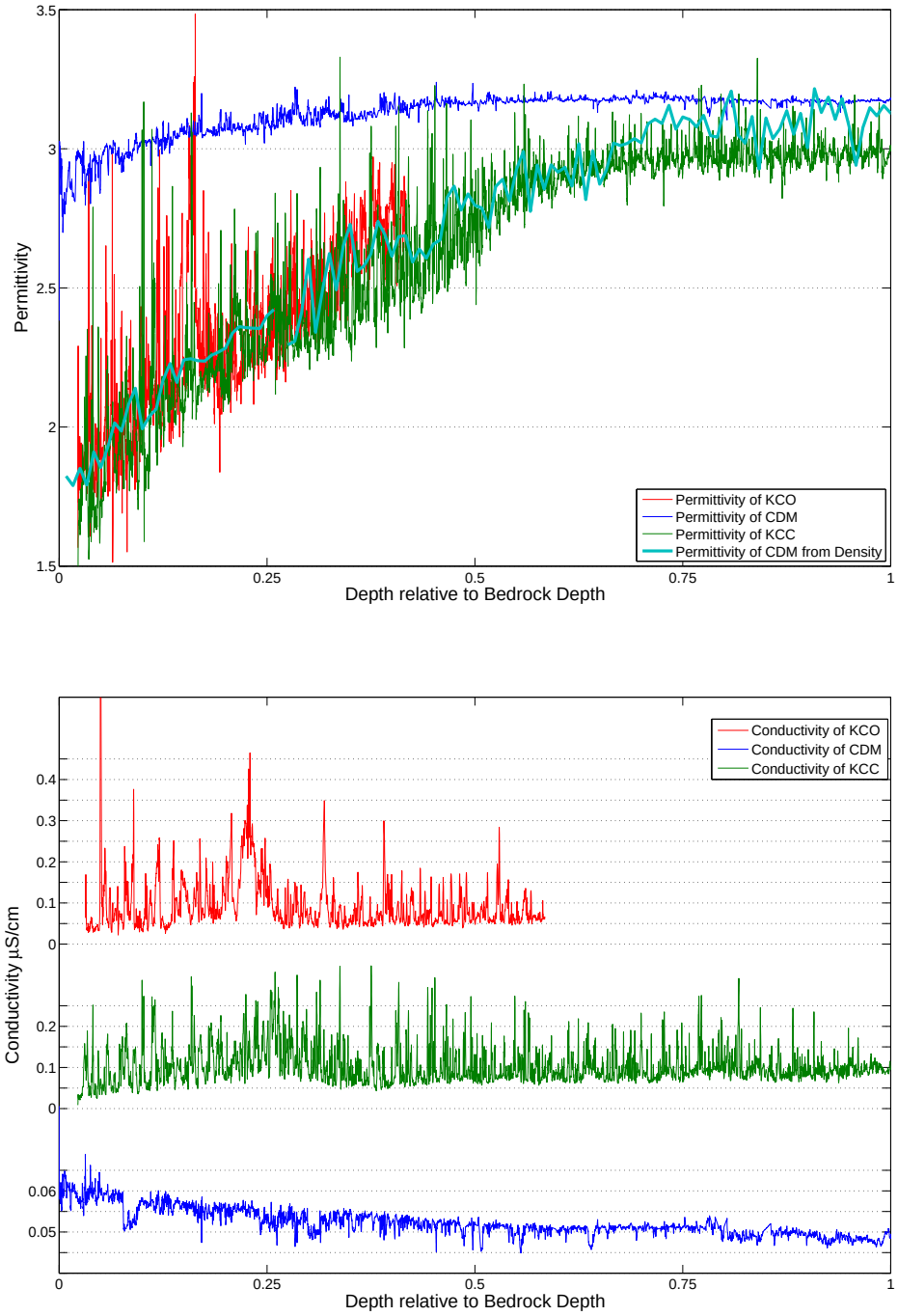

Figure 5.13: Comparison of permittivity- (top) and conductivity-depth profiles (bottom) of the Alpine ice cores CDM from Col du Dôme and KCO and KCC from Colle Gnifetti on relative depth scale (relative to bedrock). On the x axis 0 denotes the glacier surface and 1 the bedrock.

respectively in the depth $z_{63} \approx 52$m to $\frac{\Delta z_{63}}{z_{63}} \approx 0.14\%$ and at bedrock in depth $z_{159} \approx 121$m to $\frac{\Delta z_{159}}{z_{159}} \approx 0.10\%$ corresponding to an absolute depth error of $\Delta z_{159} \approx 12.6$cm.

UNCERTAINTIES OF PERMITTIVITY AND CONDUCTIVITY The total uncertainties of permittivity and conductivity of the CDM core can be divided into

- errors generally arising from the method DEP,
- uncertainties due to the specific problems with the CDM core's DEP

The general errors from DEP originate for empty measurements and ideal cores from [Wilhelms, 1996, 2000]

- uncertainties of the used LCR Meter as dominating contribution to the total error,
- uncertainties of the environmental temperature, and
- errors of the electrode diameter and electrode distance of the DEP bench as minor contributions.

For measurements using a calibrated LCR Meter HP 4284A in the capacitance range $C = 0.06$pF to 0.19pF and for temperatures in the range of $T = 243$K to 263K with an uncertainty of $\Delta T = 1$K Wilhelms [2000] specifies maximum relative errors of 3.5% for permittivity and 7.5% for conductivity. The measurements of the CDM core after offset correction lay in the same capacitance range, they used an improved LCR Meter HP 4285A with comparable smaller uncertainties and were conducted at $T = (262 \pm 1)$K. So transferring the errors by onto the measurements of the CDM core this would mean that the absolute error of permittivity in the ice range for the profiles (OC2 AC2) and (OC2 AC3) with $\varepsilon'_{z\to\infty} = 3.2$ would amount to $\Delta\varepsilon' = 0.11$ and for profile (OC1 AC2) with $\varepsilon'_{z\to\infty} = 3.7$ to $\Delta\varepsilon' = 0.13$ (cf. Figure 5.8).

The uncertainties due to the specific problems with this core's DEP demonstrate themselves in the deviations between the different profiles of about four to fife times the above errors. Obviously they constitute the dominating contributions to the total uncertainties. As discussed before there order cannot be quantified precisely but, following the statement of Wilhelms [1996, p.104ff.] that the true course of the DEP data should lie within an relative uncertainty range of 5% around data calculated from density with the Looyenga Model, the estimated relative uncertainty respectively relative deviation from this expectation of the trend of the profile (OC2 AC2) chosen for the further processing ranges from 30% in lower depths to 5% below the firn-ice transition, whereas the uncertainty of the variability should correspond to the value given by Wilhelms. As discussed above this should not interfere with the interest of this thesis.

6 COMPARISON OF REAL RADARGRAMMS FROM GROUND PENETRATING RADAR SURVEYS WITH SYNTHETIC RADARGRAMMS OUT OF DIELECTRIC-PROFILING-BASED FORWARD MODELLING BY CONVOLUTION

6.1 FORWARD MODELLING BY CONVOLUTION

The subsequent forward modelling approach started on the permittivity- and conductivity-depth profiles of the preceding DEP processing (cf. Figure 5.8, Chapter 5). The approach comprised several stages (cf. Figure 5.2) before the final convolution resulted in a synthetic radargramm. It followed a procedure discussed in Eisen *et al.* [2003b, 2006] and was based on MATLAB code by Eisen *et al.* [2003b], which had to be supplemented by a down-sampling and filtering module.

PIT CORRECTION AND EXTENSION INTO BEDROCK The missing DEP data of the 1.8m deep drilling pit was set to the mean value of the adjacent data in the depth interval from 1.8m to 5m, thus shifting the strong surface reflector back towards surface and reducing uncertainties in the conversion of depth to two-way traveltime. An extension of the dielectric ice core properties with higher bedrock permittivities and conductivities was not conducted, as the GPR radargramms adjacent to the borehole did not reach bedrock either.

DOWN SAMPLING AND FILTERING To align GPR and DEP data in resolution and increment, the DEP data was smoothed with a Gaussian running mean filter with 0.01m window (corresponding to the time resolution of ca. 4ns of the GPR (cf. Section 4.3.2)) and subsequently down sampled by linear interpolation from 0.005m to 0.15m (corresponding to the increment of the GPR traces of ca. 1.7ns). Forgoing this would have lead to a too high deposition of energy of the synthetic wavelet in each depth interval, as the synthetic wavelet would have seen more IRH in finer resolution than the GPR wavelet and consequently would have been reflected more often.

CALCULATION OF COMPLEX RELATIVE PERMITTIVITY AND REFLECTIVITY A complex relative dielectric permittivity $\varepsilon(z)$ and therewith a complex reflectance-depth profile $R(z)$ were calculated by Equations (3.1) and (3.3) from the profiles of the real relative dielectric permittivity and the electric conductivity resulting from the DEP processing (cf. profile (OC2 AC2) in Figure 5.8 and Figure 5.9).

FREQUENCY SCALING The dispersion of the dielectric properties of firn and ice had to be considered as GPR was conducted with frequency $\nu' = 250$MHz and DEP with $\nu = 250$kHz. Therefor, following Wilhelms [2005], Eisen *et al.* [2006] and Jepsen [2010], it was assumed, that in the kHz to MHz range the

real real part ε' of the complex relative permittivity ε (cf. Equation (3.1), Section 3.1.1) was frequency-independent and the imaginary part $\varepsilon'' = \frac{\sigma}{2\pi\nu\cdot\varepsilon_0}$ linearly dependent on frequency. $\varepsilon(\nu)$ was consequently scaled to $\varepsilon(\nu')$ by:

$$(3.1) \Longrightarrow \qquad \Delta\varepsilon = \varepsilon(\nu') - \varepsilon(\nu) = -i\frac{\sigma}{\varepsilon_0}\left(\frac{1}{2\pi\nu'} - \frac{1}{2\pi\nu}\right)$$

In case of the complex relative dielectric permittivity of the CDM core this yields a correction in the order of $\Delta\varepsilon'' = 0.02$. However as discussed, e.g. in Bohleber *et al.* [2012] and Fujita *et al.* [2000], the assumption of a frequency-independent real part ε' does not meet the real observations. Corresponding to Figure 3.1 a further uncertainty of $\Delta\varepsilon' = \pm 0.05$ for the real part of the complex relative dielectric permittivity of the CDM core remains as no formal correction for ε' has been derived yet. The above linear correction of the imaginary part ε'' however meets the empirical observations (cf. Figure 3.2).

Conversion of Depth to Two-way-Traveltime The conversion of depth to two-way traveltimes (TWT) (cf. Section 3.2.2) was conducted on basis of the hybrid profile from density-based trend and DEP-based variability (cf. the light blue profile in Figure 5.8, Section 5.2.7) by a discrete implementation of the Equations (3.2) and (3.8).

Choice of Wavelet As the real wavelet of the used GPR system has not been recorded, a synthetic wavelet, generated by convolution of a Gaussian bell with a sinus function and consisting of three 250MHz cycles (cf. Figure 6.1), was chosen as input signal for the further convolution. Thus, following the considerations of Eisen *et al.* [2006] and Jepsen [2010].

In theory best resolutions of the subsurface could be gained by a wavelet consisting of one sharp pulse that approximates a δ-function as close as possible, e.g. a Ricker wavelet (cf. Figure 6.1). Convolution of a δ-function with the reflectance-TWT profile would practically lead to a radargramm completely equal to the reflectance-TWT profile. However a true wavelet will inevitably have a temporal extension with time-dependently varying amplitudes, yielding for each reflector a bandwidth of contributions of different phase and amplitude superposed in the radargramm. Thus a compromise has to be made to get a good resolution without neglecting the in reality occurring physical superposition effects.

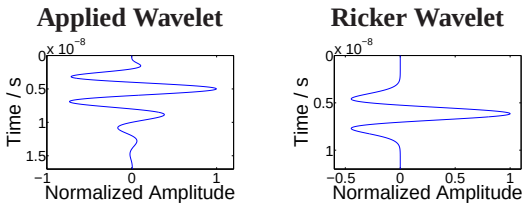

Figure 6.1: Depicted on the left is the applied wavelet consisting of three cycles of 250MHz and on the right a Ricker wavelet of the same frequency.

Convolution Finally the forward modelling was conducted by convolution of the synthetic radar wavelet *w* (cf. Figure 6.1) with the reflectance profile *R* in the time domain using a discrete implementation of the one-sided convolution (3.12). (cf. Section 3.2.4)

6.2 Results and Discussion of the Forward Modelling

After the forward modelling of a synthetic radargramm from DEP data it remained to establish in how far the result reproduces the features of real GPR traces recorded adjacent to the borehole and i.e. if the assignment of appendant reflectors in both radargramms was possible.

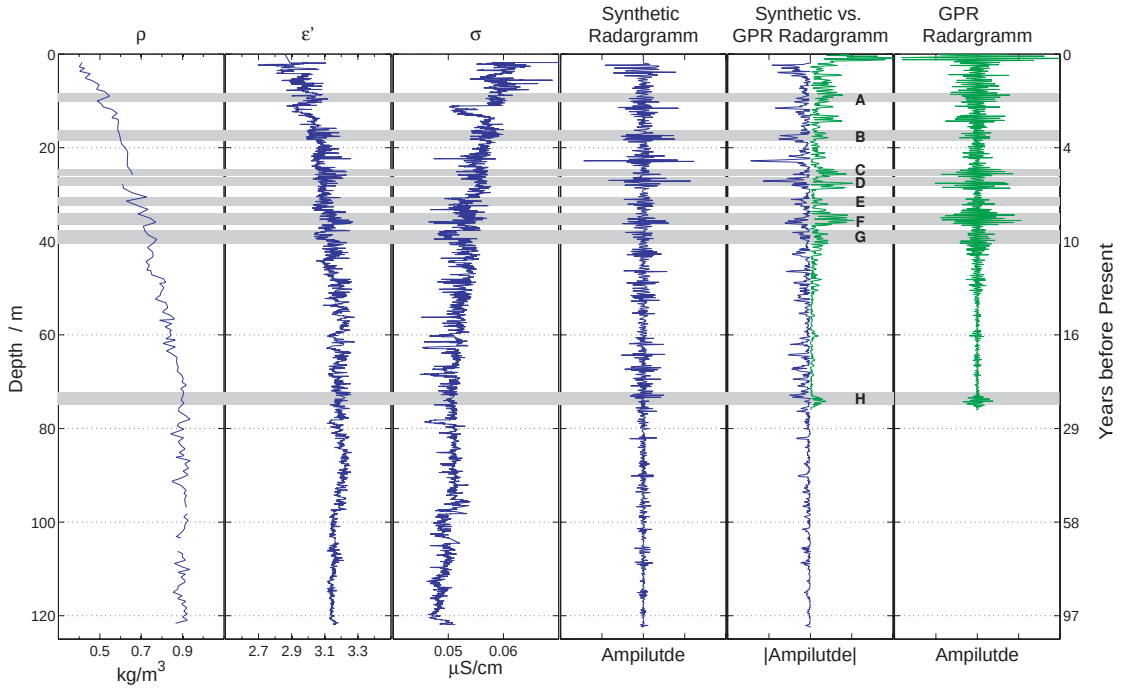

Figure 6.2: Displayed are from left to right the depth profiles of the CDM core from Col du Dôme of density, real relative permittivity, electrical conductivity, synthetic radargramm, power envelopes of synthetic vs. GPR radargramm and GPR radargramm. Special events A, B, ... H referred to in the text are highlighted by grey bars. On the left ordinate given is the depth, bedrock lies at 121m, on the right ordinate given is the age before present (2012) derived from the age-depth profile of the CDK core.

Therefor the synthetic radargramm was compared with a stack of the five closest traces to the borehole from radargramm 121601 (cf. Figure 4.1).[19] For better comparison both the real and the synthetic radargramm were normalized over their common length. To make their common features visually more distinctive, they were compared directly by their squared amplitudes, which are proportional to energy and thus called power envelopes. Furthermore, as the typical resolution for deposition events due to the very high net-accumulation at CDD should lie in the range of 10^{-1} to 10^{0} meters, to suppress high frequent noise they were again compared after filtering with a Gaussian running mean with 0.4m-window. In Figure 6.2 the synthetic and real radargramms as well as their power envelopes are compared unfiltered together with the DEP and density profiles of the CDM core. In Figure 6.3 the Gauss-filtered power envelopes of real and synthetic radargramm are depicted, joint by Gauss-filtered power envelopes of the single GPR traces, and the results of several sensitivity studies in the forward modelling discussed in Section 6.2.1.

6.2.1 Comparison of real and synthetic Radargramms

A visual comparison of the real and synthetic radargramms yields that

- the 1.8m-drilling pit afflicts at least the upper 5m of the synthetic radargramm as the strong surface reflection still is shifted down to 1.8m and thus allows no comparison with the real GPR trace in

[19] The five closest shots correspond very well beneath each other and with their stacked mean, which might be seen in Figure 6.3. This corresponds with the result of Section 4.3.1, that the internal reflecting horizons (IRH) recorded by GPR at CDD are coherently traceable over a range of about 100 meters around the borehole of the core CDM.

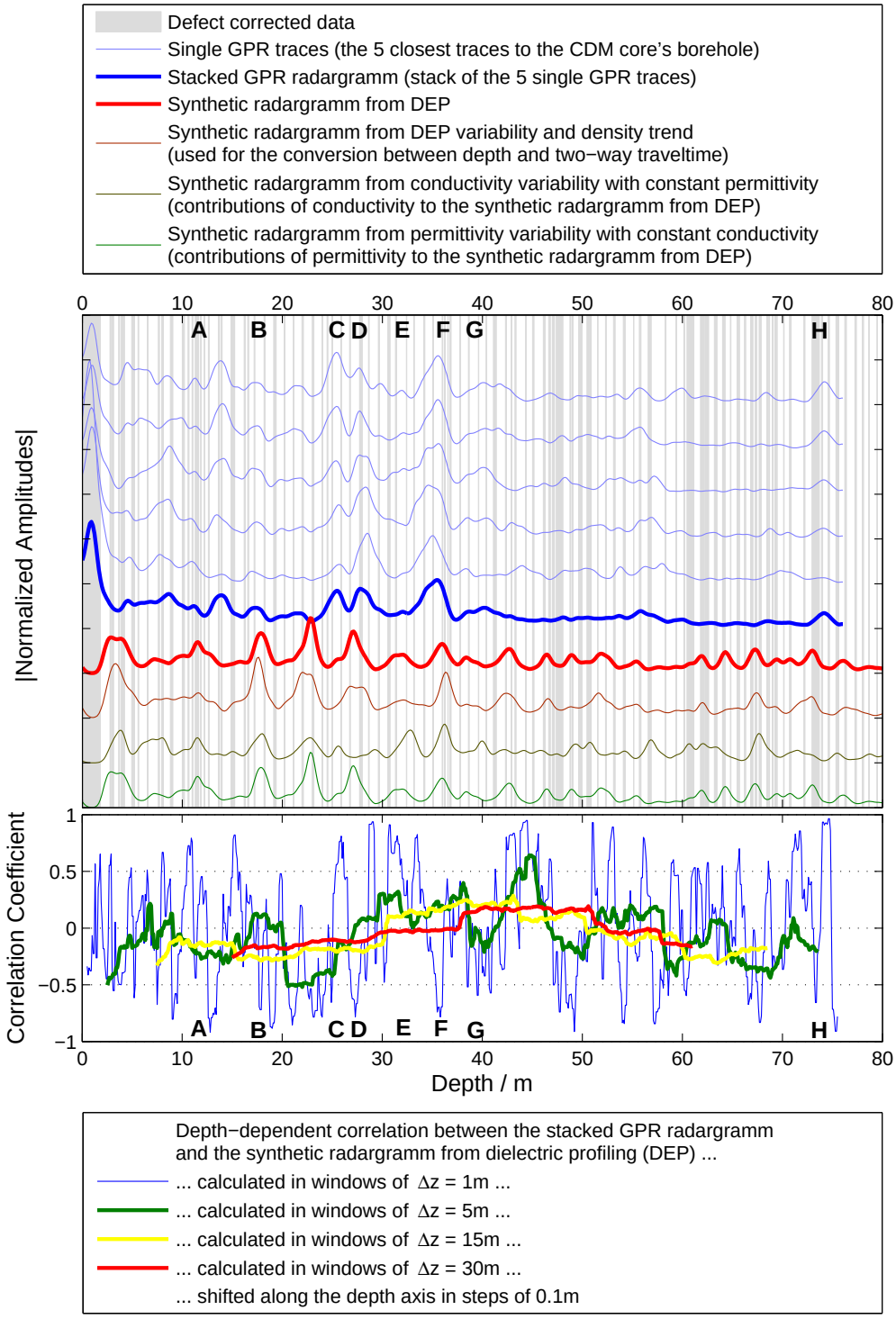

Figure 6.3: Top: Power envelopes of real radar traces from GPR (blue) adjacent to the CDM borehole, synthetic radargramms from two different DEP profiles (red) and sensitivity studies on the origin of the synthetic reflectors (green). The radargramms are filtered with a Gaussian-running-mean with 0.4m window. Defect corrected data is highlighted in grey. **Bottom:** Depth-dependent correlations between the stacked GPR radargramms and the synthetic radargramm from DEP. A point in the correlation-depth diagram in a distinct depth z represents the absolute correlation calculated on data in the depth interval $[z - \Delta z_{window}/2,\ z + \Delta z_{window}/2]$ (cf. Appendix D.2) **Top and Bottom:** Further depicted in both figures are the depths of special events A, B, ... H referred to in the text. Bedrock would lie in a depth of 121m.

this interval,

- no visible accordances are observable in the upper 10 meters,
- several common events seem to exist in the depth interval between 10 and 40 meters consisting in series of peaks visible in both radargramms only varying in amplitude and shifted slightly in phase, they are denoted as A, B, C, ... G and marked in the Figures 6.2 and 6.3, e.g. the most prominent common event F is the strongest reflector of the GPR radargramm,
- in the same interval nevertheless lie two prominent outliers, in the GPR radargramm a peak at ca. 14m and in the synthetic radargramm one at ca. 23m
- below 40 meters no further agreement can be observed, besides a possibly common event H in about 73 to 75 meters depth.

The common events A, B, C, E and G thereby where found to agree well in phase while varying in amplitude, while D, F and H agreed in amplitude while varying in phase by 0.3m to 1m increasing with depth.

CORRELATION BETWEEN REAL AND SYNTHETIC RADARGRAMM

Calculations of absolute and depth-dependent correlations (cf. Appendix D.2) between real and synthetic radargramms on the common depth interval between 0 and 76 meters were not expected to reveal additional informations as they suffered from the same problem as before the ones of the DEP data with chemical concentrations (cf. Section 5.3.1). I.e. the exact depth-dependent phase shift between the time rows was not known and could not be corrected, thus correlations could not be calculated between data points, who were in reality in the exact same depth, but only on such in a assumably common depth interval.

- No absolute correlation could be detected between the un-filtered radargramms (resulting in a Pearson Correlation Coefficient of -0.043) or the Gauss-filtered ones (resulting in a Pearson Correlation Coefficient of -0.061).
- Depth-dependent correlations on the Gauss-filtered radargramms (cf. Figure 6.3) deliver on small scales (i.e. in a shifting 1m-windows) no unambiguous correlations or anti-correlations at the spots of the visually selected events.
- Depth-dependent correlations on intermediate scales (i.e. in a shifting 5m-windows) reveal by ≥ 0.5 correlated areas around the events B, D and F and on larger scales (i.e. in a shifting 30m-windows) a slight general correlation of about 0.3-0.4 for data between 25m and 65m.

ORIGIN OF APPENDANT REFLECTORS

To estimate the dominant contributions to the peaks A till H, two further sensitivity studies were conducted on the forward modelling by convolution, each with one of the two input profiles of the real relative dielectric permittivity and the electric conductivity substituted by constant depth profiles of its mean value. The resulting synthetic radargramms are depicted in Figure 6.3. Comparing them to the non-manipulated synthetic radargramm, one finds

- for all peaks contributions from permittivity and for nearly all peaks comparable contributions from conductivity,
- for D and H solely contributions from permittivity.

Further inquiries as to the origin of the reflectors from density, chemical impurities or crystal fabric orientations might have been interesting, but could not be conducted as no data at all or no data in sufficient resolution was available for the CDM core.

6.2.2 UNCERTAINTIES

Errors and uncertainties in the comparison of real and synthetic radargramms are generally originating from two sources

- deficiencies of the input DEP and GPR data and
- shortcomings of the forward modelling approach by convolution

UNCERTAINTIES ARISING FROM DEFICIENCIES OF THE DATA

A major cause for errors in the forward modelling and thus the synthetic radargramm is missing or defective DEP data. The reconstruction of such inevitably produces artefacts, mostly suppressing real variations in permittivity or conductivity and thus neglecting in reality existent reflectors. This problem is amplified by the fact that breaks and defects while the drilling of the ice core regularly occur at positions with changing ice properties and particularly brittleness, which would appear as strong reflectors in a real GPR radargramm, e.g. ice layers, dust layers, etc. For the CDM core the uncertainties arising from this were huge, as the core was of very poor quality[20]. E.g. the missing counterpart of the outlier in the GPR radargramm in a depth of ca. 14m in the synthetic radargramm might be explained by a series of two close defects of width of 9cm and 14cm falling together with the maximum of this peak. Further errors in the forward modelling may arise from noise in the DEP data. E.g. from aslope layers in the ice core, originating from sastrugi[21] preserved in the glacier or from the steep flow of Alpine glaciers, that would cause spreading losses in a real GPR radargramm but contribute like horizontal layers to the synthetic one.

A further major source for errors in GPR radargramms on Alpine glaciers stems from reflector allocation (cf. Section 3.2.1) due to the small-scaled complex topography of the glaciers bedrock and thus its internal reflecting horizons (IRH). The correction of such is not possible by simple migration approaches frequently used for the correction of scattering in horizontally plane-layered polar glaciers but would require extensive three-dimensional GPR data and complex algorithms. Both do not exist for the CDM core.

SHORTCOMINGS OF THE FORWARD MODELLING APPROACH BY CONVOLUTION

The greatest weakness of the forward modelling approach by convolution lies in the negligence of multiple reflections and due interferences. Thus in the synthetic radargramm might appear peaks that are much smaller or not present at all in the real GPR radargramm, e.g. the outlier in the synthetic radargramm in the approximate depth of ca. 23m might possibly be caused thereby. Furthermore the approach does not consider reflection and absorption losses, i.e. the attenuation of the synthetic wavelets amplitude due to reflection and absorption with depth, with the consequence that reflectors and noise in the synthetic radargramm do not diminish with depth as they do in the GPR radargramm. Neither are the natural dispersion of the wavelet and phase shifts of the complex reflection coefficient at IRH considered.

[20] Recall that 17% of the CDM core's volume was missing or defective and had to be corrected involving 24% of it (cf. Section 5.3.3)

[21] 'Sastrugi are jagged erosional features (often cut into snow dunes) caused by strong prevailing winds that occur after snowfall.' [McHenry, 2010, p.733]

ERROR OF THE TWO-WAY-TRAVELTIME-DEPTH CONVERSION

Finally due to the inability to calibrate the two-way-traveltime-depth conversion with absolute depth-time markers, e.g. from surface and bedrock, there remains an uncertainty about the depth-dependent phase shift between the synthetic radargramm of the CDM core and the GPR radargramm. Gaussian error propagation for the conversion of depth to two-way traveltime with a conservatively estimated relative uncertainty for permittivity of $\frac{\Delta\varepsilon'}{\varepsilon'} = 5\%$ and an error for depth of $\Delta z = 1$cm per core segment (cf. Section 5.3.3) yields a relative error of two-way traveltime of $\Delta t_{TWT}(0.15m)/t_{TWT}(0.15m) = 15\%$ directly beyond the surface, falling rapidly to 3% below a depth of 4m and converging against 2.5% in great depths.

$$\Delta t_{TWT}(z) = \frac{\partial t_{TWT}(z)}{\partial z}\cdot\Delta z + \frac{\partial t_{TWT}(z)}{\partial \varepsilon'}\cdot\Delta\varepsilon' = \frac{2}{c_0}\sqrt{\varepsilon'(z)}\cdot\Delta z + \frac{1}{c_0}\sum_{i=1}^{N(z)}\frac{z_{i+1}-z_i}{\sqrt{\varepsilon'(z_i)}}\cdot\Delta\varepsilon'(z) \tag{6.1}$$

with $\quad \frac{\partial t_{TWT}(z)}{\partial z} \overset{(3.8)}{=} \frac{2}{c(z)} \overset{(3.2)}{=} \frac{2}{c_0}\sqrt{\varepsilon'(z)}$

and $\quad \frac{\partial t_{TWT}(z)}{\partial \varepsilon'} \overset{(3.8)}{=} \frac{1}{c_0}\int_0^z \frac{dz'}{\sqrt{\varepsilon'(z')}} = \frac{1}{c_0}\sum_{i=1}^{N(z)}\frac{z_{i+1}-z_i}{\sqrt{\varepsilon'(z_i)}}$

7 SUMMARY AND CONCLUSION

The main objectives of the thesis, to for the first time measure a complete Alpine ice core with dielectric profiling (DEP), to derive synthetic radargramms and to compare the later with radar traces from ground penetrating radar (GPR), could be accomplished. The CDM ice core from Col du Dôme (CDD) could be measured and, in spite of the challenging core quality and the artefacts from the deficient setup, analysed in full extent, furthermore a partial program leaving the analysis and the comparison with GPR traces could be conducted for the KCC ice core from Colle Gnifetti (CG), which came along in the final stage of the thesis.

The analysis of the DEP profiles of the CDM core

- could observe known dependencies between the real part of the firn's complex relative permittivity and density and, not quite unambiguously, between its real and imaginary part. However, exact relations could not be confirmed due to the problematic data situation, i.e. the comparatively high defect ratio of the core. The known dependency of the imaginary part on impurity concentrations in the ice, could not be confirmed due to missing complementary data.
- could probably detect the transition of Alpine snow chemistry from slightly alkaline to acid in the 1950s [e.g. Wagenbach *et al.*, 2012], which displays itself e.g. by a significant diminishing of both the profiles variability before 1950 and a correlated decrease in both signals trend.
- could not identify absolute time markers from depositions of Sahara dust or Volcano eruptions.
- could not reveal any seasonalities as might have been expected e.g. from annual cycles in firn densification [e.g. Li *et al.*, 2007, Zwally and Jun, 2002, Gerland *et al.*, 1999] or impurity deposition [e.g. Preunkert and Legrand, 2013, Legrand *et al.*, 2013]. This might be caused by either the large defect ratio of the core, the strong impact of firn densification on the very few (due to a large net-surface accumulation) annual cycles in the firn part of CDD or disturbances from a crevasse upstream the flow line of the drilling site.

The DEP profiles of the KCC core allowed a assessment of the large corrections that had to be applied in the DEP processing of the CDM core.

The synthetic radargramm from forward modelling by convolution on basis of the CDM core's DEP profiles

- was able to reproduce several reflectors from GPR traces adjacent to the borehole. Common series of peaks only varying in amplitude and shifted slightly in phase could be detected particularly in the depth interval between 10m and 40m (the firn part of the glacier) and were predominantly caused by permittivity changes. Below that depth interval (in the RFZ) no distinguished correlation between GPR and synthetic radargramm could be detected, above large disturbances from the surface reflector limited the comparison.

The found agreements have to be regarded with caution due to the large defect ratio of the core. On the other hand the exceptionally high net-surface accumulation at CDD and the correspondingly high layer thickness should reduce the effect of defects on cm scale. Besides this, the result stays in general

agreement to the first results from the application of forward modelling by convolution at a polar site, for which Eisen *et al.* [2003b] reports a generally *'good agreement in numerous incidents* [with radar traces recorded adjacent to the borehole] *enabling the identification of distinct reflections'*, and to the conclusion from the first Alpine application on the firn core KCO from Colle Gnifetti (CG) within the Bachelor thesis of Jepsen [2010], which reports local agreements between real and synthetic radargramms whereat only differences in amplitude and phase shifts exist, while only for few segments no agreement could be found.

As by products of the thesis, some results from the analysis of the radargramms from CDD could be obtained.

- A reflector-free zone (RFZ)[22], as it is known from CG [Eisen *et al.*, 2003a], occurs at CDD below the firn-ice transition. The complementary age-depth relation at CDD probably allows to rule out one of the for CG discussed hypothetical contributions to the RFZ [Eisen *et al.*, 2003a], i.e. the supposed buffering impact of the regime transition in Alpine snow chemistry [e.g. Wagenbach *et al.*, 2012].

- CDD is in respect to the picking and the traceability of internal reflecting horizons (IRH) comparable to CG. On CDD, too, IRH can be picked only in the firn part above the RFZ and are there well traceable over nearly the complete study site, the steep slope towards Dôme du Goûter and the crevasse close beyond its top excluded. The errors of tracing are comparable to the ones reported for CG [Bohleber, 2011]. Ice core records of the CDM core and the adjacent cores C10, C11, CDK therefore are representative for the whole study site and can be extrapolated along IRH.

The above results lead to the conclusion that in future DEP should be applied to all Alpine ice cores. It is a non-invasive method that can be applied with little effort after the drilling and before the sawing of the core, it can yield a variety of quickly accessible[23] informations, e.g. on density or on absolute time markers like possibly the regime change in Alpine chemistry in the 1950s. Furthermore the interpretation of radar records from Alpine sites requires information on the glaciers dielectric properties, viz. DEP. Here too, forward modelling could supply the physical connection between GPR and DEP data, as it did on polar sites.

However, to reach an unambiguous verdict further investigations should be conducted. E.g.

- The DEP data of the KCC core should be analysed. This might allow to confirm the known relations from polar sites between the dielectric properties of firn and their causes density and impurity deposition for an Alpine ice core. The investigation of seasonalities might be more successful as the KCC comprises far more annual cycles in its firn part than the CDM. And the supplementation with a dating might reveal whether the already observed change in signal variability, too, lies in the 1950s, thus displaying the regime shift in snow chemistry. As the record of the KCC covers a larger span in time and displays distinctive peaks, it might finally allow to identify absolute time markers e.g. deposition of Sahara dust and from Volcano eruptions.

- The already existing synthetic radargramms on basis of the KCC's DEP data should be compared to GPR traces from CG, which will have to be collected soon. As the synthetic radargramms of KCC are far less hampered by defects than the one of CDM, their comparison with GPR traces from CG might yield a more distinctive agreement and allow a unambiguous assessment of the method.

- A more sophisticated forward modelling approach on basis of the finite-difference time-domain (FDTD) algorithm [Eisen *et al.*, 2003c], which considers phenomena of wave propagation like multiple reflections, etc., should be conducted especially on the promising DEP data set of the KCC, and as it is know available in sufficient quality, too, on the DEP data set of the CDM. The resulting

[22] Note that the Alpine reflector-free zone (RFZ) is not identical to the echo-free zone [Drews *et al.*, 2009] at polar sites.
[23] Presuming of cause that the setup works and the core quality is sufficient.

synthetic radargramms should be compared with both GPR traces and the already existent synthetic radargramms from convolution.

- To establish whether an analogue interpretation of the conductivity record from DEP at Alpine cores to that of polar cores [Wolff *et al.*, 1997a,b, 1995, Moore *et al.*, 1994, 1992, 1990] was possible it would further be of high interest, to measure ECM and chemical concentrations on both cores.

Wer immer strebend sich bemüht,
Den können wir erlösen.

Who strives always to the utmost,
For him there is salvation.

Johann Wolfgang von Goethe,
Faust: The Second Part of the Tragedy, Act V, Mountain Gorges

LISTS

LIST OF FIGURES

List of Tables

List of Acronyms

BP	before present
CG	Colle Gnifetti
CMP	common midpoint
CO	common offset
CDD	Col du Dôme
DECOMP	density-conductivity-mixed permittivity
DEP	dielectric profiling
ECM	electrical conductivity method
EFZ	echo-free zone
FDTD	finite-difference time-domain
GPR	ground penetrating radar
IRH	internal reflecting horizon
m a.s.l.	meter above sea level
m w.e.	meter water equivalent
RFZ	reflector-free zone
RX	receiver
TWT	two-way traveltime
TX	transmitter

BIBLIOGRAPHY

[Arcone and Delaney 2000] Arcone, SA ; Delaney, AJ: GPR images of hidden crevasses in Antarctica. *Proceedings of the Eighth International Conference on Ground Penetrating Radar*. 2000

[Auer *et al.* 2007] Auer, I ; Böhm, R ; Jurkovic, A ; Lipa, W ; Orlik, A ; Potzmann, R ; Schöner, W ; Ungersböck, M ; Matulla, C ; Briffa, K *et al.*: HISTALP—historical instrumental climatological Surface Time Series of the Greater Alpine Region. *International Journal of Climatology*. 2007

[Blindow 1994a] Blindow, N: Reflection amplitudes of 40 MHz monopulse radio echo sounding: Correlation with ice core data and ice dynamics. *Filchner Ronne Ice Shelf Programme, Report*. 1994

[Blindow 1994b] Blindow, N: The central Part of the Filchner-Ronne Ice Shelf, Antarctica: Internal Structures revealed by 40 MHz monopulse RES. *Annals of Glaciology*. 1994

[Bogorodskiĭ *et al.* 1985] Bogorodskiĭ, VV ; Bentley, CR ; Gudmandsen, PE: Radioglaciology. Springer, 1985

[Bohleber 2008] Bohleber, P: Age distribution and $\delta^{18}O$ variability in a low accumulation Alpine ice core: perspective for paleoclimate studies, IUP, University Heidelberg, Diploma Thesis, 2008

[Bohleber 2011] Bohleber, P: Ground-penetrating radar assisted ice core research: The challenge of Alpine glaciers and dielectric ice properties, IUP, University Heidelberg, PhD Thesis, 2011

[Bohleber *et al.* 2012] Bohleber, P ; Wagner, N ; Eisen, O: Permittivity of ice at radio frequencies: Part II. Artificial and natural polycrystalline ice. *Cold Regions Science and Technology*. 2012

[Böhlert 2005] Böhlert, R: Glaziologische Untersuchungen auf dem Colle Gnifetti und auf dem Mt. Blanc: Ermittlung der Eisdickenverteilung und interner Schichten mittels Georadar, Geographisches Institut der Universität Zürich, PhD Thesis, 2005

[Böhm *et al.* 2010] Böhm, R ; Jones, PD ; Hiebl, J ; Frank, D ; Brunetti, M ; Maugeri, M: The early instrumental warm-bias: a solution for long central European temperature series 1760–2007. *Climatic Change*. 2010

[Bronstein 2000] Bronstein, IN: Taschenbuch der Mathematik. Verlag Harry Deutsch AG, Thun, 2000

[Clough 1977] Clough, JW: Radio echo sounding: Reflections from internal layers in ice sheets. *Journal of Glaciology*. 1977

[Cole-Dai *et al.* 2013] Cole-Dai, J ; Ferris, DG ; Lanciki, AL ; Savarino, J ; Thiemens, MH ; McConnell, JR: Two likely stratospheric volcanic eruptions in the 1450 s CE found in a bipolar, sub-annually dated 800-year ice core record. *Journal of Geophysical Research: Atmospheres*. 2013

[Corona *et al.* 2010] Corona, C ; Guiot, J ; Edouard, JL ; Chalié, F ; Büntgen, U ; Nola, P ; Urbinati, C: Millennium-long summer temperature variations in the European Alps as reconstructed from tree rings. Climate of the Past. Copernicus GmbH, 2010

[Cronin *et al.* 2013] Cronin, TM ; Polyak, L ; Reed, D ; Kandiano, ES ; Marzen, RE ; Council, EA: A 600-ka Arctic sea-ice record from Mendeleev Ridge based on ostracodes. *Quaternary Science Reviews*. 2013

[Dahl-Jensen *et al.* 2013] Dahl-Jensen, D ; Albert, MR ; Aldahan, A ; Azuma, N ; Balslev-Clausen, D ; Baumgartner, M ; Berggren, A-M ; Bigler, M ; Binder, T ; Blunier, T *et al.*: Eemian interglacial reconstructed from a Greenland folded ice core. *Nature*. 2013

[Dansgaard 1964] Dansgaard, W: Stable isotopes in precipitation. *Tellus*. 1964

[Debye 1929] Debye, P: Polare Molekeln. Verlag von S. Hirzel, Leipzig, 1929

[Drews *et al.* 2012] Drews, R ; Eisen, O ; Steinhage, D ; Weikusat, I ; Kipfstuhl, S ; Wilhelms, F: Potential mechanisms for anisotropy in ice-penetrating radar data. *Journal of Glaciology*. 2012

[Drews *et al.* 2009] Drews, R ; Eisen, O ; Weikusat, I ; Kipfstuhl, S ; Lambrecht, A ; Steinhage, D ; Wilhelms, F ; Miller, H: Layer disturbances and the radio-echo free zone in ice sheets. *The Cryosphere*. 2009

[Eisen *et al.* 2007] Eisen, O ; Hamann, I ; Kipfstuhl, S ; Steinhage, D ; Wilhelms, F *et al.*: Direct evidence for continuous radar reflector originating from changes in crystal-orientation fabric. *The Cryosphere*. 2007

[Eisen *et al.* 2003a] Eisen, O ; Nixdorf, U ; Keck, L ; Wagenbach, D: Alpine ice cores and ground penetrating radar: combined investigations for glaciological and climatic interpretations of a cold Alpine ice body. *Tellus B.* 2003

[Eisen *et al.* 2004] Eisen, O ; Nixdorf, U ; Wilhelms, F ; Miller, H: Age estimates of isochronous reflection horizons by combining ice core, survey, and synthetic radar data. *Journal of Geophysical Research: Solid Earth (1978–2012)*. 2004

[Eisen *et al.* 2003b] Eisen, O ; Wilhelms, F ; Nixdorf, U ; Miller, H: Identifying isochrones in GPR profiles from DEP-based forward modeling. *Annals of Glaciology*. 2003

[Eisen *et al.* 2003c] Eisen, O ; Wilhelms, F ; Nixdorf, U ; Miller, H: Revealing the nature of radar reflections in ice: DEP-based FDTD forward modeling. *Geophysical Research Letters*. 2003

[Eisen *et al.* 2006] Eisen, O ; Wilhelms, F ; Steinhage, D ; Schwander, J: Improved method to determine radio-echo sounding reflector depths from ice-core profiles of permittivity and conductivity. *Journal of Glaciology*. 2006

[Fujita *et al.* 1993] Fujita, S ; Mae, S ; Matsuoka, T: Dielectric anisotropy in ice Ih at 9.7 GHz. *Annals of Glaciology*. 1993

[Fujita *et al.* 2000] Fujita, S ; Matsuoka, T ; Ishida, T ; Matsuoka, K ; Mae, S: A summary of the complex dielectric permittivity of ice in the megahertz range and its applications for radar sounding of polar ice sheets. *Physics of Ice Core Records*. 2000

[Gagliardini and Meyssonnier 1997] Gagliardini, O ; Meyssonnier, J: Flow simulation of a firn-covered cold glacier. *Annals of Glaciology*. 1997

[Gerland *et al.* 1999] Gerland, S ; Oerter, H ; Kipfstuhl, J ; Wilhelms, F ; Miller, H ; Miners, WD: Density log of a 181 m long ice core from Berkner Island, Antarctica. *Annals of Glaciology*. 1999

[Gerthsen and Meschede 2010] Gerthsen, C ; Meschede, D: Gerthsen Physik. Springer, 2010

[Glen and Paren 1975] Glen, JW ; Paren, JG: The electrical properties of snow and ice. *Journal of Glaciology*. 1975

[Gränicher *et al.* 1957] Gränicher, H ; Jaccard, C ; Scherrer, P ; Steinemann, A: Dielectric relaxation and the electrical conductivity of ice crystals. *Discussions of the Faraday Society*. 1957

[Grinsted *et al.* 2004] Grinsted, A ; Moore, JC ; Jevrejeva, S: Application of the cross wavelet transform and wavelet coherence to geophysical time series. *Nonlinear Processes in Geophysics*. 2004

[Gudmandsen 1975] Gudmandsen, P: Layer echoes in polar ice sheets. *Journal of Glaciology*. 1975

[Haeberli 1976] Haeberli, W: Eistemperaturen in den Alpen. *Zeitschrift für Gletscherkunde und Glazialgeologie*. 1976

[Haeberli *et al.* 1988] Haeberli, W ; Schmid, W ; Wagenbach, D: On the geometry, flow and age of firn and ice at the Colle Gnifetti, core drilling site (Monte Rosa, Swiss Alps). *Zeitschrift für Gletscherkunde und Glazialgeologie*. 1988

[Hafner *et al.* 2013] Hafner, P ; McCarroll, D ; Robertson, I ; Loader, NJ ; Gagen, M ; Young, GHF ; Bale, RJ ; Sonninen, E ; Levanič, T: A 520 year record of summer sunshine for the eastern European Alps based on stable carbon isotopes in larch tree rings. *Climate Dynamics*. 2013

[Hammer 1980] Hammer, CU: Acidity of polar ice cores in relation to absolute dating, past volcanism, and radio-echoes. *Journal of Glaciology*. 1980

[Hempel *et al.* 2000] Hempel, L ; Thyssen, F ; Gundestrup, N ; Clausen, HB ; Miller, H: A comparison of radio-echo sounding data and electrical conductivity of the GRIP ice core. *Journal of Glaciology*. 2000

[Hildebrand 1996] Hildebrand, A: Untersuchung der Laufzeit-und Amplitudenverhalten elektromagnetischer Impulse bei glaziologischen Radarmessungen, Institut für Geophysik der Westfalischen Wilhelms-Universität Münster, Diploma Thesis, 1996

[Hoelzle *et al.* 2011] Hoelzle, M ; Darms, G ; Lüthi, MP ; Suter, S: Evidence of accelerated englacial warming in the Monte Rosa area, Switzerland/Italy. *The Cryosphere*. 2011

[Hofstede *et al.* 2004] Hofstede, CM ; Van De Wal, RSW ; Kaspers, KA ; Van Den Broeke, MR ; Karlof, L ; Winther, J-G ; Isaksson, E ; Lappegard, G ; Mulvaney, R ; Oerter, H *et al.*: Firn accumulation records for the past 1000 years on the basis of dielectric profiling of six cores from Dronning Maud Land, Antarctica. *Journal of Glaciology*. 2004

[Jaccard 1959] Jaccard, C: Etude theorique et experimentale des proprietes electriques de la glace, ETH Zürich, PhD Thesis, 1959

[Jaccard 1965] Jaccard, C: Mechanism of the electrical conductivity in ice. *Annals of the New York Academy of Sciences*. 1965

[Jaccard 1967] Jaccard, C: Electrical conductivity of the surface layer of ice. *Physics of Snow and Ice*. 1967

[Jackson 1999] Jackson, John D.: Classical Electrodynamics. 3rd Edition. John Wiley & Sons Inc., New York, 1999

[Jacobel and Hodge 1995] Jacobel, RW ; Hodge, SM: Radar internal layers from the Greenland summit. *Geophysical Research Letters*. 1995

[Jepsen 2010] Jepsen, K: Leitfähigkeits- und Dichtemessungen an einem alpinen Eiskern, Georg-August-Universität Göttingen, Bachelor Thesis, 2010

[Johari 1976] Johari, GP: Glass transition and secondary relaxations in molecular liquids and crystals. *Annals of the New York Academy of Sciences*. 1976

[Johari and Charette 1975] Johari, Gyan P. ; Charette, PA: The permittivity and attenuation in polycrystalline and single-crystal ice Ih at 35 and 60 MHz. *Journal of Glaciology*. 1975

[Johnsen *et al.* 2001] Johnsen, SJ ; Dahl-Jensen, D ; Gundestrup, N ; Steffensen, JP ; Clausen, HB ; Miller, H ; Masson-Delmotte, V ; Sveinbjörnsdottir, AE ; White, J: Oxygen isotope and palaeotemperature records from six Greenland ice-core stations: Camp Century, Dye-3, GRIP, GISP2, Renland and NorthGRIP. *Journal of Quaternary Science*. 2001

[Konrad 2011] Konrad, H: Characterization of the age distribution and the flow field of an Alpine glacier by a combination of simple flow modeling and ground-penetrating radar, University Heidelberg, Diploma Thesis, 2011

[Konrad *et al.* 2013] Konrad, H ; Bohleber, P ; Wagenbach, D ; Vincent, C ; Eisen, O: Determining the age distribution of Colle Gnifetti, Monte Rosa, Swiss Alps, by combining ice cores, ground-penetrating radar and a simple flow model. *Journal of Glaciology*. 2013

[Kovacs *et al.* 1995] Kovacs, A ; Gow, AJ ; Morey, RM: The in-situ dielectric constant of polar firn revisited. *Cold Regions Science and Technology*. 1995

[Kuramoto *et al.* 2011] Kuramoto, T ; Goto-Azuma, K ; Hirabayashi, M ; Miyake, T ; Motoyama, H ; Dahl-Jensen, D ; Steffensen, JP: Seasonal variations of snow chemistry at NEEM, Greenland. *Annals of Glaciology*. 2011

[Lambert *et al.* 2008] Lambert, F ; Delmonte, B ; Petit, J-R ; Bigler, M ; Kaufmann, PR ; Hutterli, MA ; Stocker, TF ; Ruth, U ; Steffensen, JP ; Maggi, V: Dust-climate couplings over the past 800,000 years from the EPICA Dome C ice core. *Nature*. 2008

[Legrand *et al.* 2013] Legrand, M ; Preunkert, S ; May, B ; Guilhermet, J ; Hoffman, H ; Wagenbach, D: Major 20th century changes of the content and chemical speciation of organic carbon archived in Alpine ice cores: Implications for the long-term change of organic aerosol over Europe. *Journal of Geophysical Research: Atmospheres*. 2013

[Lever *et al.* 2013] Lever, JH ; Delaney, AJ ; Ray, LE ; Trautmann, E ; Barna, LA ; Burzynski, AM: Autonomous GPR Surveys using the Polar Rover Yeti. *Journal of Field Robotics*. 2013

[Li *et al.* 2007] Li, J ; Zwally, HJ ; Comiso, JC: Ice-sheet elevation changes caused by variations of the firn compaction rate induced by satellite-observed temperature variations. *Annals of Glaciology*. 2007

[Looyenga 1965] Looyenga, H: Dielectric constants of heterogeneous mixtures. *Physica*. 1965

[Lüthi *et al.* 2008] Lüthi, D ; Le Floch, M ; Bereiter, B ; Blunier, T ; Barnola, J-M ; Siegenthaler, U ; Raynaud, D ; Jouzel, J ; Fischer, H ; Kawamura, K *et al.*: High-resolution carbon dioxide concentration record 650,000–800,000 years before present. *Nature*. 2008

[Luthi and Funk 2000] Luthi, M ; Funk, M: Dating ice cores from a high Alpine glacier with a flow model for cold firn. *Annals of Glaciology*. 2000

[Matsuoka *et al.* 2003] Matsuoka, K ; Furukawa, T ; Fujita, S ; Maeno, H ; Uratsuka, S ; Naruse, R ; Watanabe, O: Crystal orientation fabrics within the Antarctic ice sheet revealed by a multipolarization plane and dual-frequency radar survey. *Journal of Geophysical Research: Solid Earth (1978–2012)*. 2003

[Matsuoka *et al.* 1996] Matsuoka, T ; Fujita, S ; Mae, S: Effect of temperature on dielectric properties of ice in the range 5–39 GHz. *Journal of Applied Physics*. 1996

[Maxwell 1881] Maxwell, James C.: A Treatise on Electricity and Magnetism. Clarendon Press, 1881

[McHenry 2010] McHenry, Robert: The new encyclopaedia britannica. Encyclopaedia Britannica, 2010

[Millar 1981] Millar, DHM: Radio-echo layering in polar ice sheets and past volcanic activity. *Nature*. 1981

[Miners *et al.* 1997] Miners, WD ; Hildebrand, A ; Gerland, S ; Blindow, N ; Steinhage, D ; Wolff, EW: Forward modeling of the internal layers in radio echo sounding using electrical and density measurements from ice cores. *The Journal of Physical Chemistry B.* 1997

[Miners *et al.* 2002] Miners, WD ; Wolff, EW ; Moore, JC ; Jacobel, R ; Hempel, L: Modeling the radio echo reflections inside the ice sheet at Summit, Greenland. *Journal of Geophysical Research: Solid Earth (1978–2012)*. 2002

[Moore 1988] Moore, JC: Dielectric variability of a 130 m Antarctic ice core: Implications for radar sounding. *Annals of Glaciology*. 1988

[Moore 1993] Moore, JC: High-resolution dielectric profiling of ice cores. *Journal of Glaciology*. 1993

[Moore and Paren 1987] Moore, JC ; Paren, JG: A new technique for dielectric logging of Antarctic ice cores. *Le Journal de Physique Colloques*. 1987

[Moore *et al.* 1990] Moore, JC ; Paren, JG ; Mulvaney, R: Chemical evidence in polar ice cores from dielectric profiling. *Annals of Glaciology*. 1990

[Moore *et al.* 1992] Moore, JC ; Wolff, EW ; Clausen, HB ; Hammer, CU: The chemical basis for the electrical stratigraphy of ice. *Journal of Geophysical Research: Solid Earth (1978–2012)*. 1992

[Moore *et al.* 1994] Moore, JC ; Wolff, EW ; Clausen, HB ; Hammer, CU ; Legrand, MR ; Fuhrer, K: Electrical response of the Summit-Greenland ice core to ammonium, sulphuric acid, and hydrochloric acid. *Geophysical Research Letters*. 1994

[Mudelsee 2010] Mudelsee, M: Climate time series analysis: classical statistical and bootstrap methods. Springer, 2010

[Müller 1962] Müller, F: Zonation in the accumulation area of the glaciers of Axel Heiberg Island, NWT, Canada. *Journal of Glaciology*. 1962

[Navarro and Eisen 2009] Navarro, F ; Eisen, O: Ground-penetrating radar. Pellika, P (ed.) ; Rees, WG (ed.): *Remote sensing of glaciers*. Taylor & Francis, London,, 2009

[Oerter *et al.* 2000] Oerter, H ; Wilhelms, F ; Jung-Rothenhausler, F ; Goktas, F ; Miller, H ; Graf, W ; Sommer, S: Accumulation rates in Dronning Maud Land, Antarctica, as revealed by dielectric-profiling measurements of shallow firn cores. *Annals of Glaciology*. 2000

[Paren 1975] Paren, G: Internal reflections in polar ice sheets. *Journal of Glaciology*. 1975

[Petit *et al.* 1999] Petit, J-R ; Jouzel, J ; Raynaud, D ; Barkov, NI ; Barnola, J-M ; Basile, I ; Bender, M ; Chappellaz, J ; Davis, M ; Delaygue, G *et al.*: Climate and atmospheric history of the past 420,000 years from the Vostok ice core, Antarctica. *Nature*. 1999

[Petrenko and Whitworth 1999] Petrenko, VF ; Whitworth, RW: Physics of Ice. Oxford University Press, 1999

[Preunkert and Legrand 2013] Preunkert, S ; Legrand, M: Towards a quasi-complete reconstruction of past atmospheric aerosol load and composition (organic and inorganic) over Europe since 1920 inferred from Alpine ice cores. *Climate of the Past Discussions*. 2013

[Preunkert *et al.* 2000] Preunkert, S ; Wagenbach, D ; Legrand, M ; Vincent, C: Col du Dôme (Mt Blanc Massif, French Alps) suitability for ice-core studies in relation with past atmospheric chemistry over Europe. *Tellus B*. 2000

[Rasmussen *et al.* 2006] Rasmussen, SO ; Andersen, KK ; Svensson, AM ; Steffensen, JP ; Vinther, Bo M. ; Clausen, HB ; Siggaard-Andersen, M-L ; Johnsen, SJ ; Larsen, LB ; Dahl-Jensen, D *et al.*: A new Greenland ice core chronology for the last glacial termination. *Journal of Geophysical Research: Atmospheres (1984–2012)*. 2006

[Robin *et al.* 1969] Robin, G de Q. ; Evans, S ; Bailey, JT: Interpretation of radio echo sounding in polar ice sheets. *Philosophical Transactions for the Royal Society of London. Series A, Mathematical and Physical Sciences*. 1969

[Roth *et al.* 1990] Roth, K ; Schulin, R ; Flühler, H ; Attinger, W: Calibration of time domain reflectometry for water content measurement using a composite dielectric approach. *Water Resources Research*. 1990

[Shumskii 1964] Shumskii, PA: Principles of Structural Glaciology. Dover Publications, Inc., New York, 1964

[Siegert *et al.* 1998] Siegert, MJ ; Hodgkins, R ; Dowdeswell, JA: A chronology for the Dome C deep ice-core site through radio-echo layer Correlation with the Vostok Ice Core, Antarctica. *Geophysical Research Letters*. 1998

[Steinhage *et al.* 2013] Steinhage, D ; Kipfstuhl, J ; Miller, H: Interpolating accumulation rates by means of internal layering detected by airborne radio-echo sounding. *Symposium on Radioglaciology, Lawrence, KS, USA, September 2013*, 2013

[Stillman *et al.* 2013] Stillman, DE ; MacGregor, JA ; Grimm, RE: The role of acids in electrical conduction through ice. *Journal of Geophysical Research: Earth Surface*. 2013

[Vallot 1913a] Vallot, J: Cartes du Massif du Mont Blanc à l'échelle du 1:20000. *Edition Girard*. 1913

[Vallot 1913b] Vallot, J: Valeur et variations de la température profonde du glacier au Mont Blanc. *CR Hebd. Séances Acad. Sci*. 1913

[Vincent *et al.* 2007a] Vincent, C ; Le Meur, E ; Six, D ; Funk, M ; Hoelzle, M ; Preunkert, S: Very high-elevation Mont Blanc glaciated areas not affected by the 20th century climate change. *Journal of Geophysical Research: Atmospheres (1984–2012)*. 2007

[Vincent *et al.* 2007b] Vincent, C ; Le Meur, E ; Six, D ; Possenti, P ; Lefebvre, E ; Funk, M: Climate warming revealed by englacial temperatures at Col du Dôme (4250 m, Mont Blanc area). *Geophysical Research Letters*. 2007

[Vincent *et al.* 1997] Vincent, C ; Vallon, M ; Pinglot, JF ; Funk, M ; Reynaud, L: Snow accumulation and ice flow at Dôme du Goûter (4300 m), Mont Blanc, French Alps. *Journal of Glaciology*. 1997

[Wagenbach 1992] Wagenbach, D: Special problems of mid-latitude glacier ice-core research. Haeberli, W (ed.) ; Stauffer, B (ed.): *Greenhouse Gases, Isotopes and Trace Elements in Glaciers as Climatic Evidence of the Holocene* Vol. Arbeitsheft Nr. 14. Versuchsanstalt für Wasserbau, Hydrologie and Glaziologie, ETH Zürich, 1992

[Wagenbach 2001] Wagenbach, D: Environmental and Climate Records from High Elevation Alpine Glaciers. ALPCLIM - Final Report, 2001

[Wagenbach *et al.* 2012] Wagenbach, D ; Bohleber, P ; Preunkert, S: Cold Alpine ice bodies revisited: What may we learn from their impurity and isotope content? *Geografiska Annaler: Series A, Physical Geography*. 2012

[Wagenbach and Geis 1989] Wagenbach, D ; Geis, K: The mineral dust record in a high altitude Alpine glacier (Colle Gnifetti, Swiss Alps). *Paleoclimatology and paleometeorology: modern and past patterns of global atmospheric transport*. Springer, 1989

[Wagenbach *et al.* 1988] Wagenbach, D ; Münnich, KO ; Schotterer, U ; Oeschger, H: The anthropogenic impact on snow chemistry at Colle Gnifetti, Swiss Alps. *Annals of Glaciology*. 1988

[Wagner 1996] Wagner, S: Dreidimensionale Modellierung zweier Gletscher und Deformationsanalyse von eisreichem Permafrost, Versuchsanstalt für Wasserbau, Hydrologie und Glaziologie, ETH Zürich, PhD Thesis, 1996

[Waite and Schmidt 1962] Waite, AH ; Schmidt, SJ: Gross errors in height indication from pulsed radar altimeters operating over thick ice or snow. *Proceedings of the IRE*. 1962

[Waldner 2011] Waldner, A: Analyse des 210Pb-Konzentrations-Profils eines Eisbohrkerns des Mont-Blanc-Gebiets hinsichtlich einer ungeklärten Konzentrations-Anomalie, University Heidelberg, Bachelor Thesis, 2011

[Wilhelms 1996] Wilhelms, F: Leitfähigkeits-und Dichtemessung an Eisbohrkernen = Measuring the conductivity and density of ice cores. *Berichte zur Polarforschung (Reports on Polar Research)*. 1996

[Wilhelms 2000] Wilhelms, F: Messung dielektrischer eigenschaften polarer eiskerne = Measuring the dielectric properties of polar ice cores. *Berichte zur Polarforschung (Reports on Polar Research)*. 2000

[Wilhelms 2005] Wilhelms, F: Explaining the dielectric properties of firn as a density-and-conductivity mixed permittivity (DECOMP). *Geophysical Research Letters*. 2005

[Wilhelms *et al.* 1998] Wilhelms, F ; Kipfstuhl, J ; Miller, H ; Heinloth, K ; Firestone, J: Precise dielectric profiling of ice cores: a new device with improved guarding and its theory. *Journal of Glaciology*. 1998

[Williams *et al.* 2012] Williams, RM ; Ray, LE ; Lever, JH: Autonomous robotic ground penetrating radar surveys of ice sheets; using machine learning to identify hidden crevasses. *Imaging Systems and Techniques (IST), 2012 IEEE International Conference on* IEEE (Veranst.), 2012

[Wolff 1995] Wolff, E: Electrical stratigraphy of polar ice cores: principles, methods. *Geophysical Research Letters*. 1995

[Wolff *et al.* 1997a] Wolff, EW ; Miners, WD ; Moore, JC ; Paren, JG: Factors Controlling the Electrical Conductivity of Ice from the Polar Regions A Summary. *The Journal of Physical Chemistry B*. 1997

[Wolff *et al.* 1997b] Wolff, EW ; Moore, JC ; Clausen, HB ; Hammer, CU: Climatic implications of background acidity and other chemistry derived from electrical studies of the Greenland Ice Core Project ice core. *Journal of Geophysical Research: Oceans (1978–2012)*. 1997

[Wolff *et al.* 1995] Wolff, EW ; Moore, JC ; Clausen, HB ; Hammer, CU ; Kipfstuhl, J ; Fuhrer, K: Long-term changes in the acid and salt concentrations of the Greenland Ice Core Project ice core from electrical stratigraphy. *Journal of Geophysical Research*. 1995

[Yilmaz 2001] Yilmaz, Ö: Seismic data analysis: processing, inversion, and interpretation of seismic data. SEG Books, 2001

[Zipf 2013] Zipf, L: Die Untersuchung eines Eisbohrkernes des Col du Dôme auf eine in benachbarten Bohrkernen auftretenden 210Pb-Aktivitätanomalie, University Heidelberg, Bachelor Thesis, 2013

[Zwally and Jun 2002] Zwally, HJ ; Jun, L: Seasonal and interannual variations of firn densification and ice-sheet surface elevation at the Greenland summit. *Journal of Glaciology*. 2002

APPENDIX

A Appendix to Chapter 4

A.1 GPR Measurement Parameters at Col dû Dome

Table A.1: Adjustment of parameters of the ground penetrating radar (GPR) system used for the common offset measurements at Col dû Dome in 2012 [Bohleber, unpublished]. As GPR a RAMAC GPR of Malå Geoscience, Sweden, triggered by an odometer of unknown type supplied by AWI was used.

Radargramm	121601	121603	121604	121605	121606	121607	121609
Frequency / MHz	250	250	250	250	250	250	250
Time Window / ns	738	895	895	895	895	895	928
Samples	2133	2585	2585	2585	2585	2585	2367
Sample Frequency / MHz	2890	2890	2890	2890	2890	2890	2550
Stacks	8	8	8	8	8	8	8
Odometer Distance / m	0.5	0.5	0.5	0.5	0.5	0.5	0.5
Antennae Distance / m	0.36	0.36	0.36	0.36	0.36	0.36	0.36

A.2 Tracing of Internal Reflecting Horizons

Table A.2: Small circle with 3 points of interception and a length of ca. 80m. In the left section are for the point of intersection P149 adjacent to the CDM borehole the corresponding depths and ages to the two-way traveltimes (TWT) of the traced internal reflecting horizons (IRH) H_1 to H_6 listed. In the middle section the TWT of the traced IRH at the points of intersection on the closed circle are listed. In the right section the offsets between the starting point P13 and the endpoint P13 in TWT are given as ΔP13 and in enumerable IRH in between as ΔIRH.

IRH	P149		P13 →	P34 →	P149 →	P13	ΔP13	ΔIRH
	Age BP/a	Depth / m	TWT/ns	TWT/ns	TWT/ns	TWT/ns	TWT/ns	
H_1	1.6	4.655	58.5	57.8	51.9	59.9	+1.4	0
H_2	3.5	14.135	165.4	149.8	159.2	183.7	+15.3	+4
H_3	3.9	17.200	203.8	184.0	198.9	218.3	+14.5	+3
H_4	6.2	25.560	298.3	258.1	295.8	330.1	+31.8	+6
H_5	6.8	28.040	323.5	281.9	323.5	354.3	+26.8	+6
H_6	9.0	35.619	416.9	377.5	413.5	439.1	+22.1	+4

Table A.3: Large circle with 5 points of interception and a length of ca. 360m In the middle section the two-way traveltimes (TWT) of the traced internal reflecting horizons (IRH) H_1 to H_6 at the points of intersection on the closed circle are listed. In the right section the offsets between the starting point P13 and the endpoint P13 in TWT are given as ΔP13 and in enumerable IRH in between as ΔIRH.

IRH	P37 → TWT/ns	P34 → TWT/ns	P149 → TWT/ns	P69 → TWT/ns	P67 → TWT/ns	P37 TWT/ns	ΔP37 TWT/ns	ΔIRH
H_1	58.5	57.8	51.9	47.4	53.6	52.9	-5.6	-1
H_2	165.4	149.8	159.2	138.8	160.2	168.5	+3.1	+1
H_3	203.8	184.0	198.9	178.8	194.8	213.5	+9.7	+2
H_4	298.3	258.1	295.8	274.0	298.6	319.0	+20.7	+3
H_5	323.5	281.9	323.5	303.8	329.7	347.0	+23.5	+5
H_6	416.9	377.5	413.5	383.8	429.0	456.0	+39.1	+7

A.3 Radargramms from Col dû Dome

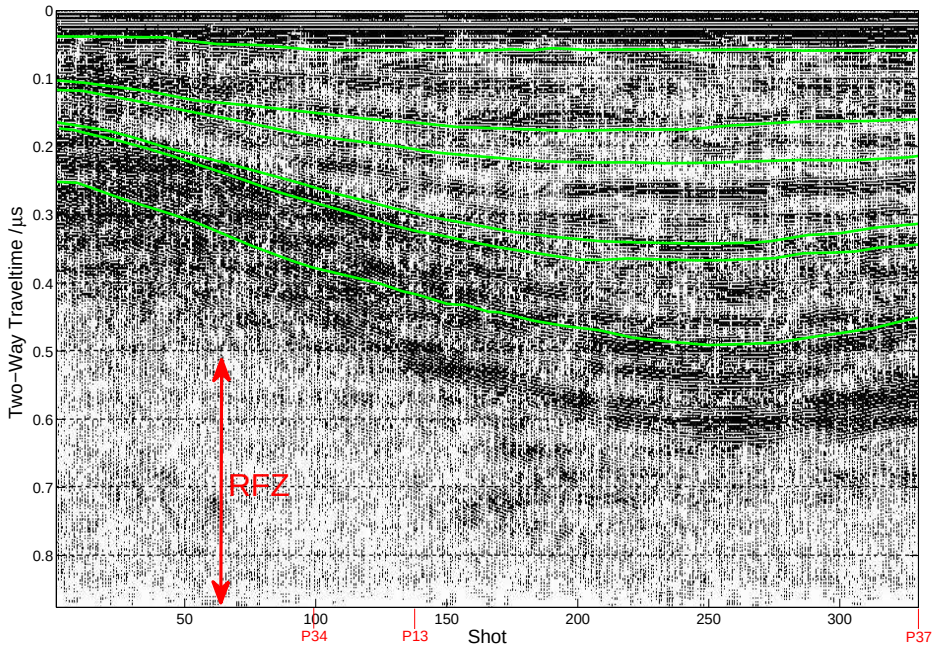

Figure A.1: Radargramm 121603. The radargramm was recorded in direction of the x axis. Its course is mapped in Figure 4.1. Highlighted in the radargramm are in downwards order the picked internal reflecting horizons (IRH) H_1 to H_6 (light green)and the reflector-free zone (RFZ)(red). Marked at the bottom are the points of intersections with other radargramms (red).

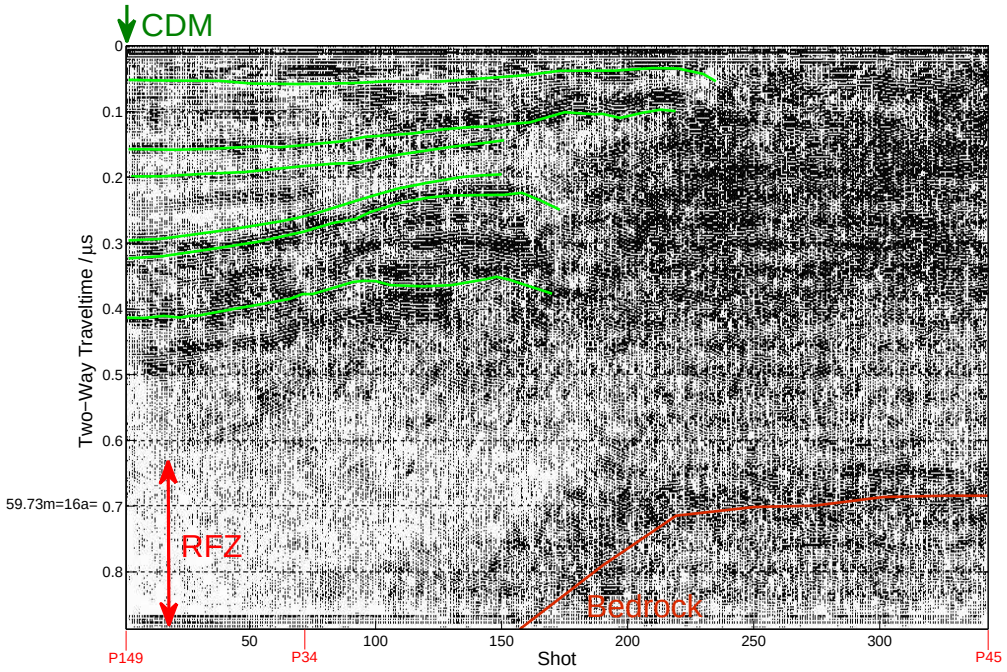

Figure A.2: Radargramm 121604. For description cf. Figure B.2. Additionally highlighted in the radargramm is the assumed course of bedrock (brown). Further marked at the top is the positions of the CDM core's borehole (dark green). For selected two-way traveltimes (TWT) the corresponding local depths and ages before September 2012 at the position of the CDM core are added at the left.

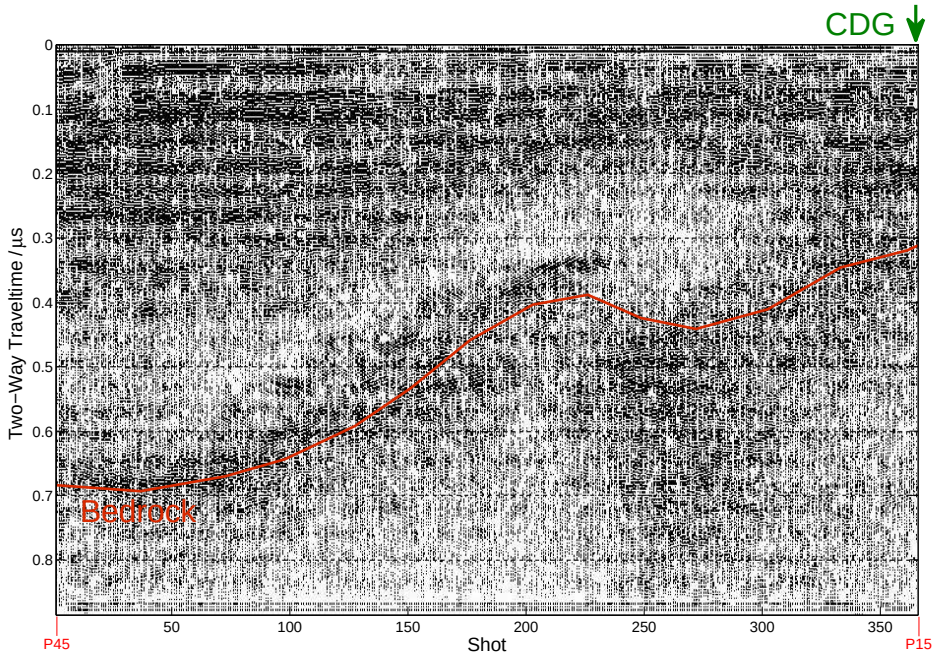

Figure A.3: Radargramm 121605. For description cf. Figures B.2 and B.3. Further marked at the top is the positions of the CDG core's borehole (dark green).

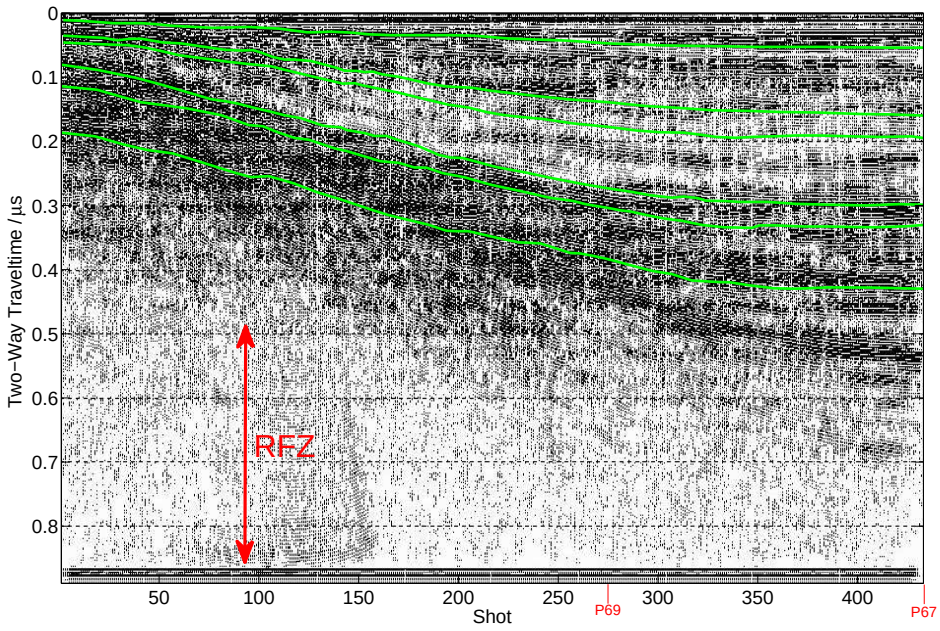

Figure A.4: Radargramm 121606. For description cf. Figures B.2 and B.3.

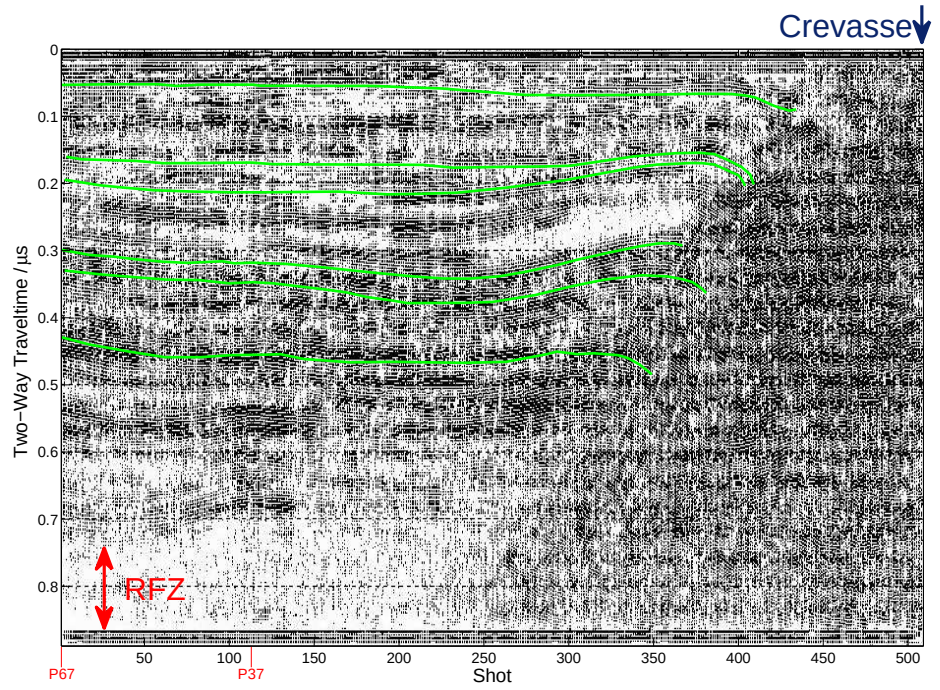

Figure A.5: Radargramm 121607. For description cf. Figures B.2 and B.3. Further marked at the top is the positions of the Crevasse (dark blue).

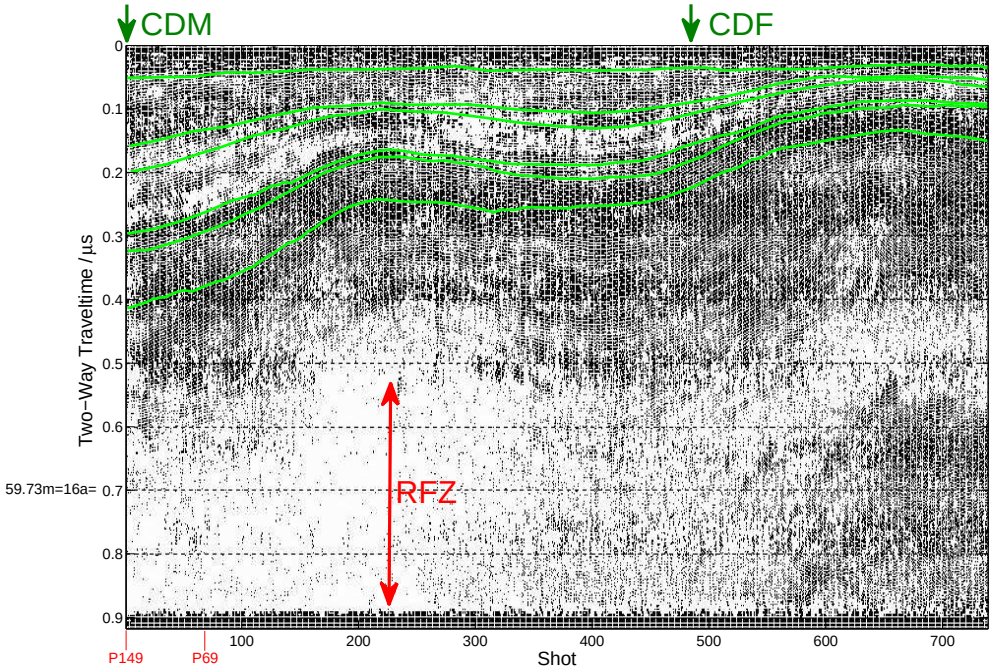

Figure A.6: Radargramm 121609. For description cf. Figures B.2 and B.3. Further marked at the top is the positions of the CDF core's borehole (dark green).

B Appendix to Chapter 5

B.1 Correction of Archive Pieces

Calculations for the 1st Approach: Derivation of non-linear Relations between the measured dielectric Properties of intact Cores and the ones of there appendant Archive Pieces in Series Connection with the the Air Gap

The DEP of the archive pieces of the core segments 1 till 63, 64/65, 72, 80/81 and 88/89 corresponds in principal to the measurement of series connections of the capacitances C_A respectively conductances G_A of the archive pieces and the capacitances C_{G0} respective conductances G_{G0} of the air gap of the missing lamellae that results in measured values of capacitance C_A^* and conductance G_A^*. Where C_{L0} and G_{L0} should be constants as all archive pieces posses the same geometry.

$$\frac{1}{C_A^*} = \frac{1}{C_A} + \frac{1}{C_{L0}} \quad \Longrightarrow \quad \frac{1}{C_A} = \frac{1}{C_A^*} - l \qquad \text{with} \quad m := \frac{1}{C_{L0}} = const. \tag{B.1}$$

$$\frac{1}{G_A^*} = \frac{1}{G_A} + \frac{1}{G_{L0}} \quad \Longrightarrow \quad \frac{1}{G_A} = \frac{1}{G_A^*} - n \qquad \text{with} \quad n := \frac{1}{G_{L0}} = const. \tag{B.2}$$

On the other hand the measurement of the capacitance C and conductance G of the intact core pieces 64/65, 72, 80/81 and 88/89 can be disassembled into series connections of the corresponding archive pieces' values C_A respectively G_A and the belonging lamellae' values C_L respectively G_L:

$$\frac{1}{C} = \frac{1}{C_A} + \frac{1}{C_L} \tag{B.3}$$

$$\frac{1}{G} = \frac{1}{G_A} + \frac{1}{G_L} \tag{B.4}$$

Taking into account that the dielectric vacuum values only depend on the obtained geometry and using simple material laws:

$$C_i = \varepsilon \cdot C_{i0} \qquad \text{with} \quad C_{i0} = const. \tag{B.5}$$

$$G_i = \sigma \cdot G_{i0} \qquad \text{with} \quad G_{i0} = const. \tag{B.6}$$

$$\text{for } i = \{.,A,L\}$$

one gets the relations:

$$
\begin{aligned}
(B.3) \overset{(B.5)}{\Longrightarrow} \quad & \frac{1}{\varepsilon \cdot C_0} = \frac{1}{\varepsilon \cdot C_{A0}} + \frac{1}{\varepsilon \cdot C_{L0}} \quad \Longrightarrow \quad \frac{1}{C_0} - \frac{1}{C_{A0}} = \frac{1}{C_{L0}} = const. \\
\Longrightarrow \quad & 1 - \frac{C_0}{C_{A0}} = \frac{\varepsilon \cdot C_0}{C_L} = const. \quad \Longrightarrow \quad \frac{C_0}{C_{A0}} = const. \\
\Longrightarrow \quad & k := \frac{C}{C_A} = const.
\end{aligned} \tag{B.7}
$$

$$
\begin{aligned}
(B.4) \overset{(B.6)}{\Longrightarrow} \quad & \frac{1}{\sigma \cdot G_0} = \frac{1}{\sigma \cdot G_{A0}} + \frac{1}{\sigma \cdot G_{L0}} \quad \Longrightarrow \quad \frac{1}{G_0} - \frac{1}{G_{A0}} = \frac{1}{G_{L0}} = const. \\
\Longrightarrow \quad & 1 - \frac{G_0}{G_{A0}} = \frac{\sigma \cdot G_0}{G_L} = const. \quad \Longrightarrow \quad \frac{G_0}{G_{A0}} = const. \\
\Longrightarrow \quad & m := \frac{G}{G_A} = const.
\end{aligned} \tag{B.8}
$$

Therewith follow non-linear relations for $C\,(C_A^*)$ and $G\,(G_A^*)$:

$$
(B.1) \overset{(B.7)}{\Longrightarrow} \quad C = \frac{k}{\frac{1}{C_A^*} - l} \tag{B.9}
$$

$$
(B.2) \overset{(B.8)}{\Longrightarrow} \quad G = \frac{m}{\frac{1}{G_A^*} - n} \tag{B.10}
$$

with $k, l, m, n = const.$

CALCULATIONS FOR THE 2ND APPROACH: SIMPLIFIED LINEAR RELATIONS NEGLECTING THE INFLUENCE OF THE AIR GAP

If one neglects the influence of the air gaps on the dielectric measurements of the archive pieces and assumes that instead of (B.1) and (B.2) holds:

$$
C_A^* \approx C_A \tag{B.11}
$$

$$
G_A^* \approx G_A \tag{B.12}
$$

the equations (B.7) and (B.8) yield simplified linear relations for $C\,(C_A^*)$ and $G\,(G_A^*)$:

$$
(B.11) \overset{(B.7)}{\Longrightarrow} \quad \frac{C}{C_A^*} \approx \frac{C}{C_A} = k = const. \tag{B.13}
$$

$$
(B.12) \overset{(B.8)}{\Longrightarrow} \quad \frac{G}{G_A^*} \approx \frac{G}{G_A} = m = const. \tag{B.14}
$$

CALCULATIONS FOR THE 3RD APPROACH: DERIVATION OF THE SET OF PARAMETERS k, l, m, n BY BACKWARDS CALCULATION ON BASIS OF LITERATURE VALUES

In this approach the parameters k, l, m and n are shall be derived from literature values of the permittivity $\varepsilon_{ice}^{lit.}$ and the conductivity $\sigma_{ice}^{lit.}$ of glacier ice and $\varepsilon_{snow}^{lit.}$ and $\sigma_{snow}^{lit.}$ of fresh snow. The backwards calculation already includes the offset correction and starts with the equations (B.21) and (B.22). After inserting of

(B.9) and (B.10) one gets the subsequent systems of equations:

$$(B.21) \overset{(B.9)}{\Longrightarrow} \qquad k = (\frac{1}{C_A^*} - l) \cdot ((C_0 + \Delta C)\varepsilon^{true} - \Delta C) \tag{B.15}$$

$$(B.22) \overset{(B.10)}{\Longrightarrow} \qquad m = (\frac{1}{G_A^*} - n) \cdot ((G_0 + \Delta G)\sigma^{true} - \Delta G) \tag{B.16}$$

If capacitance, conductance and true (literature) values of permittivity and conductivity and therewith by (B.23) and (B.24) the offsets are known for two separate measurements, these equations of two unknown ((k,l) or (m,n)) can be solved. For the frequent archive piece correction one needs the values at the boundaries, the surface of the glacier and the transition between the ice core region measured as archive pieces and the lower one measured as intact cores. The later can be extracted from the data of the intact region after its' offset correction corresponding to the second approach.

FIGURES TO THE 1ST APPROACH

Pieces 64/65

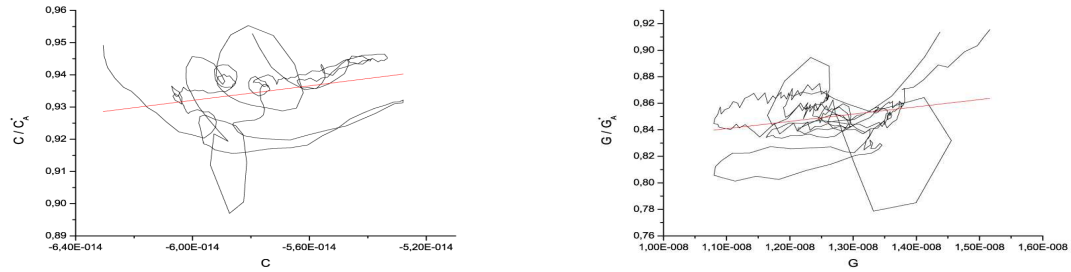

Core Piece 72

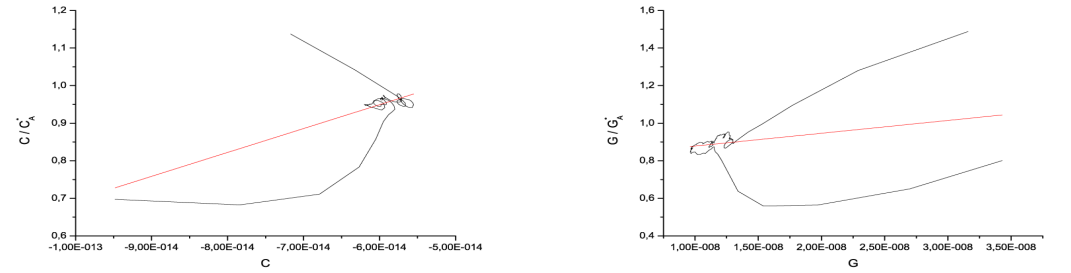

Core Pieces 80/81

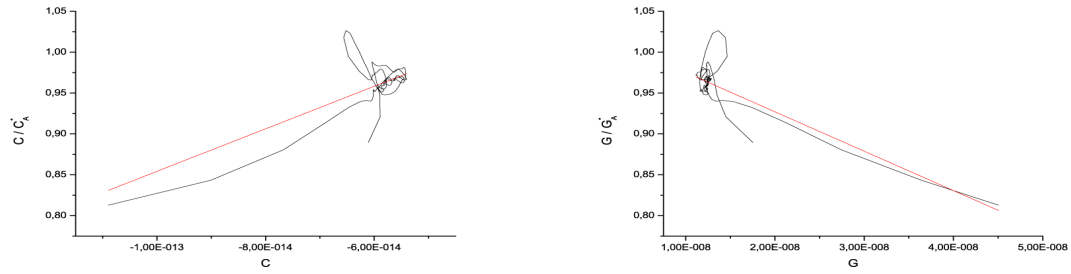

Core Pieces 88/89

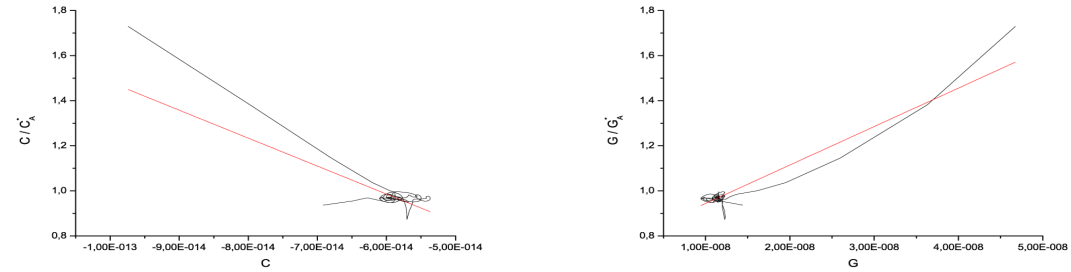

Figure B.1: 1st Approach for the determination of the parameters k, l, m through slopes and ordinate intercepts of line equations on basis of the comparison measurements of intact core pieces and archive pieces of the segments 64/65, 72, 80/81 and 88/89.

FIGURES TO THE 2ND APPROACH

Pieces 64/65

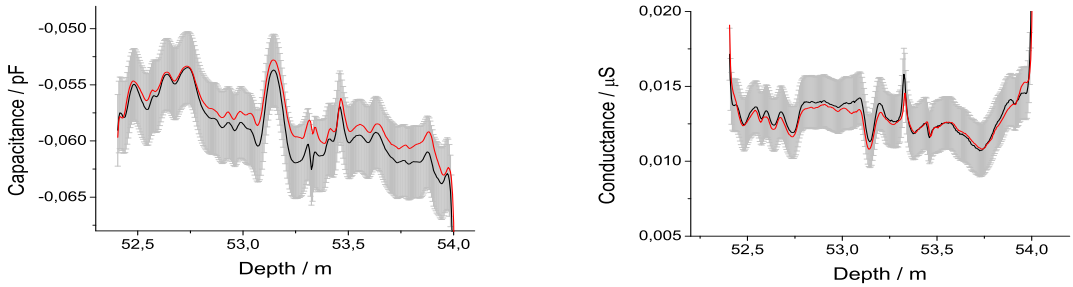

Core Piece 72

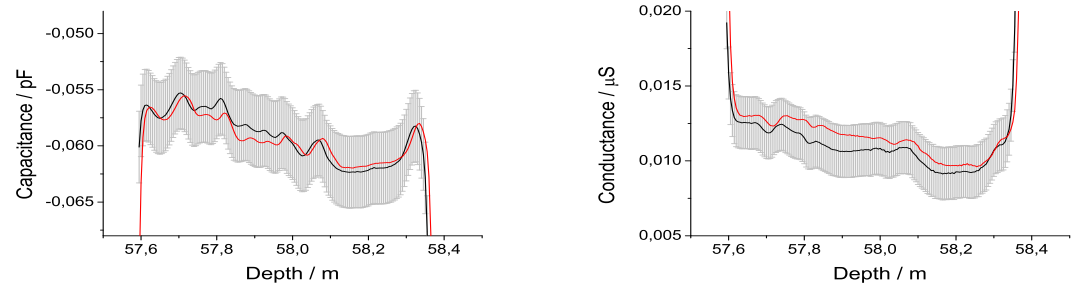

Core Pieces 80/81

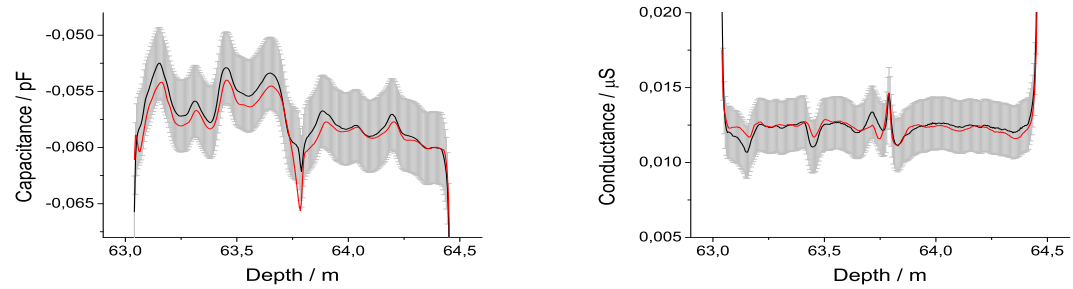

Core Pieces 88/89

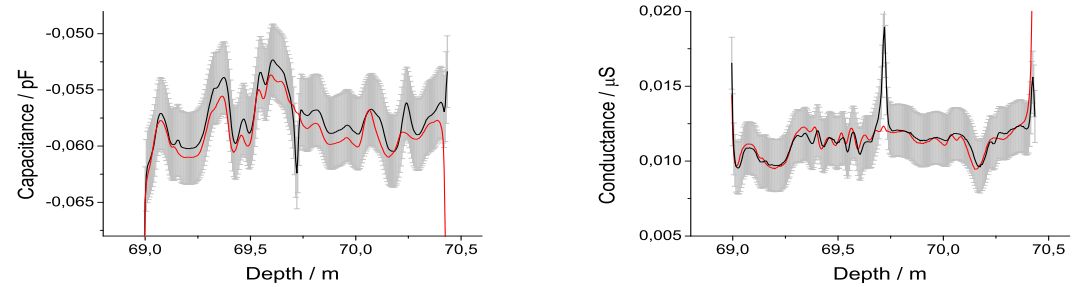

Figure B.2: Comparison of the results of the 2nd approach for the archive piece correction with appendant measurements of intact core pieces for the segments 64/65, 72, 80/81 and 88/89 of the core, which were measured both as intact core pieces before cutting and as archive pieces after cutting. Apparently the factor correction corresponding to the 2nd approach results for the corrected archive pieces in curves (black), that correspond well within one standard deviation (grey shaded uncertainty range) with the course of the intact core pieces data (red).

Core Pieces 134/135

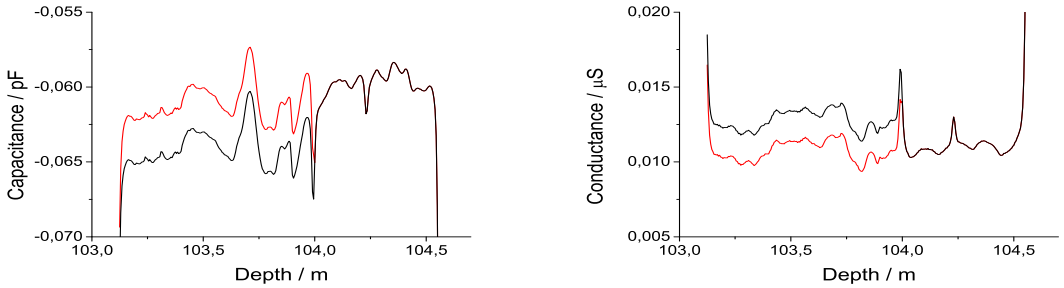

Figure B.3: Comparison of the result of the 2nd approach for the archive piece correction with the uncorrected data for the core pieces 134/135: The impact of the archive piece correction gets qualitatively distinct, when scrutinizing the data of the core pieces 134 and 135. Both were measured in one run with 134 due to a too large diameter for the setup measured as archive piece and 135 as intact core piece. The data before correction (black) comprises a significant discontinuity at the transition between the core pieces, which is reduced to insignificance compared to the natural variability of the data after the correction (red).

B.2 OFFSET CORRECTION

The measured values of capacitance C and conductance G deviate due to the failed open calibration from the true values C^{true} and G^{true} of the ice core and have to be corrected by offsets ΔC and ΔG:

$$C^{true} = C + \Delta C \tag{B.17}$$

$$G^{true} = G + \Delta G \tag{B.18}$$

CALCULATIONS FOR THE 1ST APPROACH

In this approach the offsets on the capacitance and conductance are calculated as differences between literature values of the empty capacitance $C_0^{lit.}$ and conductance $G_0^{lit.}$ and the experimentally measured mean values of the average empty signals C_0 and G_0 of the setup. It holds:

$$\Delta C = C_0^{lit.} - C_0 \tag{B.19}$$

$$\Delta G = G_0^{lit.} - G_0 \tag{B.20}$$

$$\text{with} \quad C_0 = \frac{\int dz' C_0^{exp.}(z')}{\int dz'} \qquad G_0 = \frac{\int dz' G_0^{exp.}(z')}{\int dz'}$$

CALCULATIONS FOR THE 2ND APPROACH

In the second approach the offsets of the capacitance and conductance shall be derived from literature values of the permittivity $\varepsilon_{ice}^{lit.}$ and the conductivity $\sigma_{ice}^{lit.}$ of glacier ice. If the actually measured capacitances and conductances C, C_0, G and G_0 are inserted into the simple material laws (B.5) and (B.6), one calculates permittivities ε and conductivities σ which deviate from the true permittivities ε^{true} and conductivities σ^{true} of the material, as the measured capacitances and conductances contain the offsets and and therefore deviate them self from the true capacitances and conductances C and G. It holds:

$$\varepsilon^{true} = \frac{C^{true}}{C_0^{true}} \overset{(B.17)}{=} \frac{C + \Delta C}{C_0 + \Delta C} \tag{B.21}$$

$$\sigma^{true} = \frac{G^{true}}{G_0^{true}} \overset{(B.18)}{=} \frac{G + \Delta G}{G_0 + \Delta G} \tag{B.22}$$

With the measurements and the literature values $\varepsilon^{true} := \varepsilon_{ice}^{lit.}$ and $\sigma^{true} := \sigma_{ice}^{lit.}$ one can calculate the offsets by the relations:

$$(B.21) \Longrightarrow \qquad \Delta C = \frac{\varepsilon - \varepsilon^{true}}{\varepsilon^{true} - 1} \cdot C_0 = \frac{\varepsilon - \varepsilon_{ice}^{lit.}}{\varepsilon_{ice}^{lit.} - 1} \cdot C_0 \tag{B.23}$$

$$(B.22) \Longrightarrow \qquad \Delta G = \frac{\sigma - \sigma^{true}}{\sigma^{true} - 1} \cdot G_0 = \frac{\sigma - \sigma_{ice}^{lit.}}{\sigma_{ice}^{lit.} - 1} \cdot G_0 \tag{B.24}$$

B.3 Correlations of DEP Data and Impurities

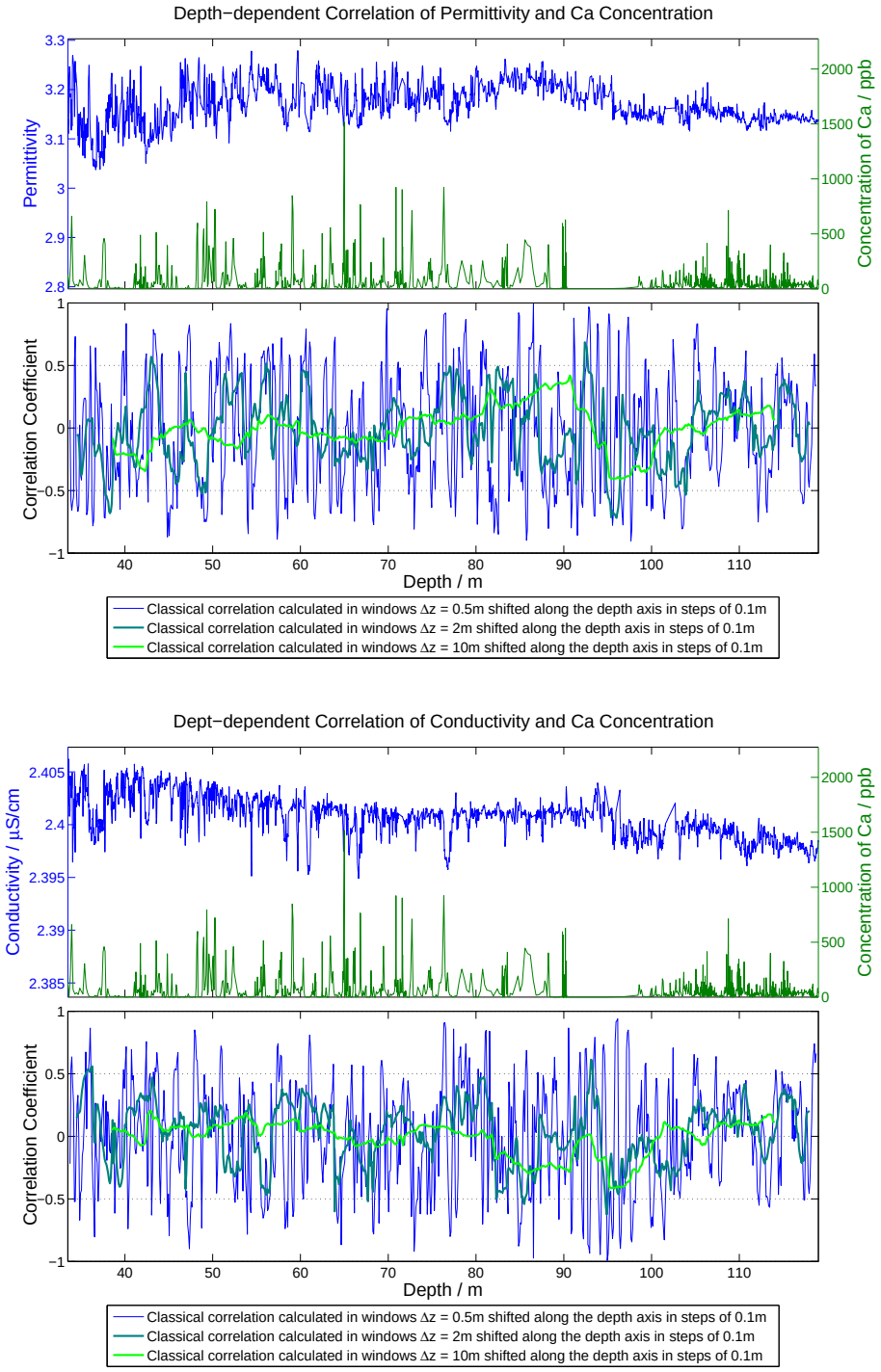

Figure B.4: Depth-dependent correlations between DEP data of the CDM core with calcium concentrations of the CDK core. A point in the correlation-depth diagram in a distinct depth z represents the absolute correlation calculated on data in the depth interval $[z-\Delta z_{window}/2, z+\Delta z_{window}/2]$ (cf. Appendix D.2). Bedrock lies at 121m.

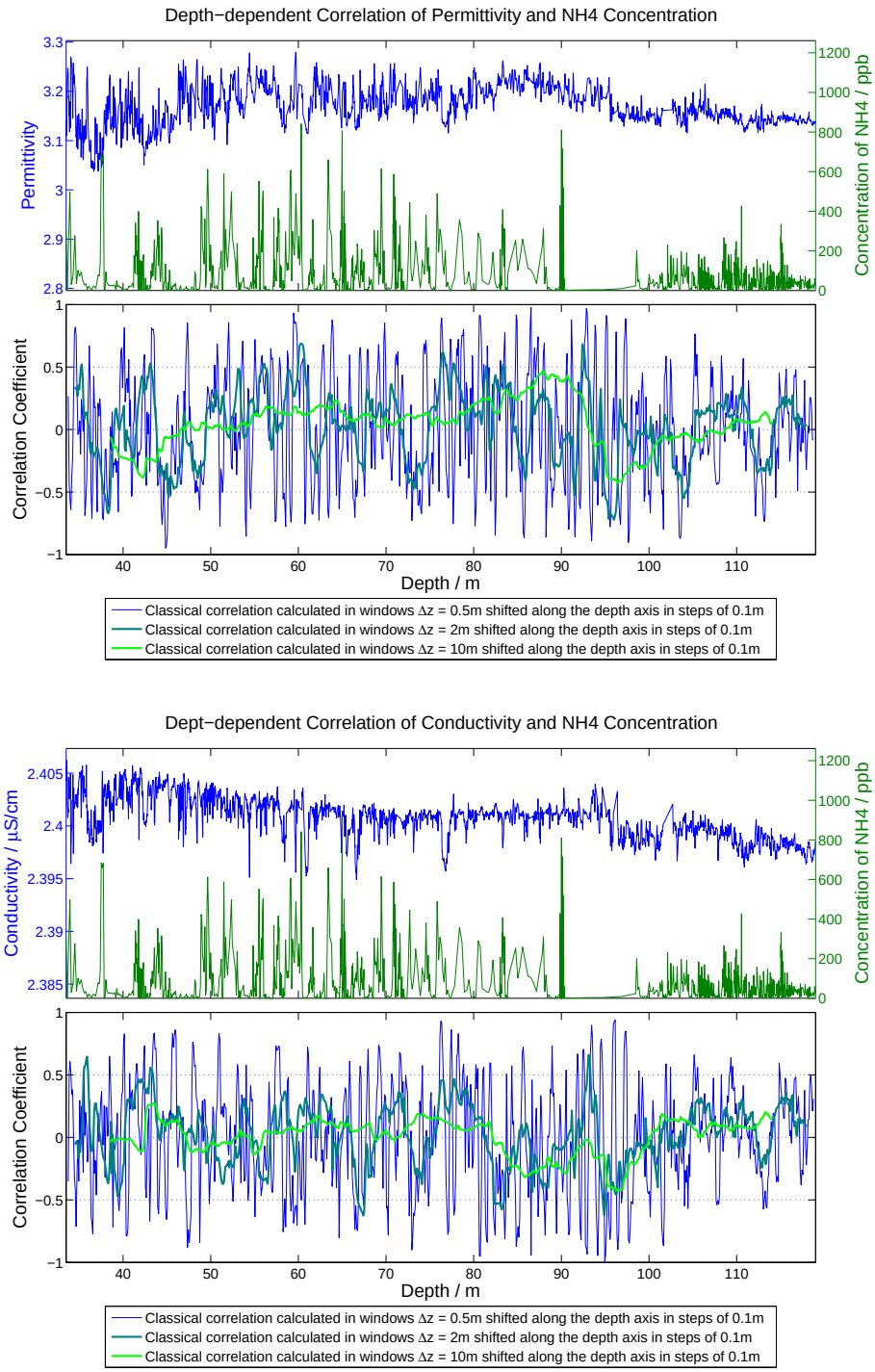

Figure B.5: Depth-dependent correlations between DEP data of the CDM core with ammonium concentrations of the CDK core. A point in the correlation-depth diagram in a distinct depth z represents the absolute correlation calculated on data in the depth interval $[z-\Delta z_{window}/2, z+\Delta z_{window}/2]$ (cf. Appendix D.2). Bedrock lies at 121m.

B.4 VARIABILITY OF DEP DATA AND IMPURITIES

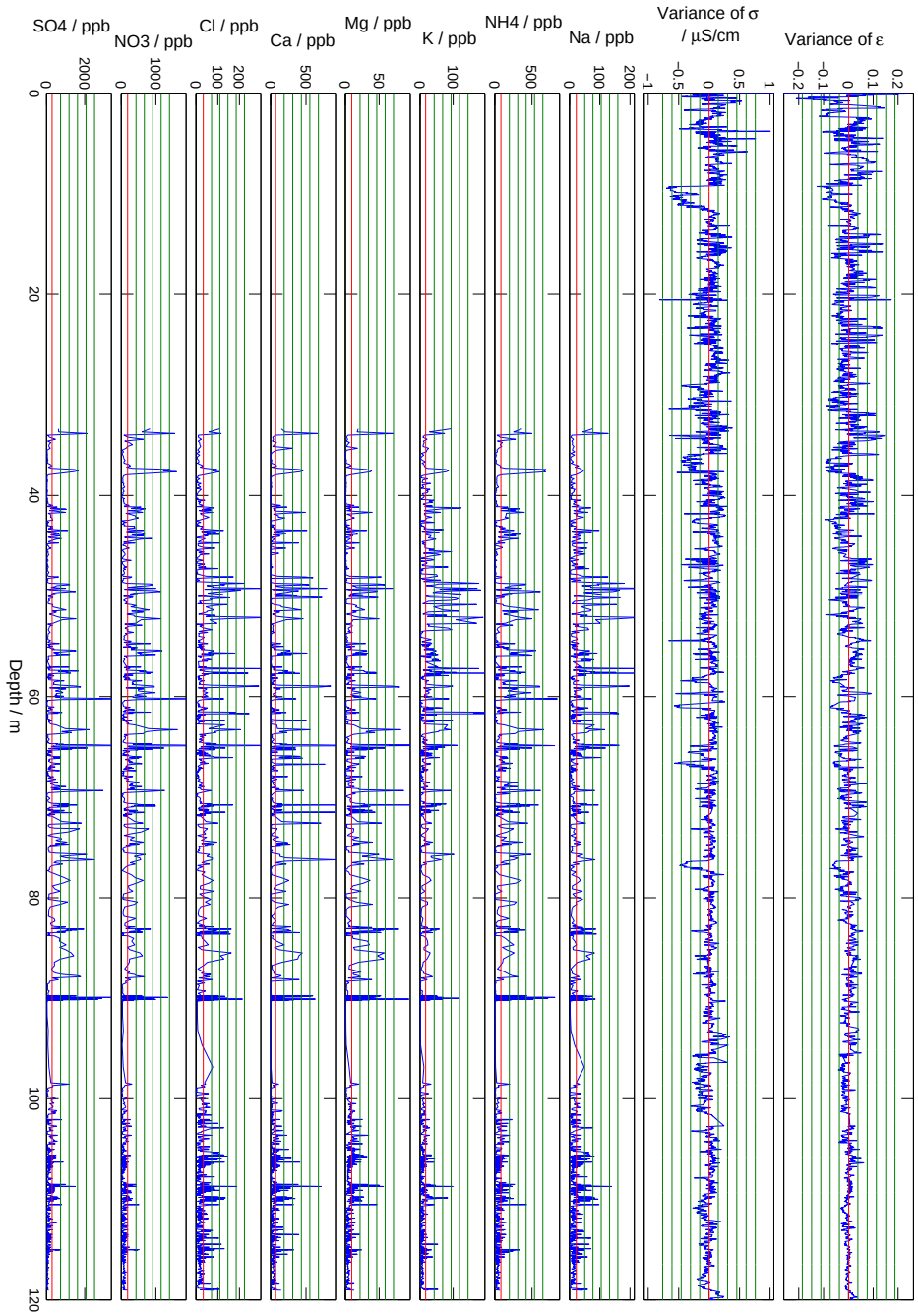

Figure B.6: Variabilities of the detrended permittivity and conductivity profiles (cf. Figure D.1) and the impurity concentrations (blue). Further depicted are the signals mean values (red line) and standard deviations (green lines). Note the reduction of signal variabilities below ca. 90m. Bedrock lies at 121m.

C Application of the Flow Model SYNDICATE to Radar Profile 121601 from Col Du Dôme

SYNDICATE [Konrad, 2011, Konrad *et al.*, 2013] is a 2.5-dimensional flow model along one flow line based on COURAN [Vincent *et al.*, 1997].

Input	Output
• Geometry of glacier surface and bedrock	• Age-depth profile at a point of choice
• Net-surface accumulation	• Flow lines
• Divergence parameter	• Isochrones
• Horizontal surface velocity at the starting ($\equiv$ highest) point $x = 0$ of the flow line	

It has been applied by [Konrad, 2011, Konrad *et al.*, 2013] for the vertical and spatial extrapolation of the coherent dating of ice cores of the Alpine multi-core array at Colle Gnifetti (CG). It improved the coherent dating of the ice cores from 80 years before present (BP$\equiv$2012) without to 120 years BP with the flow model.

Application to Radar Profile 121601 SYNDICATE has been applied to profile 121601 from Col du Dôme (cf. Figure 4.1, Chapter 4). Input parameters for geography , net-surface accumulation (cf. Table C.1) and surface velocities (i.e. 0.4m w.e./a for $x = 0$) were taken from Vincent *et al.* [2007a]. The density profile was taken from the CDM core [Preunkert, 2012, personal communication]. The divergence parameter was set to 0.1. Flow lines were calculated starting from every 0.5m at the surface in a vertical resolution of 0.1m. A dating was calculated for the point of the cores CDM and CDK at $x = 285m$. The resulting age-depth relation is depicted in comparison to the one of DCK core in Figure C.1, model flow lines and isochrones are depicted in comparison with picked internal reflecting horizons from 121601 in Figure C.2. Note that SYNDICATE does not regard the influence of the crevasse upstream 121601. The model results therefore are not expected to depict the reality in the vicinity of the crevasse. However, as SNYDICATE is able to reproduce within limits the real situation along a flow line without crevasse [Konrad, 2011, Konrad *et al.*, 2013], model results may allow to assess the influence of the crevasse at CDD.

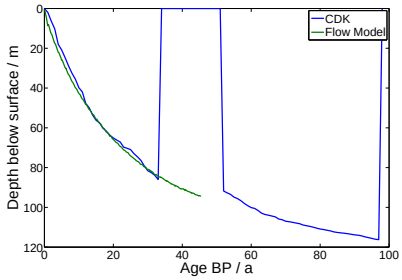

Figure C.1: Age-depth profile from flow modelling at the position of CDM and CDK in comparison to the one of CDK.

Table C.1: Net-surface accumulations along profile 121601 as input for the flow model SYNDICATE.

Path length along the flow line / m:	0	22	70	124.5	141	158	176	194	215	235	258	285
Net-surface accumulation / m w.e./a:	0.4	0.6	0.8	1.0	1.3	1.6	1.9	2.1	2.3	2.5	2.7	2.9

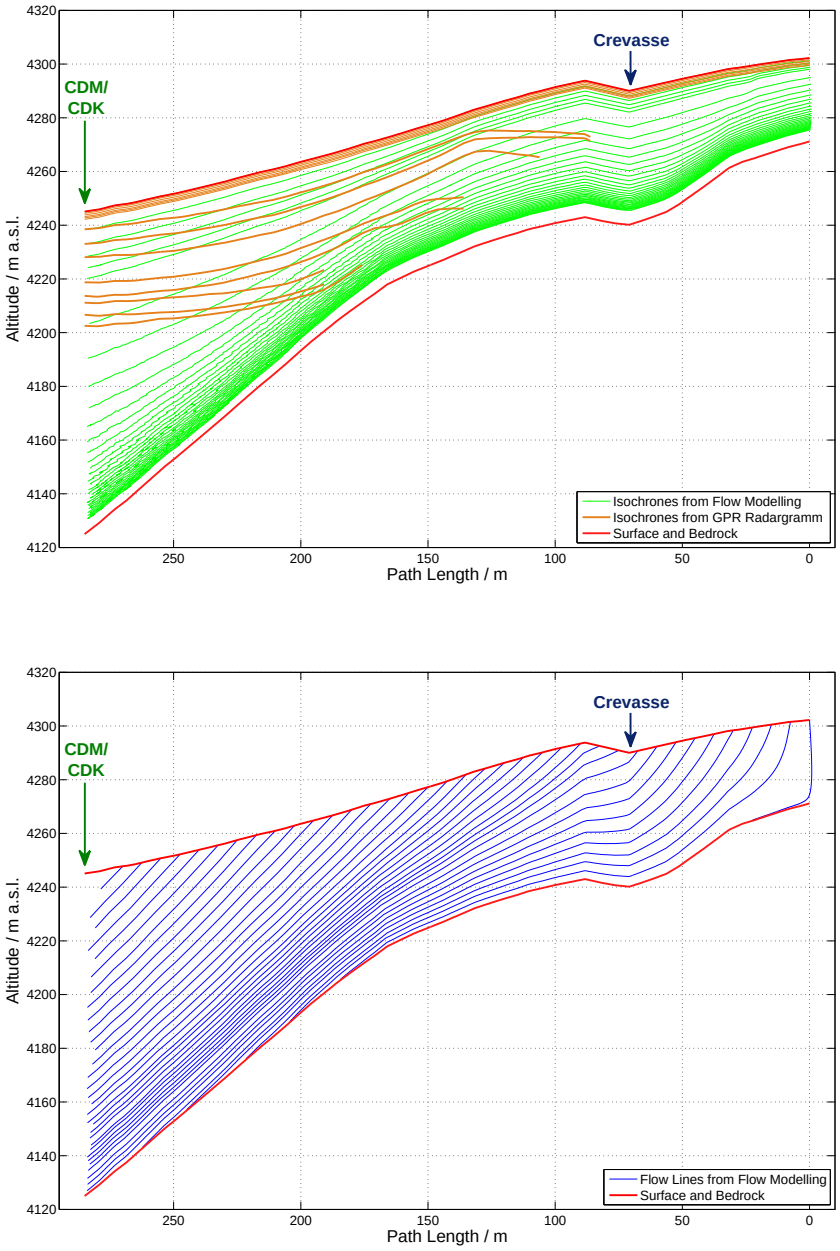

Figure C.2: Results from the application of the flow model SYNDICATE [Konrad, 2011, Konrad *et al.*, 2013] to the radar profile 121601 (cf. Figure 4.1, Chapter 4) from Col du Dôme. **Top:** Modelled isochrones (green) in 10 year distances in comparison to picked internal reflecting horizons (IRH) (orange) from radargramm 121601. Note the descending course of the real IRH in the vicinity of the crevasse. **Bottom:** Modelled flow lines (blue) starting every 7.5m at the surface. **Both Figures:** The flow model cannot reproduce the influence of the crevasse. Note the deviation between the modelled and GPR isochrones in the vicinity of the crevasse.

D MISCELLANEOUS

D.1 DETRENDING OF THE PERMITTIVITY- AND CONDUCTIVITY-DEPTH PROFILES

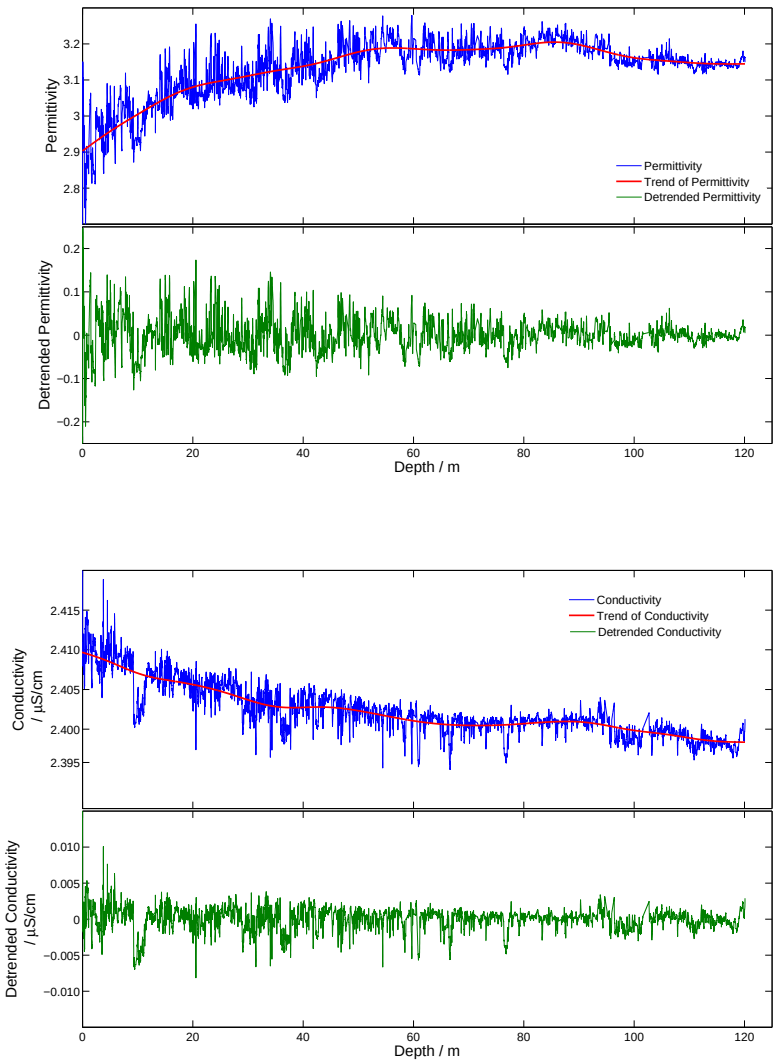

Figure D.1: Detrending of permittivity and conductivity. The detrending has been conducted by using AUTOSIGNAL of SeaSolve Software Inc.

D.2 Calculation of absolute and depth-dependent Correlations

Correlations in this thesis were calculated using a discrete implementation of the classical Pearson Correlation Coefficient [cf. Mudelsee, 2010].

$$r_{xy} = \frac{1}{n}\sum_{i=1}^{n}\frac{(x_i-\bar{x})(y_i-\bar{y})}{s_{n,x}\cdot s_{n,y}} \tag{D.1}$$

$$\text{with} \quad s_{n,x} = \sqrt{\frac{1}{n}\sum_{i=1}^{n}(x_i-\bar{x})^2}, \quad \bar{x} = \frac{1}{n}\sum_{i=1}^{n}x_i \quad \text{and} \quad s_{n,y} = \sqrt{\frac{1}{n}\sum_{i=1}^{n}(y_i-\bar{y})^2}, \quad \bar{y} = \frac{1}{n}\sum_{i=1}^{n}y_i$$

They are partially calculated as here so-called **absolute correlations** on the complete data sets from surface to bedrock and partially as so-called **depth-dependent correlations** in windows of size Δz_{window} shifted along the depth axis in equidistant steps. In the later case a point in the correlation-depth diagram in a distinct depth z represents the absolute correlation calculated on data in the depth interval $[z-\Delta z_{window}/2, z+\Delta z_{window}/2]$. For data sets with different depth increments the data was interpolated to identical depth increments thereby increasing the increment before the calculation of correlations was conducted.

ACKNOWLEDGEMENT

I am obliged to various people, without whose support this thesis would not have been possible.

Amongst these first of all I thank my advisor Dr. Pascal Bohleber for guidance, support and long hours of proofreading. Honour is due to my group leader and advisor Dr. Dietmar Wagenbach for general guidelines and noble allowances of academic freedom with respect to my endeavour.

I am much obliged to the *Alfred-Wegener Institute for Polar and Maritime Research* (AWI) and particularly to Prof. Dr. Frank Wilhelms who developed and supplied the dielectric profiling (DEP) bench applied in this thesis. Prof. Dr. Frank Wilhelms I am further thankful for his kind willingness to discuss DEP processing approaches and results. Dr. Sepp Kipfstuhl I am grateful for his unfailing support during the DEP measurements and the processing of the KCC core in the cooling chambers of the AWI. Dipl. Ing. (FH) Andreas Frenzel kindly supplied a measurement software for the DEP measurement bench.

Prof. Dr. Olaf Eisen I owe gratitudes for the supply of software for the forward modelling and continuous counsel regarding the analysis of the ground penetrating radar data, the forward modelling or the thesis's results in general.

Dr. Susanne Preunkert and the people of the *Laboratoire de Glaciologie et Géophysique de l'Environnement* I am grateful for the support they offered during the DEP measurements of the CDM core in their institute in Grenoble and for the supply of glaciological data regarding Col du Dôme and its ice cores.

Furthermore I am committed to the drilling teams who retrieved the ice cores CDM and KCC.

Not least I am grateful for the amiable and reliable collaboration of my colleagues of the glaciological research group of the *Institut für Umweltphysik* of the *University Heidelberg*.

Finally I thank Prof. Dr. Kurt Roth and Prof. Dr. Olaf Eisen who kindly agreed to assess my work as referees.

THANK YOU!

ERKLÄRUNG

Ich versichere, dass ich diese Arbeit selbstständig verfasst habe und keine anderen als die angegebenen Quellen und Hilfsmittel verwendet habe.

Heidelberg am 12. November 2013